CHAPTER IV

RESULTS AND DISCUSSION

4.1. Formation of Self-Organized TiO_2 Nanotube Arrays by Anodization

4.1.1 Conventional Anodization VS Pulse Anodization

These anodization experiments used either constant potential (potentiostatic) or constant current (galvanostatic) nanotube growth modes. On the other hand, the interplay of electrochemical and chemical processes inherent in the anodic film growth suggests that pulsing the potential between carefully chosen limits and varying the duty cycle (i.e., voltage 'on' and 'off' durations) can exert an important influence on the film morphology and nanotube formation. Fig. 4.1 compare the SEM micrographs for TiO_2 samples prepared by constant anodization at 20 V (Fig. 4.1a) with those grown via 20 V/-4 V pulses (Figs. 4.1b and c). In all three cases, aqueous NH_4F electrolytes (0.36 M concentration) were used for 3 h growth times in water (Figs. 4.1a and b) or in glycerol containing 1% water ("wet" glycerol) (Fig. 4.1c). In Figs. 4.1a and b, DI water-was used (instead of "wet" glycerol) to bring out the effect of NH_4F on the ordering of the anodic layer nanoarchitecture. Glycerol was reported by other authors (Macak *et al.*, 2005) to exert a viscosity modifying effect and to afford smooth TiO_2 nanotubes by suppressing local concentration fluctuations and pH bursts during anodization. However, a comparison of Figs. 4.1a and b immediately reveals that under the supposedly "adverse" conditions in the absence of this organic medium, the pulse anodization approach affords a self-ordered array of TiO_2 nanotubes on the Ti substrate. Importantly, the film morphology was considerably improved when pulse anodization was combined with "wet" glycerol as the growth medium (comparing Figs. 4.1b and c). The TiO_2 nanotube also shrinked from 67 ± 2 nm in NH_4F to 60 ± 2 nm when glycerol is added to the fluoride electrolyte.

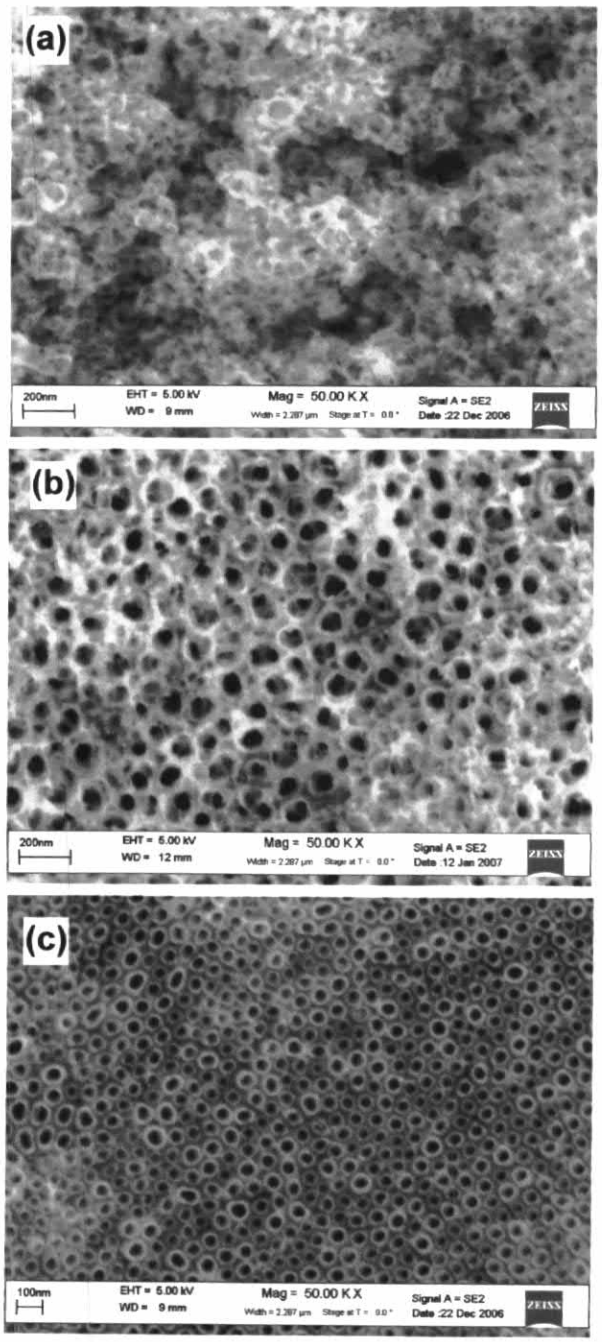

Figure 4.1 Scanning electron micrographs of TiO_2 films formed from a Ti foil in 0.36 M NH_4F by anodization at constant potential (20 V, 3 h) (a), and by pulse anodization (20 V/-4 V, 3 h) in water (b) and in "wet" glycerol (c).

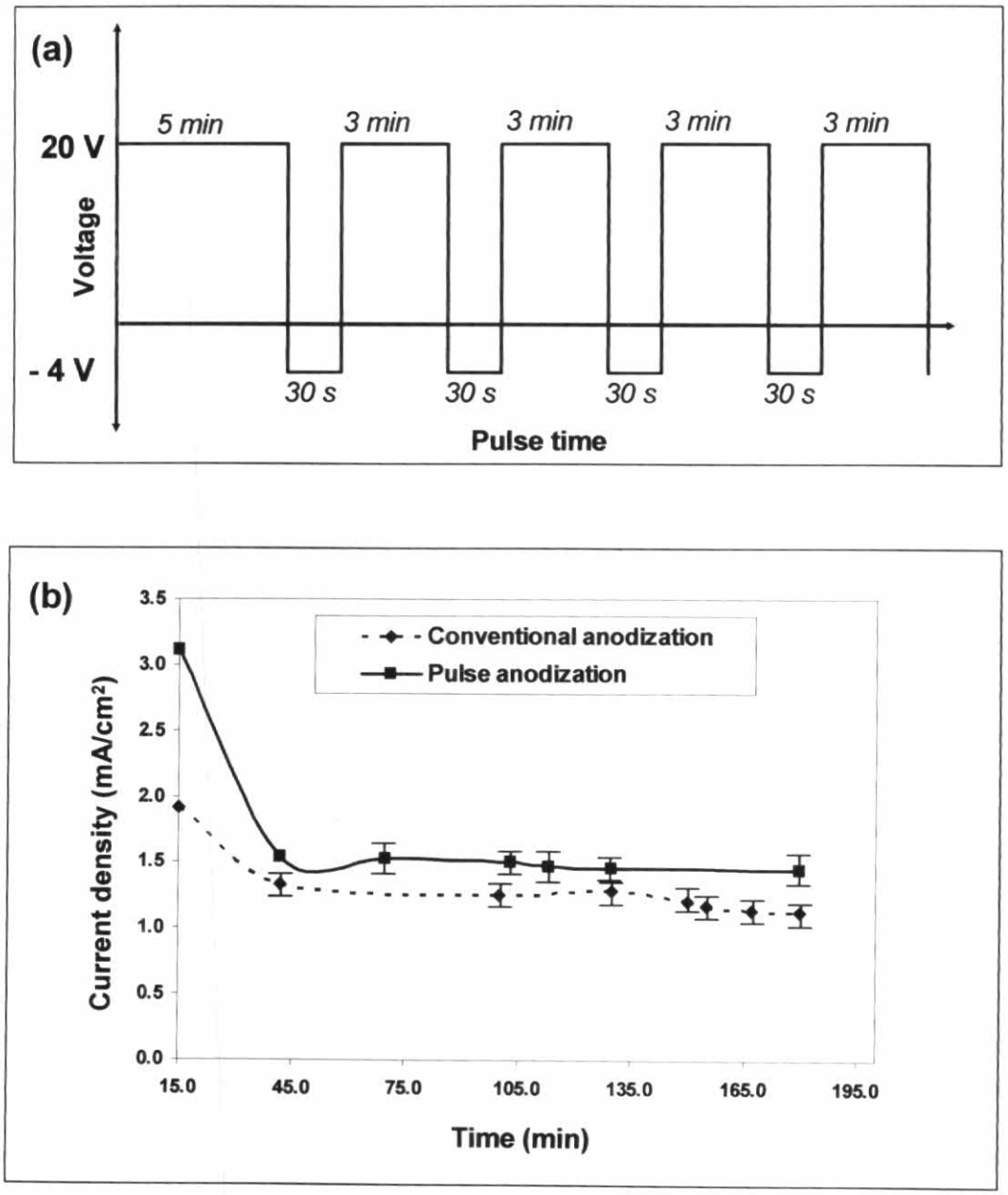

Figure 4.2 Potential pulse waveform used for the anodic growth of TiO_2 nanotube arrays.

The negative limit of the voltage pulse (Fig.4.2) and the cathodic current flow regime of the pulse both exert a crucial effect on the nanotube morphology which is mainly controlled by the following chemical and electrochemical reactions (equations 4.1 and 4.2). In general, hydrogen evolution is occurring at the TiO_2/electrolyte because the semiconductor is under direct biased condition (i.e. under an applied potential more negative than its flat band potential). Besides, during the cathodic

voltage portion of the cycle, chemical dissolution of the oxide in the fluoride electrolyte (i.e., F^- ion-etch, see equations 4.1 and 4.2) plays a key role in the anodic layer morphology(Cai *et al.*, 2005; Mor *et al.*, 2006).

$$TiO_2 + 6NH_4F \rightarrow TiF_6^{2-} + 6NH_3 + 2H_2O + 2H^+ \qquad \text{(Eq. 4.1)}$$

$$2H^+ + 2e^- \rightarrow H_2 \qquad \text{(Eq. 4.2)}$$

Table 4.1 Anodization conditions, diameter, wall thickness, and photoelectrochemical performance of resulting TiO_2 nanotubes.

No.	Electrolyte, medium modifier	Pulse duration	Voltage, total time	Nanotube diameter [a]	Nanotube length[a]	Wall thickness[a]	j_{ph}/mA cm^{-2} [b]
1	0.36 M NH_4F	constant potential	20 V, 3 h	nanoporous	n.d. [c]	n.d.	1.21
2	"	3 min, 30 s	20 V/-4 V, 3 h	67 ± 2 nm	300 ± 10 nm	19.0 ± 0.5 nm	1.95
3	0.36 M NH_4F, glycerol	constant potential	20 V, 3 h	68 ± 2 nm	607 ± 10 nm	13.0 ± 0.5 nm	1.56
4	"	3 min, 30 s	20 V/-4 V, 3 h	60 ± 2 nm	389 ± 10 nm	20.6 ± 0.5 nm	2.10

[a] As assessed by SEM.
[b] j_{ph} = photocurrent density in 0.5 M Na_2SO_4 at 1.5 V
[c] No data

These account for the progression in layer morphology from a nanoporous structure (Fig. 4.1a) to a discrete tubular appearance (Fig. 4.1b) when the chemical etch process (equation 4.1) is allowed to exert an effect in the pulse mode. However, the two processes of nanotube growth and self-assembly and the chemical/electrochemical dissolution must be carefully balanced; for example, too facile a chemical etch will destroy the nanotube array structure. In this regard, a negative voltage limit (e.g., -4 V) serves to electrostatically induce the binding of NH_4^+/NH_3 species (equation 4.3).

$$TiO_2 + NH_3 \rightarrow TiO_2(NH_3)_{ads} \qquad \text{(Eq. 4.3)}$$

Adsorption of NH_3 on TiO_2 surface was already reported (Pittman *et al.*, 1994) and in the present case we speculate that this will protect the nanotube walls against chemical etch by F^- ions or ameliorate the extent of it. This is clearly seen in Table 4.1 where the effect of pulse (20 V/ -4 V) and constant (20 V) anodization conditions (columns 2-4) on the ensuing nanotube diameter, nanotube length, wall thickness,

(columns 5-7) and related photocurrent (column 8) is presented. Electroadsorbed NH_4^+ on the nanotube walls, during the -4 V pulse, enhances wall thickening and thus reduces the nanotube diameter and length (compare entries 3 and 4). Indeed comparison of samples obtained from a +20 V/0 V pulse sequence (show in section 4.2) reveals an inferior morphology (and photoresponse quality) relative to those from the +20 V/-4 V pulse mode (Fig. 4.2a) considered here. The negative pulse potential induces NH_4^+ adsorption whereas at 0 V this effect is negligible. In fact, there is both experimental (Pittman *et al.*, 1994) and theoretical (Markovits *et al.*, 1996) precedence for the adsorption of NH_3 on TiO_2; NH_3 and NH_4^+ species are believed to adsorb on Lewis and Brønsted acid sites on the oxide surface.

Considerable information exists on the mechanistic aspects of anodic alumina growth dating back to more than 50 years (Diggle *et al.*, 1969; Hoar *et al.*, 1959; and Xu *et al.*, 1985). On the presumption that similar phenomena apply to valve metals such as titanium, the first stage is barrier layer oxide growth on the Ti substrate. Formation of this compact layer decreases the electric field abruptly; the main reaction in this regime (called the "recovery" period) is chemical dissolution. After a certain time, the barrier layer thickness decreases increasing the electric field across this layer. Now the field-assisted oxide growth and electrochemical dissolution can kick in. The higher current densities (by ~ 20%) seen in this study (Fig. 4.2b) for the pulse mode can then be related to a thinning of the barrier layer by the *controlled* chemical etch/hydrogen discharge during the negative voltage pulses. Clearly, these factors are beneficial to optimal nanotube formation, growth and self-assembly (Figs. 4.1b and c). A fuller account of the effects of the voltage pulse duty cycle and the negative limit values on the nanotube morphology and properties will be discussed in next section.

The photoelectrochemical response of TiO_2 films prepared under constant (20 V) and pulse (20 V/-4 V) polarization are shown in Fig. 4.3A and a bar graph comparing photocurrent densities at a reverse bias potential of + 1.5 V (vs. Ag|AgCl reference) in 0.5 M Na_2SO_4 supporting electrolyte for films prepared in water and glycerol media is contained in Fig. 4.3B. The anodic photocurrents measured for the TiO_2 nanotube arrays in 0.5 M Na_2SO_4 (Figs. 4.3) presumably reflect the oxidation of water and/or surface hydroxyl groups by the photogenerated holes in the oxide. Note that no hole scavengers were present in the supporting electrolyte in both cases in Figs. 4.3.

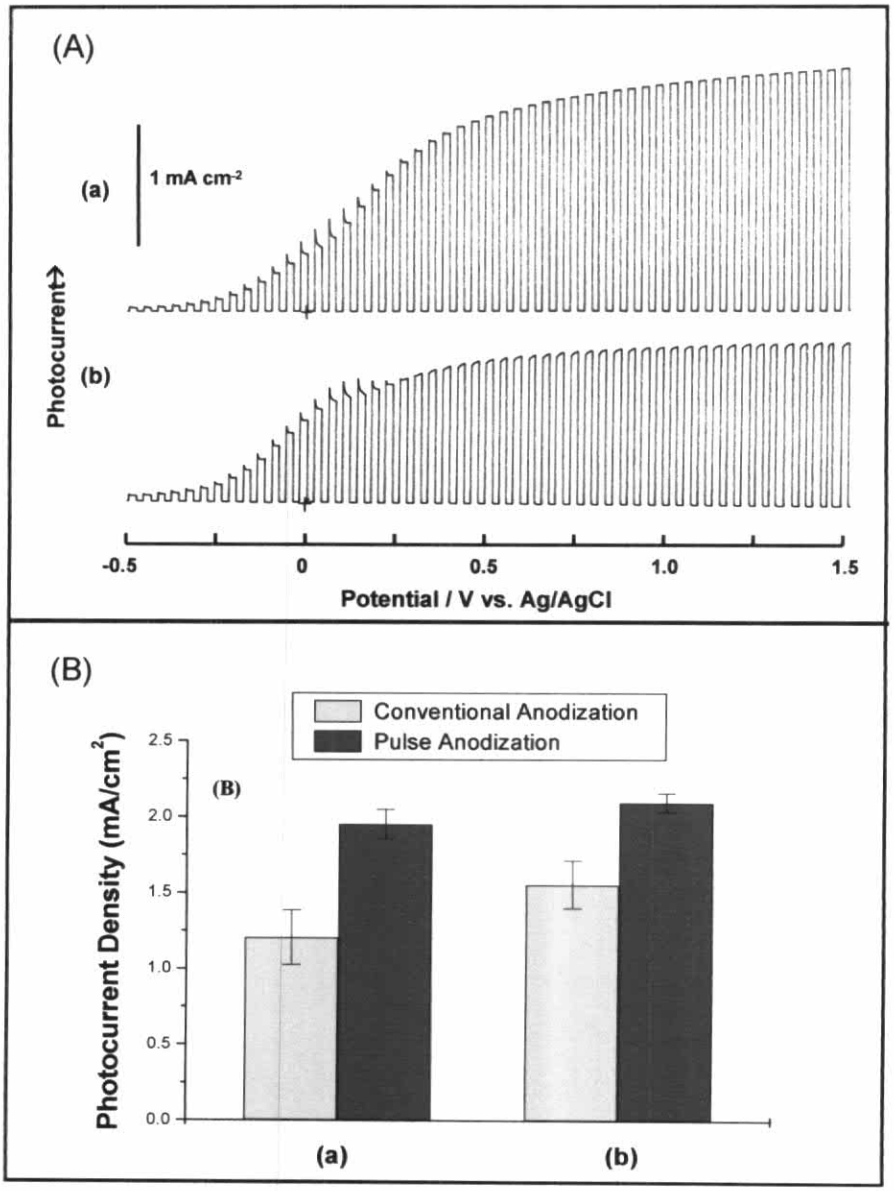

Figure 4.3 (A) Photocurrent-potential profiles under chopped irradiation (0.05 Hz) for TiO_2 nanotube arrays prepared using pulse (a) and constant (b) anodization. These TiO_2 films were grown in 0.36 M NH_4F in water. (B) Comparative bar diagram of photocurrent density performance for TiO_2 nanotube arrays prepared using either pulse or constant anodization. Photocurrent data were obtained in 0.5 M Na_2SO_4 supporting electrolyte and at +1.5 V (vs. Ag|AgCl ref. electrode). The TiO_2 films were grown in 0.36 M NH_4F in water (a) and in "wet" glycerol (b).

The increase in the magnitude of the photocurrent densities by ~26% - ~38% for the pulse anodized nanotube arrays relative to the samples obtained from the conventional, continuous anodization approach, then reflects better e^- - h^+ pair separation and transport in the former. Interestingly, the nanotubes prepared by pulse anodization are shorter than those under constant voltage (see Table 4.1) but in both cases they are longer than the depth of penetration (α^{-1}) of the UV light into the film. As an example, wavelengths of 340 nm will have a light penetration depth (L_λ) of only 200 nm (Mollers *et al.*, 1974) while at 335 nm the L_λ will be of ~ 100 nm (Lindquist *et al.*, 1983). In both cases the light penetration corresponds to the inverse of the absorption coefficient, α^{-1}, of TiO_2 anatase phase. Moreover, the wall thickness is thicker in the pulse anodized films which in turn indicates that these films contain a larger amount of TiO_2 per constant length than those prepared by constant anodization.

4.2 Formation of self-organized TiO_2 nanotube arrays by pulse anodization

In a previous section, we reported the anodic growth of self-organized nanoporous TiO_2 films by anodization under different conditions (de Tacconi *et al.*, 2006). From this work it was obvious that the nanotube morphology, tube diameter, wall thickness, and photocurrent response depended on the anodization and growth medium variables. In the present study, we expand the anodization protocol to a wider range of growth conditions as shown in Table 4.2. The nanotube arrays are now grown from Ti foils by pulse anodization using either 20 V/-4 V or 20 V/0 V sequences. In either case, the potential perturbation was applied for 3 h and compared to films prepared for same time period but under constant polarization, i.e., at 20 V. The pulse durations were set in the 150 s -180 s range for the positive potential limit and in the 2 s - 30 s for the lower potential pulse. Table 4.2 compiles the potentials and pulse durations combined with four electrolyte compositions. Moderately concentrated NH_4F (0.36 M) was used as both supporting electrolyte and chemical complexing agent; it was used directly in aqueous solution (entries no. 1-8 in Table 4.2) or in combination with a medium modifier; i.e., dissolved in 90% glycerol:10 % water (entries no. 9-16), in 90% ethylene glycol:10% water (entries no. 17-24), and in 80% PEG 400 – 20% water (entries no. 25-32).

4.2.1 Effect of pulse anodization. The scanning electron microscopy (SEM) images in Fig. 4.4 compare the surface morphology of TiO_2 films prepared by conventional anodization (20 V, 3 h) in 0.36 M NH_4F and 0.36 M NH_4F/glycerol:H_2O (90:10) electrolytes (Figs. 2a and c) and pulse anodization using a 20 V/-4 V pulse sequence for 2 s in the same electrolytes (Figs. 4.4b and d).

The organic additive was intentionally omitted for the films shown in Figs. 4.4a and b to bring out the effect of glycerol on the ordering of the anodic layer nanoarchitecture. Glycerol was reported by other authors (Macak *et al.*, 2005) to exert a viscosity modifying effect to afford smooth TiO_2 nanotubes by suppressing local concentration fluctuations and pH bursts during anodization. However, a comparison of Figs. 4.4b and d immediately reveals that even under the supposedly "adverse" conditions in the absence of this organic additive, the pulse anodization approach affords a self-ordered array of TiO_2 nanotubes on the Ti substrate. The nanotube array morphology is considerably improved when pulse anodization is combined with organic additive addition to the electrolyte (Fig. 4.4d). Importantly,

TiO_2 nanotubes grown in aqueous NH_4F using the pulse anodization mode is seen to result in better-defined nanotube morphologies than in the constant voltage growth mode (c.f., Figs. 4.4a and c).

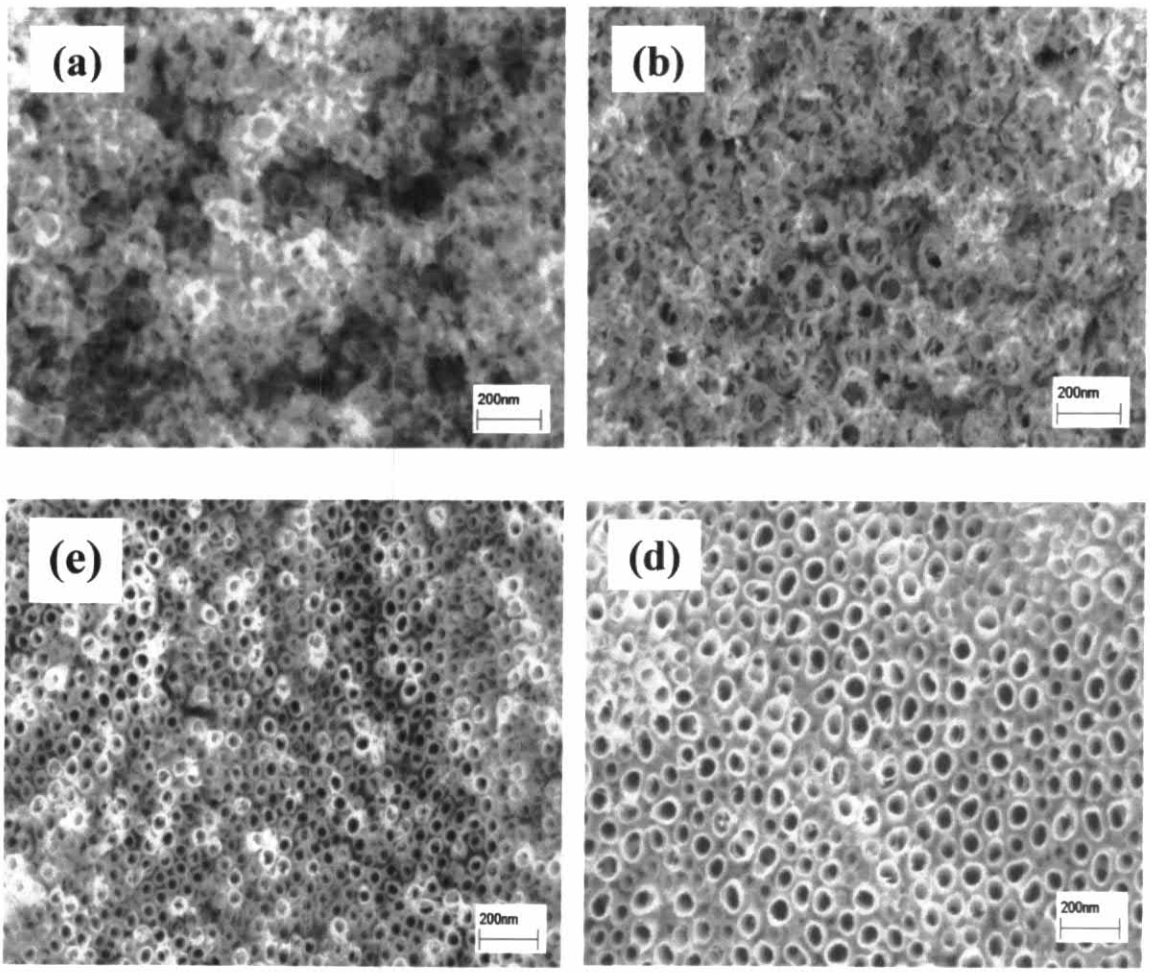

Figure 4.4 SEM images of TiO_2 nanotube arrays grown by conventional anodization (20 V, 3 h) (a, c) compared with corresponding samples from pulse anodization at 20 V/-4 V (2 s pulse duration at the negative voltage limit) (b, d). Frames (a) and (b) correspond to 0.36 M NH_4F electrolyte in aqueous medium and frames (c) and (d) correspond to the same electrolyte in glycerol medium.

Table 4.2 Anodization conditions, photoelectrochemical performance and morphology of TiO_2nanotube films in this study.

entry no.	electrolyte, medium modifier	duration of pulse anodization (t_1,t_0)	pulse anodization voltage, time	Nanotube length (nm) [a]	wall thickness (nm) [a]	Nanotube diameter (nm) [a]	j_{ph} (mA cm^{-2}) [b]
1	0.36 M NH_4F	-	20 V, 3 h	n.d. [c]	n.d	n.d.	1.2± 0.2
2	"	150, 2 s	-4/20 V, 3 h	2090± 10	n.d.	n.d.	2.1± 0.1
3	"	160, 7 s	-4/20 V, 3 h	n.d.	n.d.	n.d.	0.9± 0.2
4	"	170, 16 s	-4/20 V, 3 h	n.d.	n.d.	n.d.	0.8± 0.1
5	"	180, 30 s	-4/20 V, 3 h	300± 10	19.0± 0.5	67± 2	2.0± 0.1
6	"	150, 2 s	0/20 V, 3 h	n.d.	n.d.	n.d.	1.7± 0.2
7	"	160, 7 s	0/20 V, 3 h	n.d.	n.d.	n.d.	1.4± 0.1
8	"	170, 16 s	0/20 V, 3 h	n.d.	n.d.	n.d.	1.5± 0.1
9	0.36 M NH_4F/ glycerol:H_2O (90:10)	-	20 V, 3 h	607± 10	13.0± 0.5	68± 2	1.6± 0.2
10	"	150, 2 s	-4/20 V, 3 h	580± 10	15.6± 0.5	83± 2	4.2± 0.1
11	"	160, 7 s	-4/20 V, 3 h	n.d.	16.4± 0.5	70± 2	3.2± 0.1
12	"	170, 16 s	-4/20 V, 3 h	481± 10	17.9± 0.5	76± 2	3.1± 0.2
13	"	180, 30 s	-4/20 V, 3 h	389± 10	20.6± 0.5	60± 2	2.1± 0.1
14	"	150, 2 s	0/20 V, 3 h	n.d.	11.2± 0.5	72± 2	3.7± 0.1
15	"	160, 7 s	0/20 V, 3 h	n.d.	15.6± 0.5	73± 2	2.6± 0.2
16	"	170, 16 s	0/20 V, 3 h	228± 10	13.4± 0.5	72± 2	2.2± 0.1
17	0.36 M NH_4F/ethylene glycol:H_2O(90:10)	-	20 V, 3 h	837± 10	14.4± 0.6	55± 3	1.2± 0.2
18	"	150, 2 s	-4/20 V, 3 h	n.d.	15.4± 0.5	82± 2	2.3± 0.2
19	"	160, 7 s	-4/20 V, 3 h	n.d.	15.8± 0.5	78± 2	2.0± 0.1
20	"	170, 16 s	-4/20 V, 3 h	n.d.	16.6± 0.5	70± 2	1.7± 0.1
21	"	180, 30 s	-4/20 V, 3 h	n.d.	17.4± 0.5	62± 2	1.3± 0.1
22	"	150, 2 s	0/20 V, 3 h	527± 10	14.3± 0.6	69± 1	1.8± 0.1
23	"	160, 7 s	0/20 V, 3 h	436± 10	12.6± 0.6	70± 2	1.8± 0.2
24	"	170, 16 s	0/20 V, 3 h	365± 10	11.2± 0.6	71± 2	1.7± 0.1
25	0.36 NH_4F/PEG400:H_2O (80:20)	-	20 V, 3 h	727± 10	16.0± 0.4	120± 3	2.1± 0.2
26	"	150, 2 s	-4/20 V, 3 h	n.d.	15.4± 0.5	123± 2	2.5± 0.1
27	"	160, 7 s	-4/20 V, 3 h	n.d.	17.9± 0.5	120± 2	2.1± 0.1
28	"	170, 16 s	-4/20 V, 3 h	n.d.	20.1± 0.5	116± 2	2.1± 0.1
29	"	180, 30 s	-4/20 V, 3 h	n.d.	21.2± 0.5	104± 2	2.0± 0.1
30	"	150, 2 s	0/20 V, 3 h	n.d.	16.1± 0.4	91± 2	2.4± 0.2
31	"	160, 7 s	0/20 V, 3 h	n.d.	12.7± 0.4	92± 2	2.1± 0.1
32	"	170, 16 s	0/20 V, 3 h	n.d.	11.3± 0.5	93± 2	2.0± 0.2

[a] As assessed by SEM
[b] j_{ph}= photocurrent density in 0.5 M Na_2SO_4 at 1.5 V
[c] No data available

The average nanotube diameter increases from 68 ± 2 nm to 83 ± 2 nm with a pulsing protocol involving 2 s duration at the negative voltage (Figs. 4.4c and d). This enlargement trend is accompanied with a thickening of the nanotube walls which are seen to grow from 13.0± 0.5 nm to 15.6± 0.5 nm at the inner tube diameter. Thicker walls are obtained if the duration of the negative potential limit is increased (see Table 4.2). Thus, Fig. 4.5 shows the changes in the nanotube wall thickness (Fig. 4.5a) and diameter (Fig. 4.5b) as a function of the duration of the pulse (t_0) at the lower potential of the waveform. Data in this figure are for a 20 V/-4 V waveform. The range of wall thickening dimensions depends on the composition of the electrolyte, i.e., is higher in PEG 400 than in glycerol or ethylene glycol, but in all the three cases, a systematic increase is observed when t_0 is increased. These findings point to NH_4^+ and F^- (which are presented at the same concentration in the three cases studied) as the possible chemical culprits for these effects.

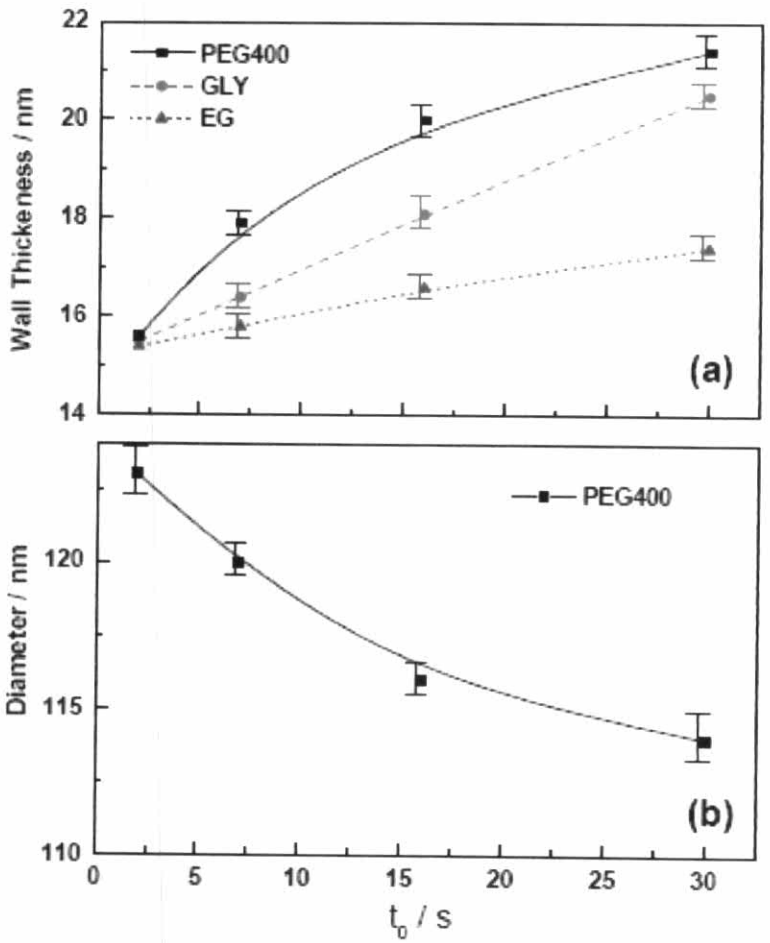

Figure 4.5 Nanotube wall thickness (Figure 4.5a) and diameter (Figure 4.5b) as a function of pulse duration (t_0) at the lower (i.e., more negative) potential of the waveform.

Another finding was that the nanotubes prepared by pulse anodization were shorter than those under constant voltage (see Table 4.2). As an example, in the nanotube arrays prepared from glycerol:H_2O 90:10 with 20 V/-4 V pulse anodization, a decrease in length from 580 ± 10 nm to 390 ± 10 nm was observed when t_0 was increased from 2 s to 30 s. Two factors are likely coupled for the decrease of the nanotube length with the pulse duration at the lower potential: (a) When the walls grow thicker, they contain more material in the x-y plane and therefore the z-axis (nanotube length) should be shorter than in the case of thinner walls in order to maintain the same amount of TiO_2 in both cases; (b) The pulse anodization was applied for the same total time of 3 h as for the constant voltage anodization; therefore the time for the growth of the nanotubes at the positive potential limit is shorter in the first case than in the second. For instance, with a cathodic pulse duration of 30 s, the *real* time for anodization is in fact 2 h 30 min instead of 3 h as is the case of the constant voltage anodization mode. We intentionally kept the total time constant to bring out the benefits in the photolectrochemical quality of the films prepared by pulse anodization vs. the conventional anodization. Importantly, when the lower pulse limit is set at 0 V, both nanotube wall thickness and nanotube length decrease (see Table 4.2). These results demonstrate that at 0 V, the main effect is that of fluoride ions at the outer interface (oxide/electrolyte) that dissolve the TiO_2 surface by formation of highly soluble TiF_6^{2-}.

It is worth noting that long t_0 periods promote the increase of the barrier layer that in turn decreases the growth rate of the nanotube array. This is a shortcoming in any application where the length of the nanotube arrays is an important variable related to their performance, but not for those applications using UV excitation light in that the arrays are longer than the depth of light penetration (α^{-1}) into the film. As an example, a wavelength of 340 nm will have a light penetration depth (L_λ) of only 200 nm (Mollers *et al.*, 1974) while at 335 nm the L_λ value will be ~ 100 nm (Lindquist *et al.*, 1983). In both cases the light penetration depth corresponds to the inverse of the absorption coefficient, α, of the anatase TiO_2 phase (Mollers *et al.*, 1974; Lindquist *et al.*, 1983).

The nanotube walls are thicker in the 20 V/-4 V pulse anodized films than those prepared by constant anodization, indicating that these films contain a larger amount of TiO_2 per unit length. This trend is not observed when a 20 V/0 V pulse

perturbation is used in any of the four electrolytic media (see Table 4.2). The negative limit of the voltage pulse (Fig. 4.6a) and the related current transient in the pulse regime (Fig. 4.6b), both exert a crucial effect on the nanotube morphology mainly controlled by the following chemical and electrochemical reactions (equations 4.1 and 4.2). These account for the progression in layer morphology from a nanoporous structure (Fig. 4.4a) to a discrete tubular appearance (Fig. 4.4b) when the chemical dissolution process (equation 4.1) is allowed to exert its effect through the duration t_0 of the pulse at the lower voltage limit. Important to note is the fact that reaction 2 is not relevant when polyhydric alcohols are the main component of the electrolytic bath as only very little water is present to sustain the hydrogen evolution reaction.

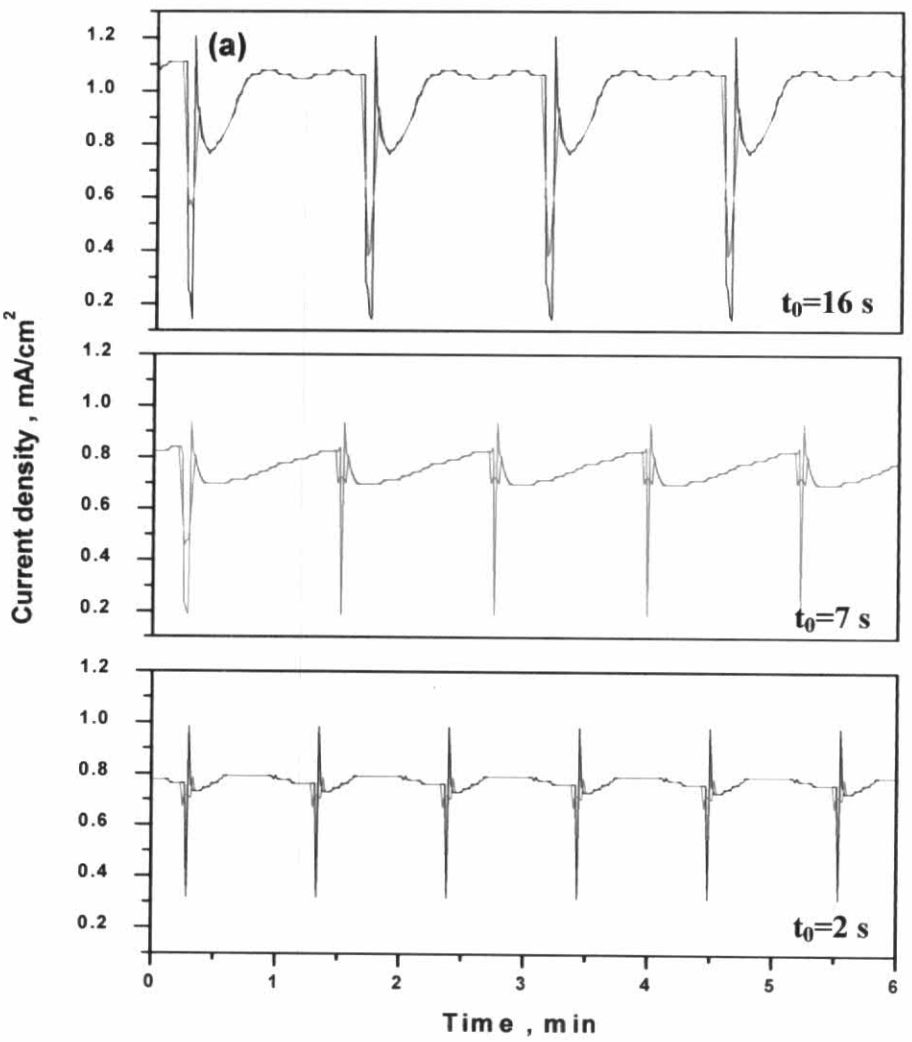

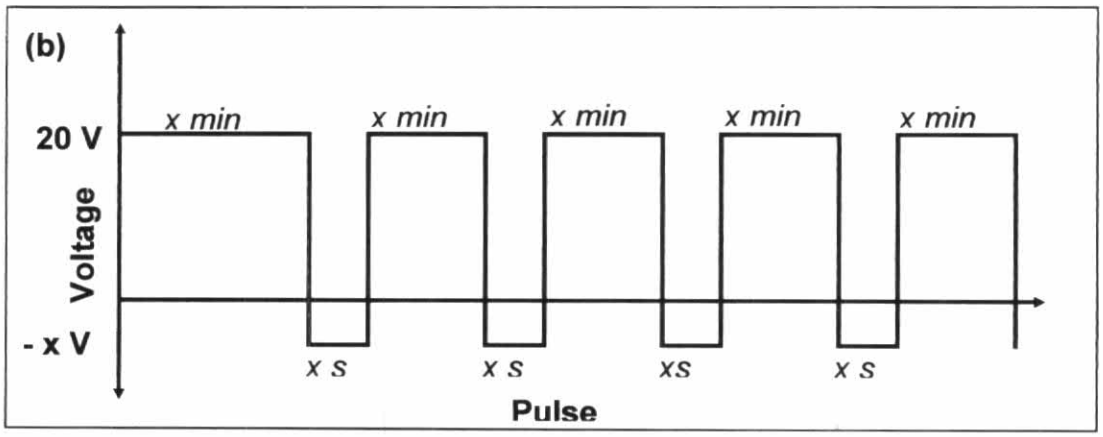

Figure 4.6 (a) Current density vs. time recorded on a Ti foil with a 20 V/ 0 V pulse waveform adjusted at pulse durations of 16, 7, and 2 s at its lower voltage limit. Electrolyte: 0.36 M NH_4F in ethylene glycol:water (90:10). (b) Schematic representation of the voltage-time waveform for pulse anodization. An initial constant time t = 5 min was applied at 20 V and then the pulse wave form is applied with time t_0 and t_1 (s) values as shown in Table 4.2

4.2.2 Effect of Pulse Limits (20 V/0 V and 20 V/-4 V). Fig. 4.7 compares the SEM morphology of TiO_2 samples prepared by pulse anodization at 20 V/0 V and 20 V/-4 V respectively. The pulse duration was 16 s in both the cases and films were grown in NH_4F/glycerol electrolyte (0.36 M) containing 10% water for 3 h. The TiO_2 nanotubes grown at 20 V/-4 V are thicker and the nanotubes are longer than those grown at 20 V/0 V (see Table 4.2).

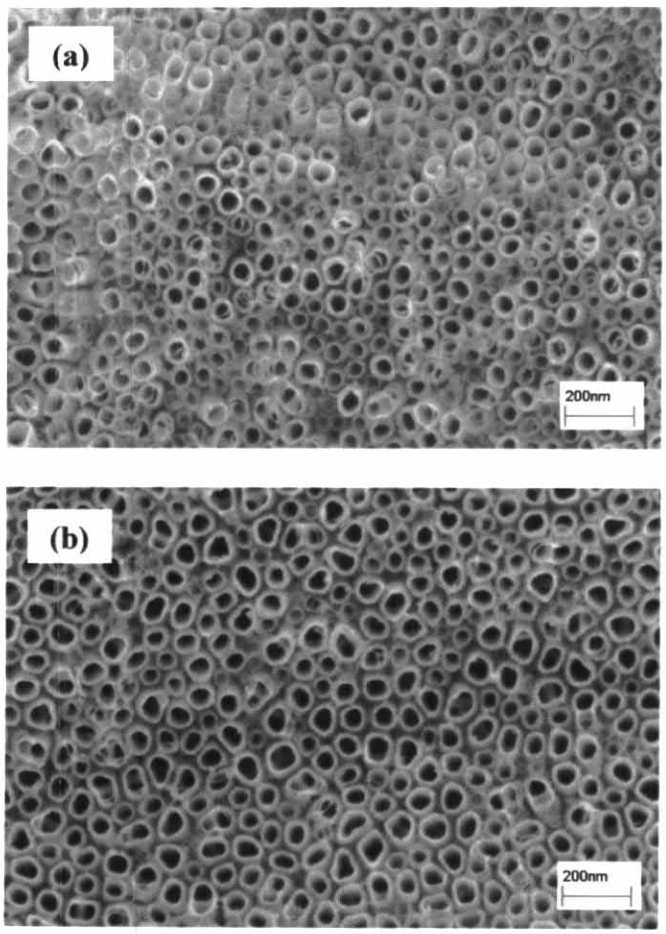

Figure 4.7 SEM images of TiO_2 nanotube arrays grown by pulse anodization (pulse duration: 16 s) in 0.36 M NH_4F electrolyte with glycerol containing 10% water at 20 V/0 V (a) and (b) at 20 V/-4 V pulse sequences.

The four processes of nanotube growth, self assembly, chemical and electrochemical dissolution must be carefully balanced. In this regard, a negative voltage limit (e.g., -4 V) serves to electrostatically induce the binding of NH_4^+/NH_3 species (equation 4.3)

This interfacial process will protect the nanotube walls against chemical etch by F^- ions or at least ameliorate the extent of it. Thus, when the lower voltage limit is set at 0 V, the protection by NH_4^+ species is less versus etching by fluoride species and the nanotube wall is slightly thinner or even not affected when compared to those prepared by constant anodization. The net result is that the samples obtained from a 20 V/0 V pulse sequence have an inferior morphology (and photoresponse quality, see below) relative to those from the 20 V/-4 V pulse mode.

4.2.3 Tuning of nanotube growth and self-Assembly via interfacial chemistry and electrochemistry. There is a corpus of both experimental (Pittman *et al.*, 1994; Pang *et al.*, 2007; and Roman *et al.*, 1991) and theoretical (Onal *et al.*, 2006) evidence for the adsorption of NH_3/NH_4^+ species on the TiO_2 surface. These include scanning tunneling microscopy evidence for ammonia adsorption on 5-fold co-ordinated Ti sites on the TiO_2 (101) surface (Pang *et al.*, 2007). Density functional theory calculations indicate the favored adsorption modes of both dissociated and un-dissociated species and the importance of H-bonding on relaxed and fixed surface oxide model clusters (Onal *et al.*, 2006).

To further elaborate the influence of the ammonium cation on nanotube array growth in our pulse anodization experiments, a series of films were prepared in PEG 400: H_2O (90:10) with 2, 7, and 16 s at the -4 V limit of the pulse. The electrolyte contained the same fluoride ion concentration (0.36 M) but variable ratios of Na^+: NH_4^+ (1:3, 1:1, and 3:1). Interestingly, replacement of NH_4^+ with Na^+ inhibited TiO_2 nanotube growth as seen by SEM. Even at a Na^+: NH_4^+ ratio of 1:3, no nanotube formation was noted under pulse anodization. Clearly, the protective (surface-passivating) effect of NH_4^+ is compromised by the presence of sodium ions at the interface. Presumably, even relatively small amounts of Na^+ in the electrical double-layer suffice to counteract the favorable influence of NH_4^+ in ameliorating chemical attack of the oxide surface by the fluoride ions.

As in our companion studies (de Tacconi *et al.*, 2006), the use of polyhydric alcohols (especially, ethylene glycol and PEG) for tuning the TiO_2 nanotube morphology is an innovative feature. The interfacial chemistry role of these alcohols and NH_3/NH_4^+ species was further probed by laser Raman spectroscopy. Fig. 4.8 contains representative spectra for TiO_2 nanotube arrays grown by pulse anodization (20 V/-4 V); the oxide surface in each case had been in contact with the corresponding electrolyte bath in which it had been prepared, i.e. NH_4F/glycerol, NH_4F/ethylene glycol, and NH_4F/PEG 400. For comparison with these three spectra, a reference spectrum containing the TiO_2 lattice phonon modes is also shown as an insert in Fig. 4.8. This particular reference sample was grown by conventional anodization (20 V, 3 h) in 0.36 M NH_4F/ethylene glycol.

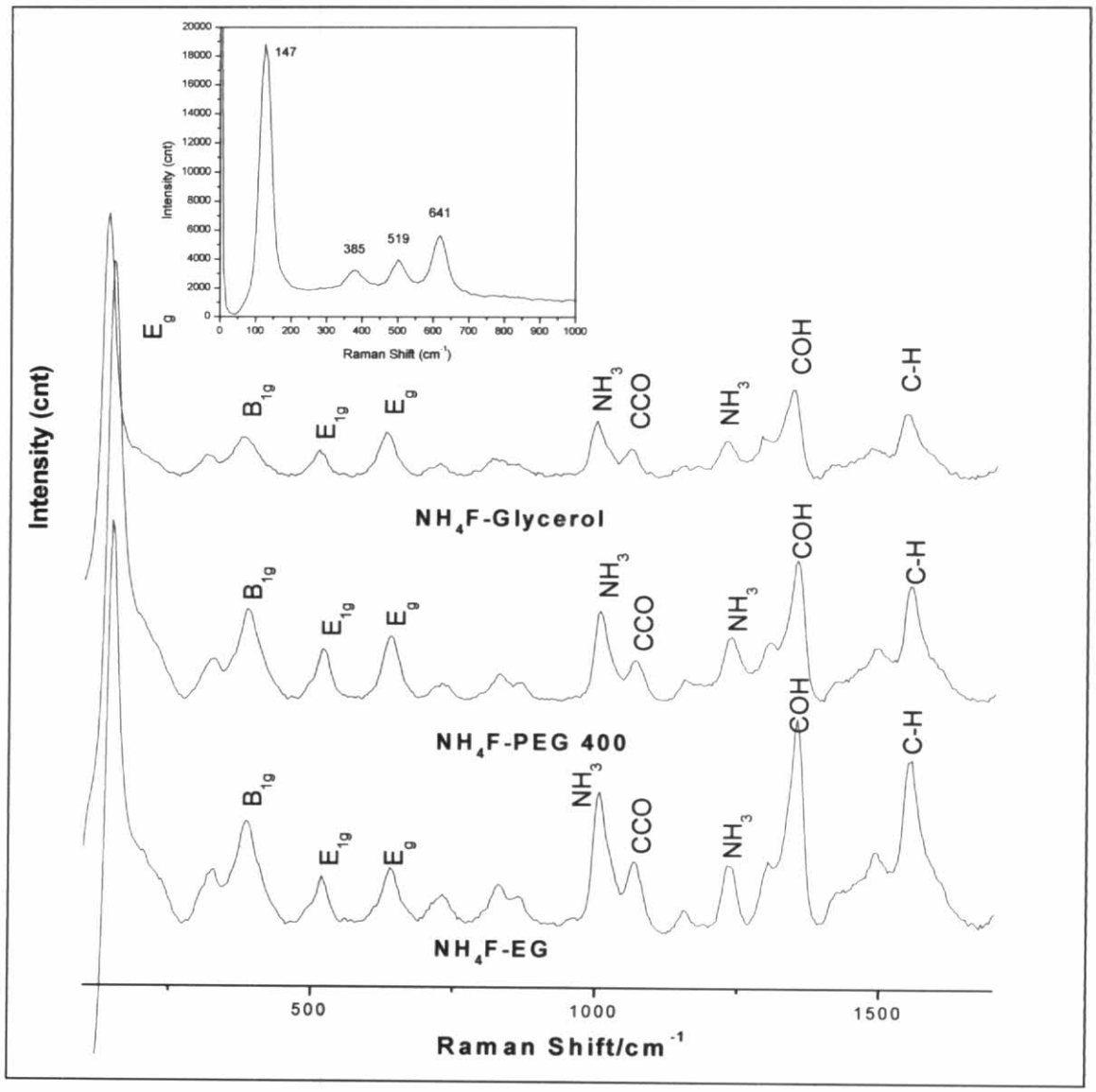

Figure 4.8 Raman spectra of TiO_2 nanotube arrays grown by pulse anodization (20 V / -4 V) in 0.36 M NH_4F/glycerol, 0.36 M NH_4F/ethylene glycol and 0.36 M NH_4F/PEG 400 for 3 h respectively. The spectra were obtained ex-situ after the films were removed from the respective electrolytic bath. For comparison, a reference spectrum of a TiO_2 film prepared with conventional anodization (20 V, 3 h) in 0.36 M NH_4F/ethylene glycol is included in the insert.

Four Raman bands are clearly seen in the reference spectrum for the "clean" TiO_2 nanotube surface at 147, 385, 519 and 641 cm^{-1} and assigned to E_g, B_{1g}, E_{1g} and E_g active modes respectively using reported reference spectra pertaining to anatase TiO_2 structure (Bersani *et al.*,1998 ; Miao *et al.*, 2004). No Raman bands related to the rutile phase are seen, as the rutile phase is characterized by bands at 143, 235, 447 and 612

cm^{-1} respectively which are not seen in this spectrum (Zhang *et al.*, 1998). No significant broadening or shifts were found when compared to the anatase TiO_2 powder. Observe that in the spectra for TiO_2 nanotubes after being in contact with the preparative electrolyte, the bands for anatase TiO_2 nanotubes are also clearly discernible although slightly shifted (< 10-15 nm).

Particularly significant to note in the three spectra in Fig. 4.8 are the bands assignable to the presence of NH_3/NH_4^+ species. Thus the band at 999.8 cm^{-1} is assigned to NH_3 by analogy with the theoretically predicated band for free ammonia at 964.3 cm^{-1} (Harzberg, 1945). The band at 1228.0 cm^{-1} in NH_4F/glycerol is assignable to NH_3 (symmetric bending mode); this band is seen to shift to higher numbers when the coverage by ammonia on TiO_2 increases and was reported at 1220 cm^{-1} for TiO_2 anatase (Hadjiivanov *et al.*, 1997). The bands at 1428 and 1480 cm^{-1} are assigned to the ammonium ion by comparison with similar bands located at 1415 and 1465 cm^{-1} respectively for the ammonium cation in NH_4SO_4 (Jarawaia *et al.*, 2007).

The Raman bands traceable to the three alcohols have a high degree of resemblance; for example, the COH deformation appears at 1343.7 cm^{-1} for adsorbed glycerol and at 1354.5 cm^{-1} for both ethylene glycol and PEG 400. The CCO vibration modes appear at 1059.2 cm^{-1} and 1145 cm^{-1} for glycerol and at 1070.3 and 1157.3 cm^{-1} for the other two alcohols. The band at 1542.8 cm^{-1} in glycerol is tentatively assigned to C-H vibrations, appearing slightly shifted to 1553.3 cm^{-1} for ethylene glycol and PEG 400 although in the latter, the band is significantly more intense when compared to the intensity of the TiO_2 signature bands. These band assignments are supported by literature data on the three polyhydric alcohols (Mendelovici *et al.*, 2000; Djaoued *et al.*, 2005; and Luo *et al.*, 2001).

4.2.4 Effect of pulse duration. Fig. 4.9a shows the surface morphology of a sample prepared by conventional anodization (20 V, 3 h) in 0.36 M NH_4F/ethylene glycol:H_2O (90:10). Individual groups of nanotube arrays are seen separated by big crevices as if uncontrolled chemical/electrochemical etching of the nanotube walls had occurred and the nanotube array formation was unable to develop on the entire substrate surface. There are apparent patches with non-porous structure and also some cloudy precipitates covering the surface. However, Fig. 4.9b shows the surface morphology obtained under the same electrolytic conditions but with 20 V/0 V pulse anodization using a pulse duration t_0=16 s at the lower voltage limit. Large areas

covered with the self-organized nanotube arrays and much less cloudy precipitate on top of the nanotube arrays was found compared to the previous case (c.f., Figs. 4.9a and b).

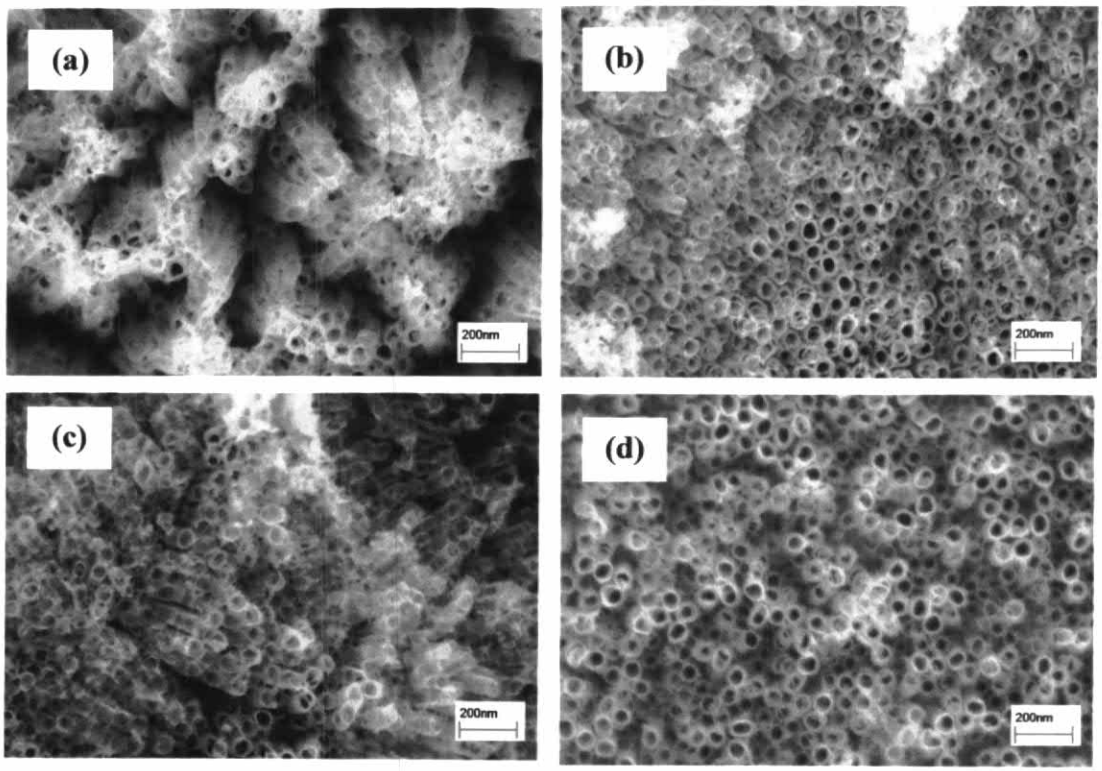

Figure 4.9 Comparison of SEM images of nanotube arrays of TiO_2 grown by conventional anodization (20 V, 3 h) in 0.36 M NH_4F/ethylene glycol (a) and by pulse anodization (20 V / 0 V) with t_0 = 16 s (b), t_0 = 7 s (c), and t_0 = 2 s (d) respectively.

Anodization using shorter pulse duration (t_0 = 7 s) yielded well structured areas of nanotube arrays covering almost the entire surface (Fig. 4.9c). The amount of precipitates on top of the self-organized nanotubes is negligible. Interestingly much shorter pulse duration (t_0 = 2 s) gave a regular porous structure consisting of organized nanotubes with uniform single pore diameters of approximately 69-71 nm (Fig. 4.9d). Interestingly, nanotubes prepared by pulse anodization using short t_0 pulse durations were longer than those from longer t_0 and from a constant voltage mode (see Table 4.2). The related photocurrent data reflect this morphology (Table 4.2, column 8).

The current transients recorded during the formation of nanotube arrays depicted in Figs. 4.9b-d are shown in Fig. 4.6b with the corresponding three t_0 values indicated at the top right corner of each current profile. When the anodization voltage

is applied, the current increases and reaches a steady level while the barrier layer is reaching a thickness corresponding to nanotube formation. When the voltage is suddenly changed to the lower limit of the waveform the current density is seen to decrease drastically to very small values because the electrochemical growth/dissolution of the nanotube arrays is very low. Hence in this pulse period t_0, oxide formation is almost negligible, and the main processes in this period is the interaction of the growing nanotubes with F^- and NH_4^+ species, these two species affecting chemical dissolution of the oxide. When the voltage is again increased the current density will reach a steady level and the oxide starts forming again.

Thus the formation of nanotubes will occur more slowly avoiding cracking of the surface. This also prevents the nanotubes from clumping together, as well as eliminating cloud formation on the nanotube surface from rapid oxide formation (Mor *et al.*, 2006). With 0 V as the lower potential of the waveform the effect of fluoride chemical dissolution is more marked than in the case of -4 V. Once again, a negatively polarized oxide film promotes the electrostatic attraction of NH_4^+ that in turn slows down the oxide being chemically etched by fluoride (see above).

4.2.5 Photoelectrochemical performance. The photoelectrochemical response of the TiO_2 nanotube films was assessed using linear sweep photovoltammetry (Rajeshwar, 2002; and Zhou *et al.*, 1996) in 0.5 M Na_2SO_4 supporting electrolyte. Fig. 4.10. shows representative photovoltammograms for TiO_2 nanotube arrays prepared by conventional anodization in 0.36 M NH_4F at 20 V for 3 h (entry 1, Table 4.2) (Fig. 4.10a), nanotube arrays prepared by pulse anodization using pulse duration (t_0=30 s) at 20 / -4 V for 3 h (entry 5, Table 4.2) (Fig. 4.10b), and samples from pulse anodization (t_0=30 s) in 0.36 M NH_4F/ PEG 400 at 20 / -4 V for 3 h (entry 29, Table 4.2) (Fig. 4.10c).

The TiO_2 nanotubes grown by pulse anodization showed superior photovoltammetry profiles in both cases compared to their counterpart grown at constant anodization voltage. This trend reflects better e^- - h^+ pair separation and transport in the former cases. Clearly the nanoarchitecture morphology and photoresponse are directly linked underlining the rationale for using nanotube arrays in photoelectrochemical and solar energy conversion applications.

A figure-of-merit indicator of the quality of photoelectrochemical response is the photocurrent density value at the plateau region of the photovoltammograms (see

Fig. 4.11). Such values are contained in Table 4.2 (column 8). The photoelectrochemical response of TiO_2 films prepared under constant (20 V) and pulse (20 V/-4 V or 20 V/0 V) polarization are shown in Figs. 4.11a and b respectively. The data are shown in bar graph format comparing photocurrent densities for the various samples (at a reverse bias potential of + 1.5 V vs. Ag|AgCl reference in 0.5 M Na_2SO_4 supporting electrolyte) on the z-axis and pulse duration on the x-axis. The photocurrent densities are higher by ~12% - ~45% for the puls (20 V/-4 V) anodized nanotube arrays relative to samples obtained from the conventional, continuous anodization approach and by 7% -15% for pulse anodization at 20 V/0 V.

The lower photocurrent densities in films prepared by constant anodization are likely related to the fact that these films are made of thinner nanotube walls than those prepared by pulse anodization. These thinner walls imply that smaller amounts of charge are collected in the back contact because of two factors: slow charge transport through the walls and accelerated recombination due to a high concentration of injected electrons. There is precedence for the observation of lower photocurrent efficiency at thin nanotube walls (less than 5 nm) in ZnO nanotubular photoanodes grown in anodic aluminum oxide template (Martinson *et al.*, 2007).

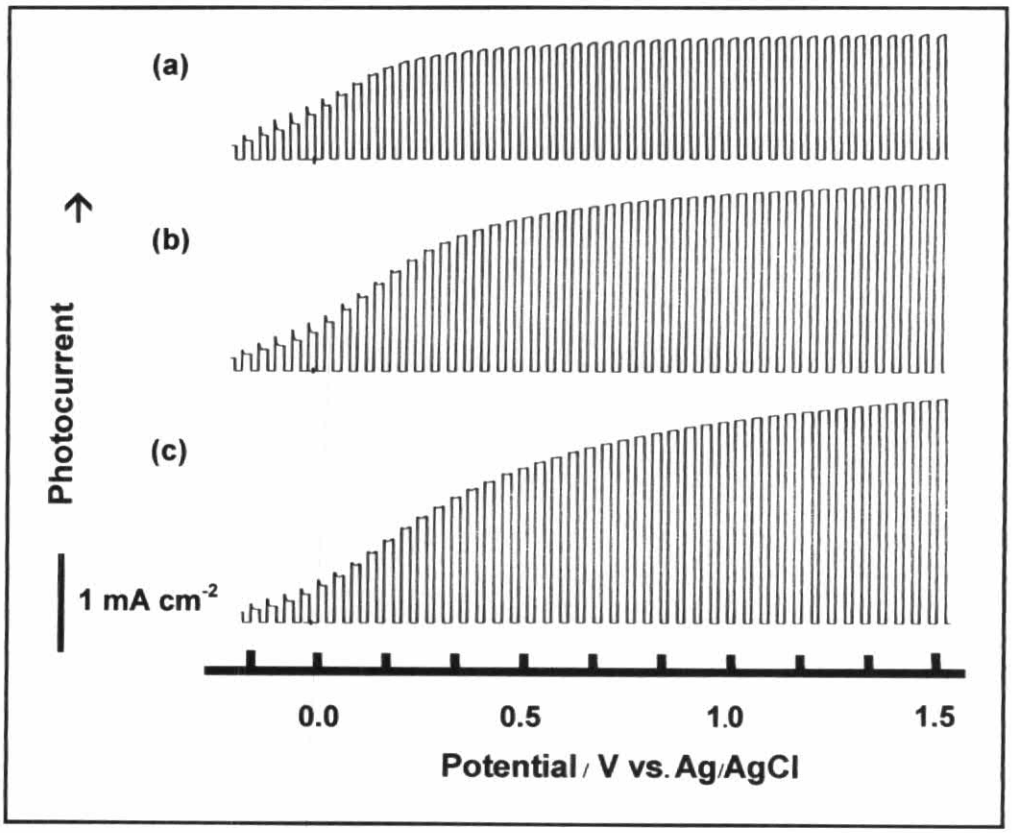

Figure 4.10 Linear-sweep photovoltammograms with 0.1 Hz chopped irradiation of a nanoporous TiO_2 film in 0.5 M Na_2SO_4. The films were obtained by conventional anodization (a) in 0.36 M NH_4F, 20 V for 3 h and (b) pulse anodization with t_0 = 30 s at -4 V/20 V in 0.36 M NH_4F, and (c) pulse anodization with t_0 = 30 s at -4 V/20 V in 0.36 M NH_4F/PEG 400. Photovoltammograms were obtained at 2 mV/s using the full output of a 150 W Xe lamp.

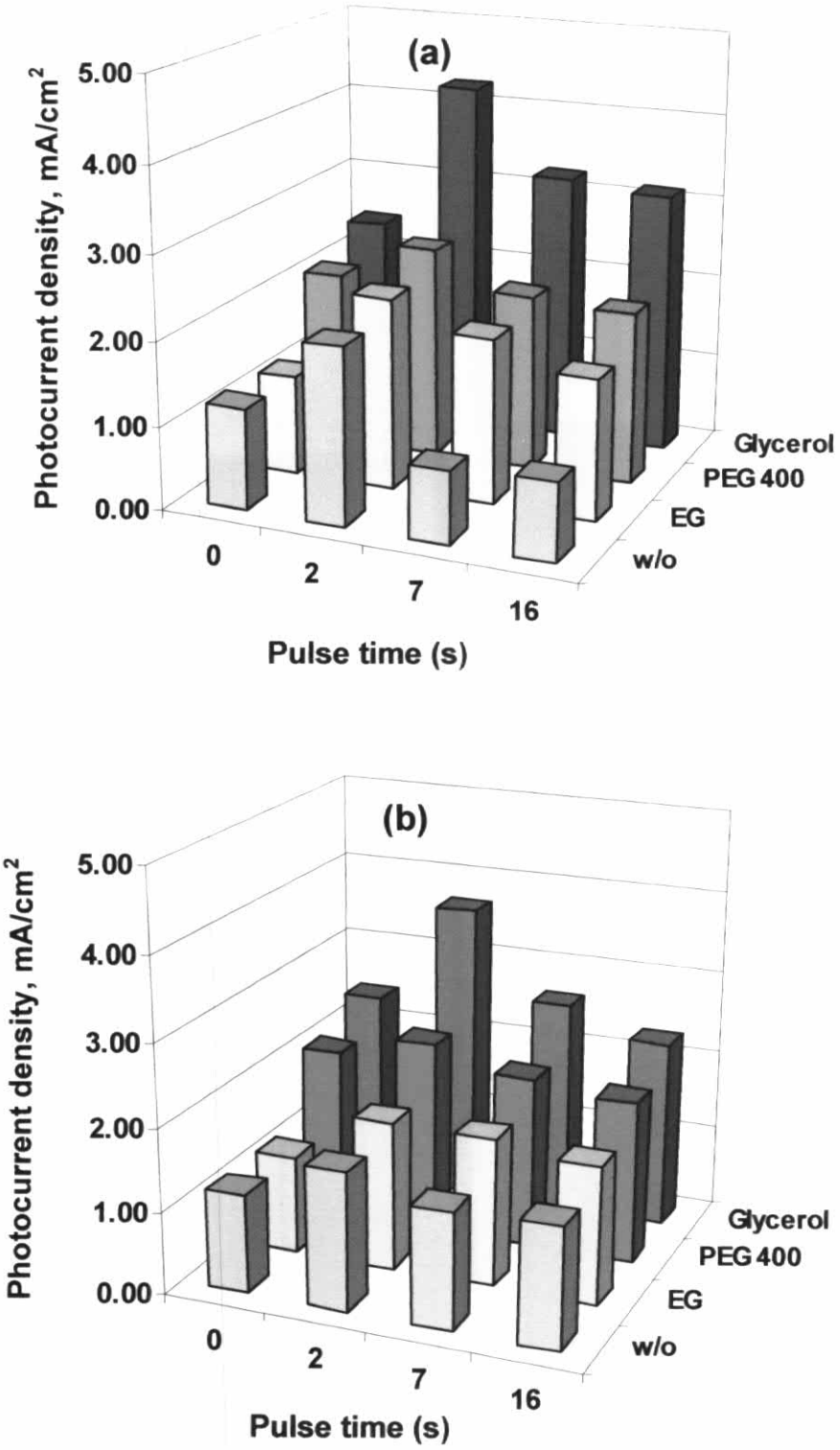

Figure 4.11 Bar graphs comparing photocurrent densities at a reverse bias potential of + 1.5 V (vs. Ag|AgCl reference) in 0.5 M Na_2SO_4 supporting electrolyte for films prepared without and with different media modifiers by conventional anodization (20 V, 3 h) and by pulse anodization for duration between 2-16 s at 20 V/-4 V (a) and 20 V/0 V (b).

Importantly, note in Fig. 4.11a that the highest photocurrent in each medium modifier (glycerol, ethylene glycol and PEG 400) was obtained for a pulse duration of 2 s. Reference to Table 4.2 indicates that this pulse duration generates a comparable wall thickness with values of 15.6 ± 0.5 nm for glycerol and 15.4 ± 0.5 nm for both ethylene glycol and PEG 400. This finding suggests that a nanotube wall thickness of 15.5 nm is optimal for good photoelectrochemical performance.

In terms of the comparative effect of the three medium modifiers (glycerol, ethylene glycol and PEG 400) on the resulting photoelectrochemical performance of TiO_2 nanotube arrays, those from glycerol perform the best for water photo-oxidation. These nanotubes have diameters ranging from 60 ± 2 nm to 83 ± 2 nm depending on the anodization waveform, and these dimensions seem optimal for not getting blocked by O_2 bubbles generated inside the tubes. Larger nanotube diameters such as those generated from PEG 400 do not perform better than those from glycerol. Thus the medium modifiers clearly play a role in the nanotube wall thickness, diameter and length under different waveform potentials and durations (see Fig. 4.5) and these variables, in turn, impact the photoelectrochemical response. The interfacial effect of these medium modifiers is not limited to solution viscosity changes (Macak *et al.*, 2005). The present study has clearly shown that polyhydric alcohols can interact with the growing oxide surface (Fig. 4.8). Additionally, they can reduce the water activity in the growth medium. For example, glycerol and ethylene glycol have been used as water activity depressor agents.

Importantly, the breakdown of organic solvent at the negative pulse limit could play an important role in nanotube formation and subsequent photoelectrochemical performance. In fact, there are clear differences in the photocurrent performance for films prepared using the same pulse waveform in the three polyhydric alcohols (see Figs. 4.10 and 4.11). For example, for a pulse limit of -4V (2 s), the three resulting films share similar nanotube wall thickness but the photocurrent is almost double for the film prepared from glycerol.

4.3 Metal-modified TiO_2 nanotubes

The primary driving force in this research was to study the photoelectrochemical properties of TiO_2 nanotube and the effect of metal dopants on TiO_2 nanotube performance. In photocatalytic behaviour, it is the photon-generated electron/hole (e^-/h^+) pairs that can facilitate redox reactions on the surface. The total number of free carriers on the surface determines the efficiency of catalysts. The number and the lifetime of free e^-/h^+ are particle size and dopant-dependent. For large particles, the volume recombination of electrons and holes dominates. This condition largely reduces the number of free charges on the surface and deteriorates the photocatalytic activity. For nanotube, the transportation length of e^-/h^+ from crystal interface to the surface is short, which helps to accelerate the migration rate of e^-/h^+ to the surface of the nanotube to participate the reaction process. For optimal photocatalysis efficiency, there is a critical particle size below which the surface recombination of electron and hole becomes dominant because of the increased surface-to-volume ratio. Besides the effect of morphology on the photocatalytic activity, the role of dopant is important. Different dopants may not have the same effect on trapping electrons and/or holes on the surface or during interface charge transfer because of the different positions of the dopant in the host lattice. Consequently, the photocatalytic efficiency would be divert for different types of dopants. In this study, we describe the effect of metal ions Li^+ ,Ni^{2+}, Mn^{3+}, $V^{4+}$and Nb^{5+} dopants and co-doped such as ethyl glycol, glycerol, and poly(ethyl glycol) 400 on the photocatalytic activity of TiO_2 nanotube.

In this study, it is indicated that metal-modified TiO_2 nanotubes posed higher photoactivity than that corresponding to simple TiO_2 nanotube. The optimum condition in TiO_2 nanotube synthesis was previously described and transferred for metal-modified TiO_2 nanotubes by using pulse anodization adjusting the pulse time at negative (-4 V) from 2-15 seconds in different metal loadings between 10-40%. The experiments were separated into 3 parts as follow: (1) investigation of optimum metal loading, (2) investigation of optimum pulse time, and (3) investigation of effect of media modifier during the formation of the semiconductor nanotubes. Media modifiers included glycerol, ethylene glycol, and poly ethylene glycol 400. The

optimum condition in each run was judged by photocurrent density. The results could be separated in three groups as shown below

4.3.1 Photoelectrochemical response of group 1: Li^+

The successful electrode of the metal-modified TiO_2 nanotube example of the Li-modified photocatalyst in photoelectrochemical response obtained by alkaline metal ion doping was introduced below. Fig. 4.12 shows the photocurrent action spectra (IPCE versus excitation wavelength) of five selected electrodes at the electrode potential of 1.40 V as determined in aqueous solution of Na_2SO_4 (0.5 M). The incident photon conversion efficiency (IPCE) was determined from the equation 3.1 in chapter 3.

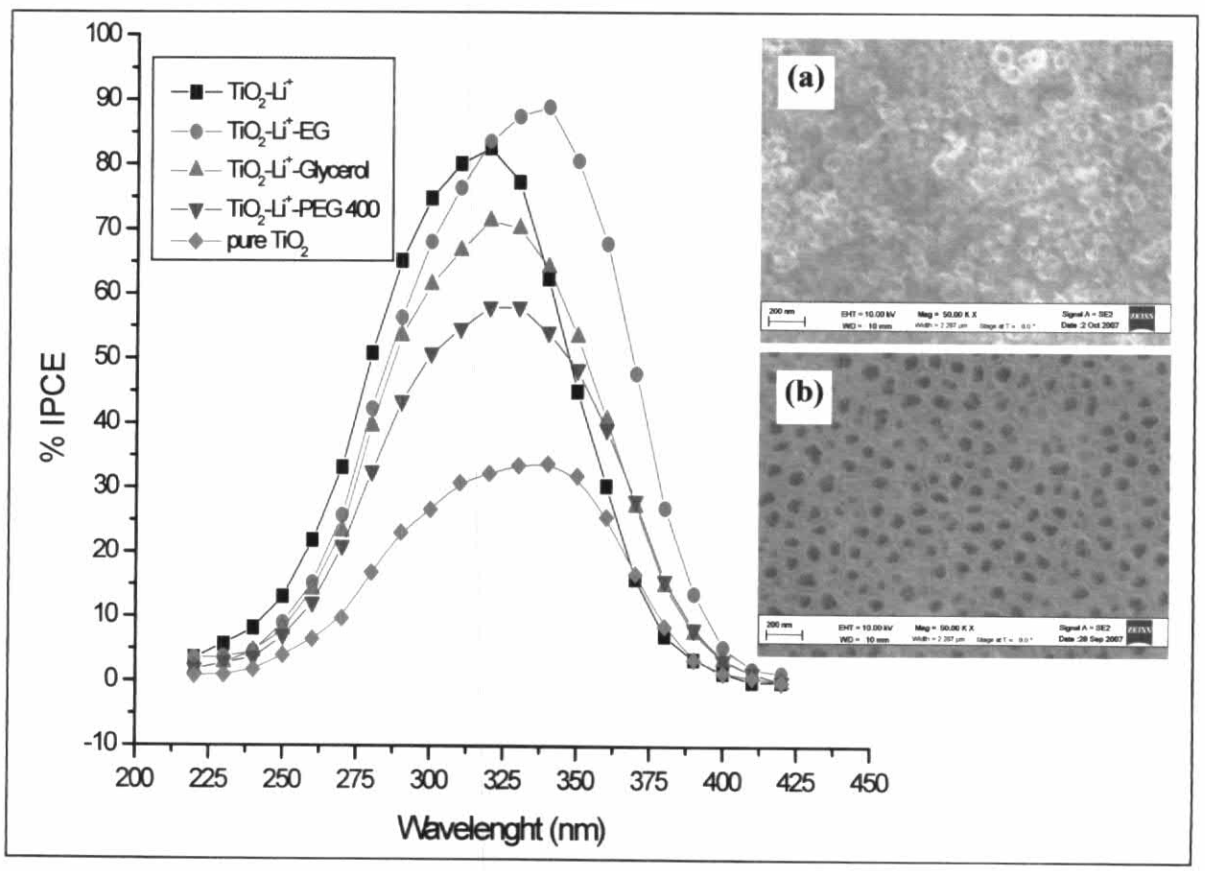

Figure 4.12 Photoaction spectra for Li^+-doping TiO_2 nanotube electrode with different co-doping. The inserts show the corresponding TiO_2 morphology, (a) pure TiO_2; (b) TiO_2 films doped with Li^+ with poly ethylene glycol as co-dopant.

The photocurrent action spectra are shown in Fig. 4.12. The result show that the IPCE reached as much as 90% at the wavelength of 320 nm with a red shift of the incident light. These results correspond to the fraction of the photons absorbed by the TiO_2 nanotube that are converted into conduction band electron of TiO_2. All Li-metal doped TiO_2 electrodes have the IPCEs larger than that of pure TiO_2. The insert pictures are the SEM micrographs of pure TiO_2 electrode and doped TiO_2 films as prepared in 20% w/v of LiF with ethyl glycol as co-doping species. A homogenous structure could be observed form the doped TiO_2 film. These results indicate that the dopant has significant effect on the morphology of the TiO_2 film. The homogenous morphology might associate the efficient separation of photogenerated electron-hole pairs as well. In this work, the Li-metal doped TiO_2 electrode without co-doping provided IPCE as high as 80% at the wavelength 320 nm. The IPCEs were lower by the addition of various organic species as glycerol, PEG 400 which play role as co-dopant. The exception was seen when using ethylene glycol as co-dopant. The co-dopants not only exert the IPCE decreasing effect but also narrow the band gap as described below.

The photocurrents of metal-ion-doped TiO_2 electrodes and band gap were shown in Table 4.3(electrode potential 1.40V). The band gap energy values, ε_g, of the five films, could be calculated using the following relationship equation 4.4 (Bignozzi *et al.*, 2000):

$$(\text{IPCE} \times h\nu)^{1/2} \propto (h\nu - \varepsilon_g) \qquad \text{(Eq. 4.4)}$$

The data from Fig. 4.13 were plotted as $(\text{IPCE}\times h\nu)^{1/2}$ versus $h\nu$. To determine the band gap of each sample, the variation of $(\text{IPCE}\times h\nu)^{1/2}$ with excitation energy (hv) was obtained using the IPEC data for the various films. Intercepts of the Tauc plots show the approximate values of the optical band gap (Eg) for the five different series. These plots are shown in Fig. 4.13, where pure TiO_2 serves as the reference with a band gap value (3.1 eV) and 2.85-2.90 eV for the Li modified TiO_2 nanotube film.

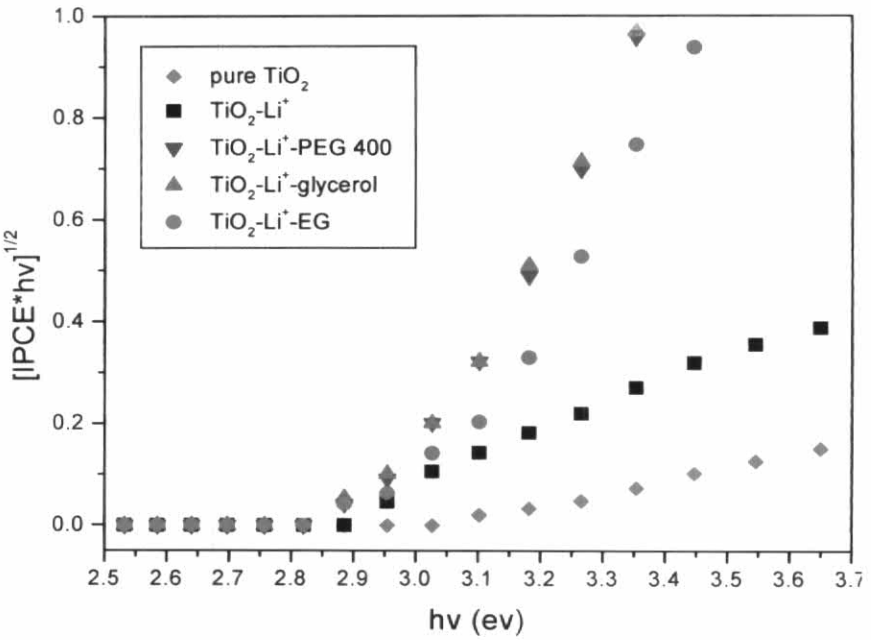

Figure 4.13 Band-gap estimation for Li^+-doping TiO_2 nanotube electrode with different co-doping, according to equation 4.4.

Table 4.3 The photocurrents and band gap of Li^+-doping TiO_2 nanotube electrode with different co-doping.

Electrode	Photocurrent density (mA/cm^2)	Band gap (eV)
Pure TiO_2	4.29	3.10
TiO_2-Li^+	7.54	2.90
TiO_2-Li^+-EG	10.24	2.85
TiO_2-Li^+-Glycerol	9.37	2.85
TiO_2-Li^+-PEG 400	7.86	2.85

It can be seen that the photocurrents of all Li modified TiO_2 nanotube electrodes were smaller than that of pure TiO_2 electrode. There are two main causes that may explain the difference observed in the photocatalytic activity of these films. Firstly, Li^+ had the radius as equivalent as the Ti^{4+} (68×10^{-12}), thus it can penetrate easily into the crystal lattice of the TiO_2. The replacement of the Li^+ was beneficial to the generation of photogenerated surface oxygen vacancies and the transition of electron at the surface. Secondly, the maximum IPCE at the Li-modified electrode

may be due to the doping concentration of Li ions in TiO_2 nanoparticles for separation of photogenerated electron-hole pairs reach the optimal condition. Tsevis *et al.* (1998) reported that the value of the space charge region potential for the efficient separation of electron-hole pairs must be not lower than 0.2 V. As the concentration of dopant ions optimum, the surface barrier becomes higher and the space charge region narrower, the electron-hole pairs photogenerated within the region are efficiently separated by the large electric field before recombination. On the other hand, when the concentration of doping ions is too low, the space charge region become very narrow and the penetration depth of light into TiO_2 greatly exceeds the space charge layer, so the recombination of the photogenerated electron-hole pairs in semiconductor become easier.

4.3.2 Photoelectrochemical response of group 2 : Mn^{3+}, Nb^{5+}

Figs. 4.14 shows the photocurrent action spectra (IPCE versus excitation wavelength) of metal-modified TiO_2 nanotubes using Mn^{3+} and Nb^{5+}. The electrode potential was 1.40 V as determined in aqueous solution of Na_2SO_4 (0.5 M). The intensity of UV light source (150Wxenon arc lamp) served as the light source in the photovoltammetry experiments was in the range 0.59 mW/cm^2 at 340 nm with a bandwidth of 4 nm. The photon flux was monochromatically measured on an Oriel model 70260 Radiant Power/Energy meter.

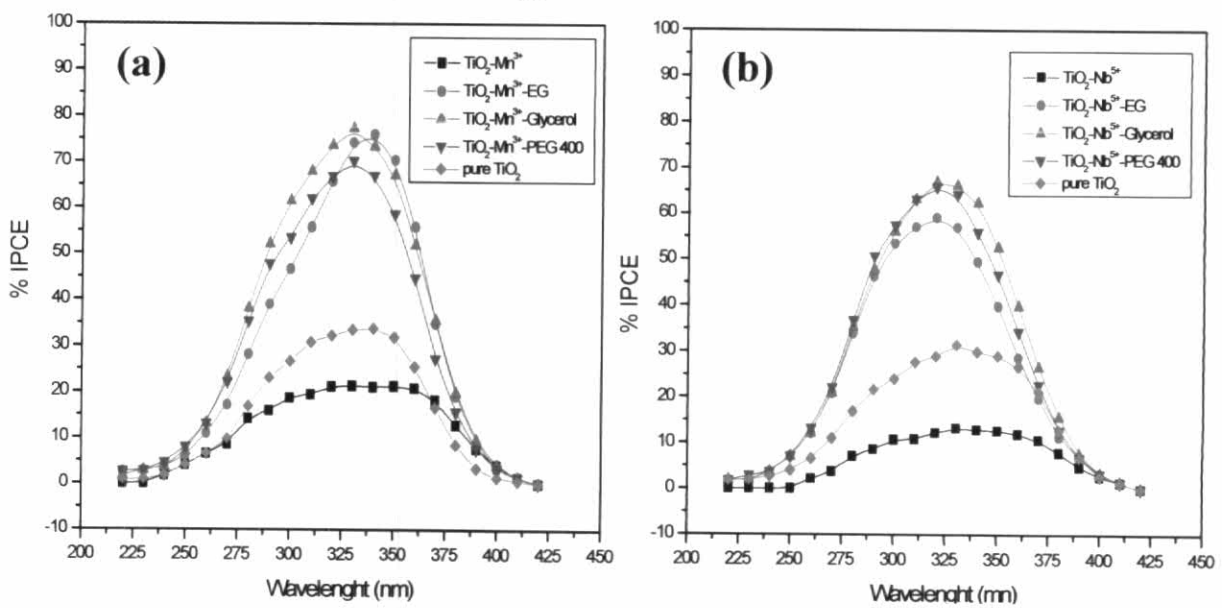

Figure 4.14 Photoaction spectra for (a) Mn^{3+} ; (b) Nb^{5+}-doping TiO_2 nanotube electrode with different co-dopant.

From IPCE values, it is seen that the Mn^{3+}- or Nb^{5+}-modified TiO_2 nanotube can provide the IPCE as high as 70-80% in the presence of co-doping species. All metal doped TiO_2 electrodes with co-dopant have the IPCEs larger than those of pure TiO_2 and TiO_2 without co-dopant. This information introduces that in doping metals with three valence electron to the TiO_2 nanotube, the co-dopant is necessary to increase the photoreactivity of titania nanotube. The photocurrents of metal-ion-doped TiO_2 electrodes and band gap were shown in Table 4.4 (electrode potential 1.40V). It can be seen that the photocurrents of modified TiO_2 nanotube electrodes which prepared with co-doping were at least two fold larger than that of pure TiO_2 electrode, and the band gap energy narrow than pure TiO_2 nanotube.

When only Mn^{3+} and Nb^{5+} were doped into TiO_2 nanotube, less activity was obtained. This behaviour might come from the fact that Mn^{3+} and Nb^{5+} were works as a recombination site (Shah *et al.*, 2002). However when added the co-doped EG, glycerol, and PEG 400 in electrolyte, the formation of metal modified were increase photocurrent action. These co-doping species might be contributed to the absorption of metal to forming an electron donor level (Kudo *et al.*, 2007), due to keeping of the charge balance and protected TiO_2 nanotube to against with F^- in electrolyte. As shown in Figs. 4.15.

Table 4.4 The photocurrents and band gap of $Mn^{3+}$and Nb^{5+} doping TiO_2 nanotube electrode with different co-doping.

Electrode	Photocurrent density (mA/cm^2)	Band gap (eV)
Pure TiO_2	4.29	3.20
TiO_2-Mn^{3+}	2.54	2.85
TiO_2- Mn^{3+}-EG	8.33	2.85
TiO_2- Mn^{3+}-Glycerol	8.73	2.85
TiO_2- Mn^{3+}-PEG 400	6.98	2.85
Pure TiO_2	3.57	3.10
TiO_2-Nb^{5+}	1.90	2.90
TiO_2- Nb^{5+}-EG	9.37	2.90
TiO_2- Nb^{5+}-Glycerol	8.73	2.90
TiO_2- Nb^{5+}-PEG 400	7.70	2.90

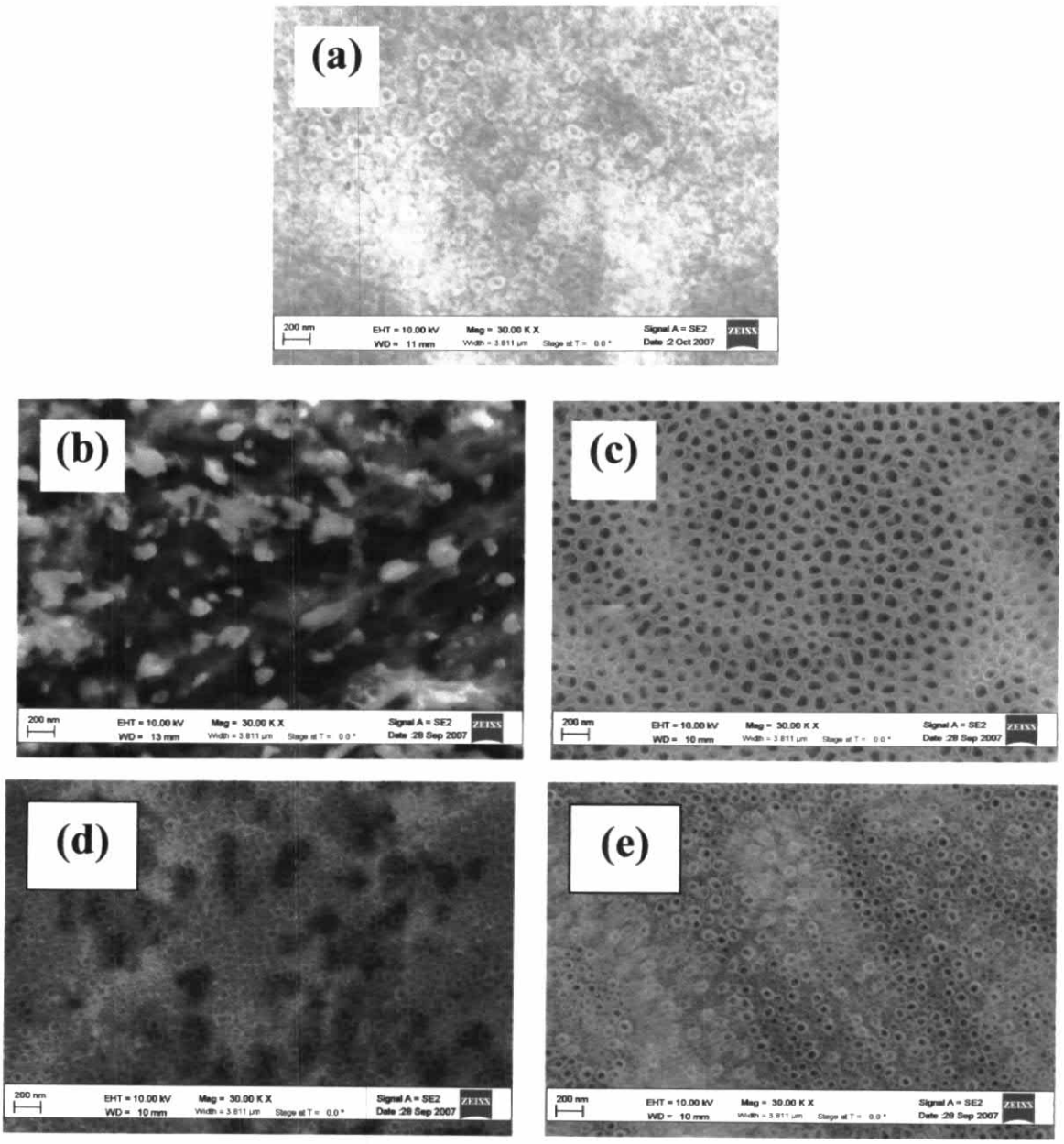

Figure 4.15 SEM image of (a) Pure TiO_2 films; (b) TiO_2 films doped with Nb^{5+} without co-doping; (c) TiO_2 films doped with Nb^{5+} with poly (ethylene glycol); (d) TiO_2 films doped with Nb^{5+} with ethylene glycol; (e) TiO_2 films doped with Nb^{5+} with glycerol as co-dopant.

Effects of co-dopants on Nb^{5+}-doped TiO_2 nanotube is clearly seen in Figs. 4.15. In addition, photocatalytic activities are affected by particle size, crystallinity, surface properties, etc. These factors are controlled by changes in a preparation method. Co-doping of metal modified in photocatalyst is one of the various factors that can affect the morphology (particle size and surface structure) of photocatalyst.

The homogenous morphology can prevent charge recombination and results in an extension in the lifetime of the active holes due to the relatively high specific surface area (Park *et al*, 2004). Doping of transition metal cations into photocatalyst with wide band gaps such as TiO_2 modify electronic structure and develop materials with light responses. As a result, the photocatalytic activity of the films was increased. Due to Mn^{3+} and Nb^{5+} have similar energy levels in the TiO_2 lattice, similar ionic radii and identical oxidation states (ionic radius of Mn^{3+}, $Nb^{5+} = 66\times10^{-12}$, 69×10^{-12} respectively), it is quite possible that the p-state contributed to band gap narrowing by mixing with p-states of oxygen (Saponjic *et al.*, 2006).

4.3.3 Photoelectrochemical response of group 3: Ni^{2+}, V^{4+}

Fig. 4.16 shows the photocurrent action spectra (IPCE versus excitation wavelength) of two metal modified TiO_2 nanotubes

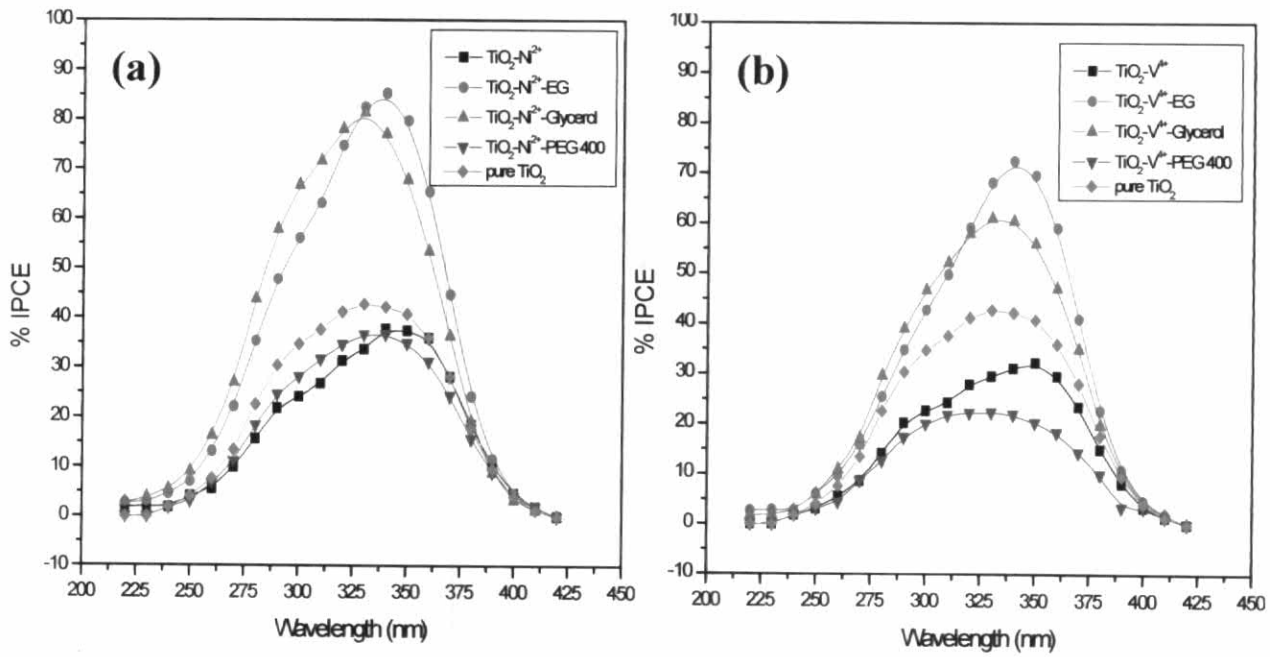

Figure 4.16 Photoaction spectra for (a) Ni^{2+} ; (b) V^{4+}-doping TiO_2 nanotube electrode with different co-doping.

When only Ni^{2+} and V^{4+} were deposited on the TiO_2 surface, less activity was obtained. As a result, the photocatalytic activity of the films was decreased. However

when added in the co-doped such as EG and glycerol, the photocurrents of metal modified structure were increase. Co-dopant could be contribute to absorption of metal to forming an electron donor level which most of the Ti^{4+} would be replaced and a large number of the electron-hole pairs be trapped, due to keeping of the charge balance and protected TiO_2 to against with F^- in electrolyte (Macak *et al.*, 2006) (shown in Fig. 4.17).

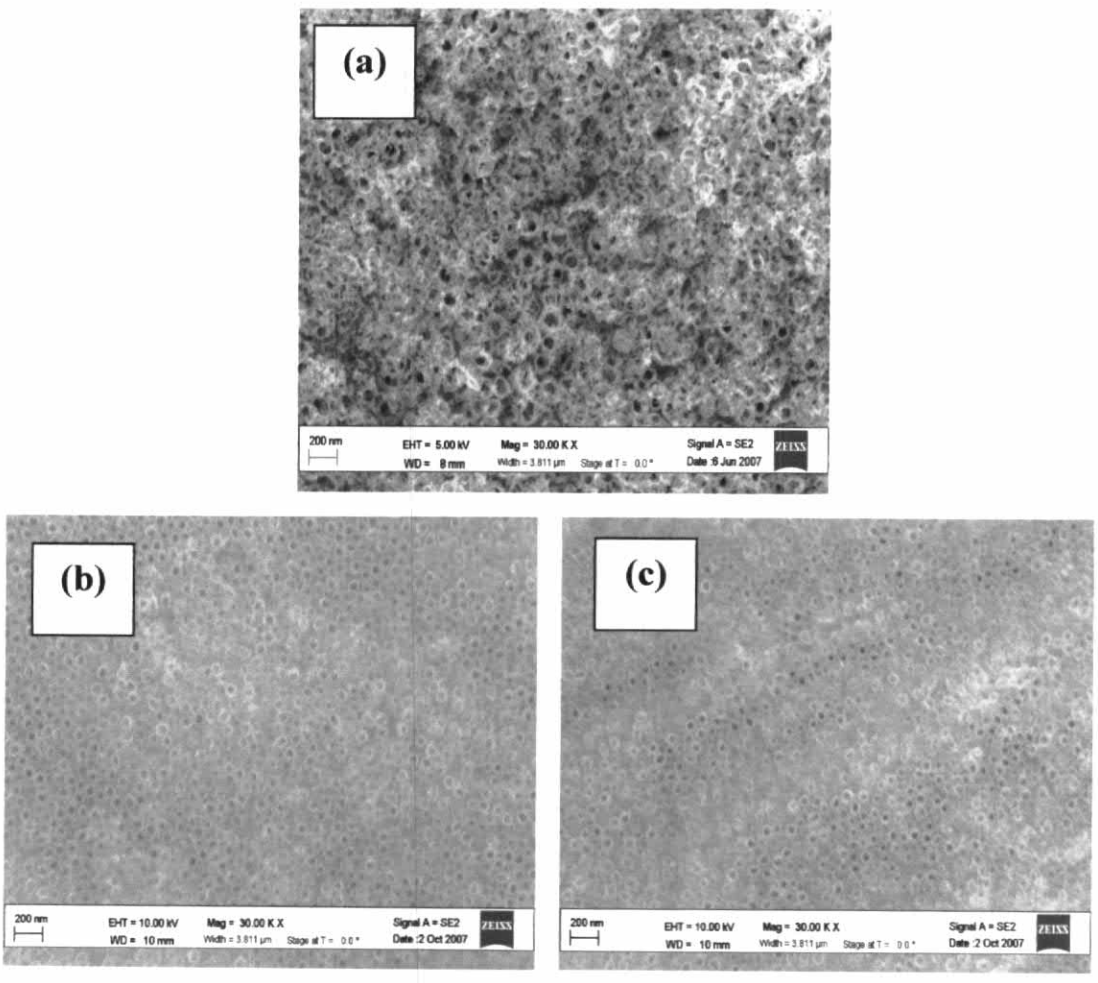

Figure 4.17 SEM image of (a) Pure TiO_2 films; (b) TiO_2 films doped with V^{4+} with glycerol; (c) TiO_2 films doped with V^{4+} with ethylene glycol as co-dopant.

From Fig. 4.17, it is attributed that the high surface area of TiO_2 nanotube doped with V^{4+} and the specific co-dopant as EG or glycerol make indirect band electron transition possible and increase the generation rate of electrons and holes. Increase of the generation rate of charge carriers is one way to enhance the photocatalytic activity (Raja *et al.*, 2007). On the other hand, electron and hole trapping during their transportation from the interior of the particle to the surface is also very crucial to preventing the recombination of electron and hole pairs (Macak *et al.*, 2006).

The photocurrents of metal-ion-doped TiO_2 electrodes and band gap were shown in Table 4.5 (electrode potential 1.40V). It can be seen that the photocurrents of modified TiO_2 nanotube electrodes which prepared with ethylene glycol and glycerol as co-doping were larger than that of pure TiO_2 electrode, and the band gap energy narrow than pure TiO_2 nanotube.

Table 4.5 The photocurrents and band gap of Ni^{2+} and V^{4+} doping TiO_2 nanotube electrode with different co-doping.

Electrode	Photocurrent density (mA/cm^2)	Band gap (eV)
Pure TiO_2	5.79	3.20
TiO_2-Ni^{2+}	3.57	3.20
TiO_2-Ni^{2+}-EG	8.17	3.10
TiO_2-Ni^{2+}-Glycerol	8.65	3.10
TiO_2-Ni^{2+}-PEG 400	4.60	3.10
Pure TiO_2	5.79	3.20
TiO_2-V^{4+}	3.80	3.10
TiO_2-V^{4+}-EG	6.27	3.10
TiO_2-V^{4+}-Glycerol	7.54	3.10
TiO_2-V^{4+}-PEG 400	2.78	3.10

Possible explanations could be based on the change of potential energy level for different positions of dopants in TiO_2 lattice. The position of dopants is determined by the size differences between the host Ti^{4+} ionic radius and the dopants ionic radii. It is noted that the radii of V^{4+} is 59×10^{-12} which is incomparable to that of that of Ti^{4+} (68×10^{-12}). Large disturbance of the potential energy resulted in the creation of localized positive charge around Ti and/or formation an oxygen vacancy, which consequently enhanced the electron trapping efficiency. Substitutionally incorporated dopants are less useful for disturbing the dopant energy level, which in turn affects the electron trapping efficiency (Wang *et al.*, 1999).

As a conclusion for all works in this part, pulse anodization method was successfully developed to synthesize the metal-modified TiO_2 nanotube. Importantly, Li-modified electrodes in photoelectrochemical response were significantly enhanced corresponding to the photospectra extend to visible region (in comparison, the $IPCE_{max}$ of pure TiO_2 at 325 nm was 35 % with $IPCE_{max}$ of doped metal TiO_2, for example, Li^+ doped TiO_2, at 345 nm was 90%). The co-doping effects by metal cations with high oxidation numbers on photoelectrochemistry properties were also observed on photocatalysis reduction. Thus, it was found that transition metal doping into photocatalyst with wide band gaps was effective for the development of photoelectrochemical response and photocatalytic activity if a suitable combination of dopant–co dopant was chosen.

4.4 Dye sensitized TiO_2 nanotube arrays for DSSC applications

Highly-ordered vertically oriented TiO_2 nanotube arrays fabricated by anodization constitute a material architecture that offers a large internal surface area without a concomitant decrease in geometric and structural order. The precisely oriented nature of the crystalline nanotube arrays makes them excellent electron percolation pathways for vectorial charge between interfaces (Frank *et al.*, 2004; Mor *et al.*, 2006). For applications where the use of vertically oriented titania nanotube arrays have been studied, these advantages have manifested themselves in an extraordinary enhancement of the extant TiO_2 properties. For example, in hydrogen sensors, the TiO_2 nanotube arrays possess such excellent photocatalytic properties that are able to self-clean from contamination with exposure to ambient UV light (Mor *et al.*, 2003b), and been successfully used as photoanodes in dye-sensitized solar cell (DSSCs) (Mor *et al.*, 2006; Macak *et al.*, 2005c).

Dye-sensitized solar cells (DSCs) are a relatively low cost solar cell technology that has achieved overall light-to-electricity conversion efficiencies of over 10.6% (Grätzel, 2004).The electron-collecting layer in a DSSC is typically a 10-*ím*-thick nanoparticulate film, with a three dimensional network of interconnected 15-20-nm-sized nanoparticles (Zhu *et al.*, 2007). The large surface area of the nanoporous film enables efficient light harvesting, maximizing the amount of photogenerated charge. Electron transport is a limiting factor in the performance of these nanoporous nanocrystalline electrodes, hindering progress in achieving higher efficiencies. The structural disorder at the contact between two crystalline nanoparticles leads to the enhanced scattering of free electrons, thus reducing electron mobility. An ordered and strongly interconnected nanoscale photoanode architecture offers the potential for improved electron transport leading to higher photoefficiencies. Several nanotubular architectures have been investigated for potential enhancement of electron percolation pathways and light conversion as well as improved ion diffusion at the semiconductor-electrolyte interface.

This part describes the application of highly-ordered TiO_2 nanotube arrays fabricated by anodization of Ti foil approximately 500 nm thick as the working electrode in liquid junction DSSCs. A detailed methodology of fabricating nanotube arrays has been explained in section 4.1.

4.4.1 Raman spectroscopy of zinc porphyrin

Raman spectroscopy was used to identity specific vibration mode that might indicate the surface interactions between Zn(II)-5,10,15,20-Tetra (4-carboxyphenyl) porphyrin (acid1), Zn(II)-5-(3,5-bicarboxyphenyl)-10,15,20-trimesitylporphyrin (acid 3) and Zn(II)-5,10,15,20-Tetra(3-carboxyphenyl)porphyrin (acid 4) on TiO_2. The samples that were studies included solution of zinc porphyrin and zinc porphyrin /TiO_2 electrodes prepared by adsorption from methanol solution using excitation wavelength at 473 nm. The Raman bands in the 600-1700 cm^{-1} region of Fig. 4.18 and 4.19 have been assigned to fundamental vibrations. The peak position of the Raman lines and their assignments are listed in Table 4.6.

Table 4.6 Wavenumbers (cm^{-1}) of the Raman spectrum of zinc porphyrin and proposed assignments

Acid 1		Acid 3		Acid 4		Assignment
solution	bound	solution	bound	solution	bound	
665	661	663	666	665	667	$\delta(C_\alpha C_m C_\alpha)+\nu(Ph)$
840	832		826	836	831	Phenyl
998	1008	1001	1001	1011	1011	ν(Ph breath)
		1016		1021		$\delta(C_\beta H)(B_{2g})$
1080	1076	1069	1068	1073	1078	$\delta(C_\beta H)$
1136			1156			$\delta(C_\beta H)$
1176	1184			1173		$\delta(C_\beta H)$
1238	1237	1229	1229	1238	1235	$\nu_1(\nu(C_m C_{ph})$
1290	1288	1300	1298	1303	1303	C-O
	1340					$\nu(C_\alpha C_\beta)+\delta(C_\beta H)$
1350	1351	1353	1352	1352	1352	$\nu C_\alpha C_\beta)+\nu(NC_\alpha)$
1419	1418	1417		1421		$\delta(CH_2)$
1451	1444			1456	1455	$\nu(C_\alpha C_\beta)+\delta(C_\beta H)$
1490	1506	1490	1489	1494	1493	$\nu(C_\alpha C_m)$, $\nu(C_\beta C_\beta)$
1546	1545	1546	1545	1547	1547	$\nu C_\alpha C_m)+\nu(C_\beta C_\beta)$
1603	1606	1589		1598	1597	Phenyl

The Raman spectra of acid 1, acid 3 and acid 4 in methanol solution with excitation at 473 nm are depicted in Fig. 4.18 the main Raman band are found between 1000 and 1600 cm^{-1} region associated with C-C and C-N stretching and C-H deformation mode. The three major Raman spectra band such as the mode $\nu(C_\alpha C_m)+\nu(C_\beta C_\beta)$ at 1546 cm^{-1}, mode $\nu C_\alpha C_\beta$), $\nu(NC_\alpha)$ at 1350 cm^{-1}, and mode (Pyrrole breath) at 1000 cm^{-1} were observed in the high-frequency region. The Raman mode assignment of the zinc porphyrin was made on the many literature and summarized in Table 4.6.

It is noteworthy that the Raman mode related to meso-phenyl groups in zinc porphyrin (Fig. 4.18), such as the ν(phenyl) mode at 1603 cm^{-1}(acid 1), at1589 cm^{-1}(acid 3) and at 1598 cm^{-1}(acid 4) and ν C_mC_{phenyl} mode appear at1238 cm^{-1}(acid 1), at 1229 cm^{-1}(acid 3) and at 1238 cm^{-1}(acid 4). Interestingly the enhancement of ν(phenyl) and ν C_mC_{phenyl} in acid 1 much difference in spectra of acid 3 and 4 which related to the rotation of the phenyl ring from vertical conformation to the porphyrin ring plane. This feature become evident enhancement of ν(phenyl) and ν C_mC_{phenyl} in acid 1, indicating phenyl ring in acid 1 easy to vibration and rotation because the position of the COOH groups introduced at *para* position with phenyl groups. Whereas acid 4 the position of the COOH groups introduced at *meta* position with phenyl and acid 3 which have three methyl groups are introduced at 2,4,6-positions of the other three meso-phenyl groups. In addition the $\nu(C_\alpha\text{-}C_\beta)$ +$\delta(C_\beta\text{- H})$ band (1455.8 cm^{-1}) was observed in acid 4 but too weak in the other two spectrums, indicating that the $\nu(C_\alpha\text{-}C_\beta)$ may be raised by coupling with $\delta(C_\beta\text{- H})$. The coupling pattern would be reversed in β-pyrrole substituted porphyrin, for which the carbon substituents are on C_β and hydrogen atom are attached to C_m.

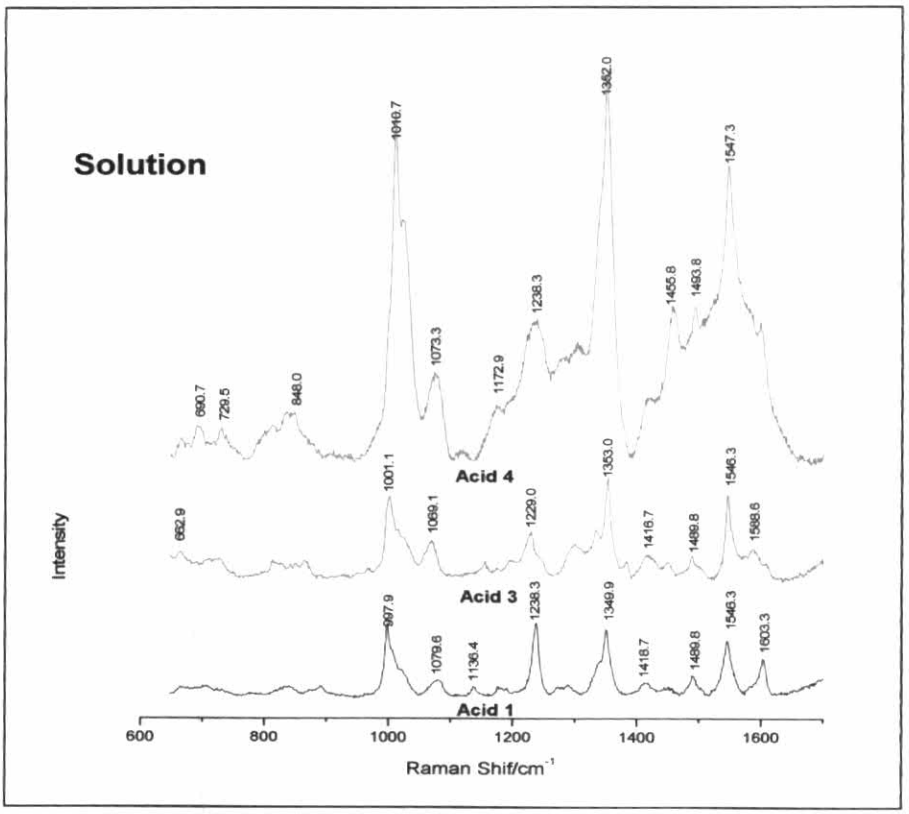

Figure 4.18 Raman spectra of Zinc Porphyrin in methanol solution.

However, when the dye is adsorbed on the TiO_2 nanotubes as substrate, weak line can be observed and also appear new line (see Fig. 4.19)

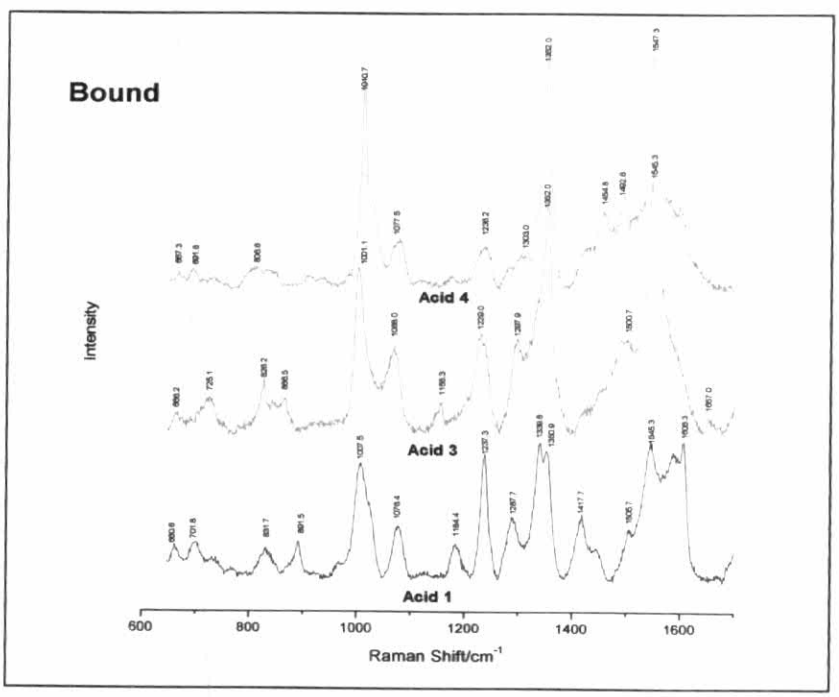

Figure 4.19 Raman spectra of Zinc Porphyrin /TiO_2 electrodes.

Fig. 4.19 shows the raman spectra of acid 1 (*p*-ZnTCPP), acid 4 (*m*-ZnTCPP) and acid 3 on TiO_2. Although the solution spectra of zinc porphyrin gave slightly different features, but for adsorption spectra were completely different. In stance, the shift position of C-O stretching mode in the 1287-1303 cm^{-1}. In case of a comparison of acid 1 with acid 4 the C-O mode at 1288 cm^{-1} shift to 1303 cm^{-1}(shift band up by 15 cm^{-1}) are strongly affected by adsorption, relatively that the coordination of the carboxyl ligands to the TiO_2 surface.

Moreover the enchantment and shift on acid 1 at 1237 cm^{-1} (shift peak up by 8 cm^{-1} when compare with acid 3) and the appear peak at 1493 cm^{-1} in acid 4 but in other two spectra very weak these modes involve the movement of meso-carbon (i.e. $\nu(C_m\text{-}C_{phenyl})$ and $\nu(C_\alpha\text{-}C_m)$ respectively). In addition the shift in this peak position for the different molecules may be the result of strict hindrance of the molecules due to different interaction with TiO_2 nanotubes surface. Therefore, the appearance different position of phenyl mode in each spectrum (acid 1 have peak splitting at 1587 $cm^{-1}$and 1606 cm^{-1}, acid 4 at 1597 cm^{-1}) suggests that the influence of binding on the TiO_2 nanotubes surface trough its carboxylic groups due to the position on the carboxylic acid anchoring groups on the meso-phenyl ring does have a great influence on the binding mode. For acid 1 have the carboxylic acid anchoring groups on the 4-meso-phenyl ring (*para*) but for acid 4 at 3-meso-phenly ring (*meta*), Campbell *et.al.*(2004) have reported demonstrates that *mata*-TCCP could lie flat on the surface with all four acid groups available foe binding, while *para*-TCCP will edgewise to the surface and edgewise would allow a significantly higher dye concentration on the highly uneven, porous TiO_2 surface than flat binding.

The spectrum presented dye adsorbed on TiO_2 nanotubes in Fig. 4.19 showed some distinctively difference features from on the solution. In particular, the δ(CH) mode at 1184 cm^{-1},$\nu(C_\alpha C_\beta)+\delta$(CH) also observed at 1340 cm^{-1} and 1587 cm^{-1} phenyl mode were appeared only in the p-ZnTCPP/TiO_2 complex. Relatively large shifts are also observed for the pyrrole breath modes at 998 and C-H at 1080 cm^{-1} in comparison to the spectrum on solution. The splitting of the $\nu(C_\alpha C_\beta)+\nu(C_\alpha N)$ at 1351 cm^{-1} to 1340 cm^{-1} and the phenyl mode at 1606 cm^{-1} to 1587 cm^{-1}, indicating that this mode is strongly affected by binding to the surface of TiO_2 nanotube and when a molecule is bound to the TiO_2 surface, the movements of its vibrations are more restricted compared to a fee molecule in the solution or gas phase.

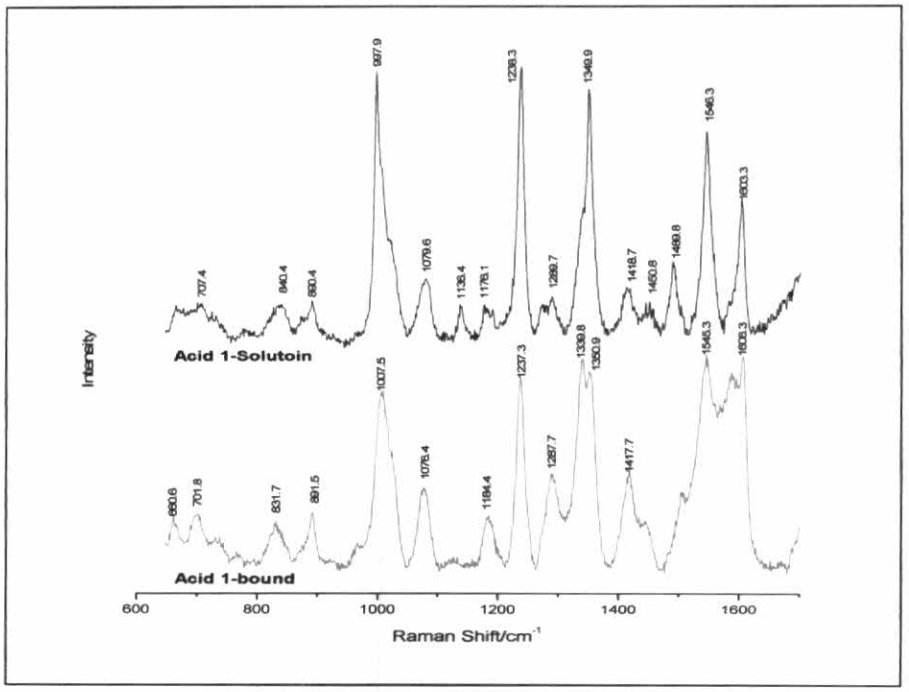

Figure 4.20 Raman spectra of p-ZnTCPP (acid 1).

The ligand of the zinc porphyrin (p-ZnTCPP) has four carboxylic acid groups, which from bonds to the surface groups on TiO_2 nanotubes (Fig. 4.20). Each carboxylic acid group could potentially from as ester bond with the surface TiOH group leading to a unidentate linkage. Each could also chelate with a single Ti^{4+} ion or two Ti^{4+} ions leading to a bidentate or a bridging bond, respectively, Recently, Nazeeruddin et.al. (2003) used the splitting of asymmetric and symmetric carboxylate stretching bands in the ATR-FTIR spectra to distinguish the possible mode of coordination of porphyrin to the surface of TiO_2 nanoparticles. Based on the splitting observed in the ATR-FTIR bands of carboxylate asymmetric (1598 cm^{-1}) and symmetric (1391 cm^{-1}), they suggests that the carboxylate are bound to the TiO_2 surface via a bridging bidentate or chelating mode.

4.4.2 Model for Zinc porphyrin binding to TiO_2 nanotubes

The binding of porphyrin to a TiO_2 film has been studied by other groups. The three possible coordination modes of the carboxylates were discussed in their studies. That coordination is unidentate (ester-like linkage), bidentate chelating or bridging and bridging bidentate. How carboxylates binding on TiO_2 surface is focused in this work. Since there are four carboxylate groups present in one porphyrin molecule, up to four attachments are in principle possible. The porphyrins could lie flat on or edgewise to the semiconductor surface. Edgewise binding would allow a significantly higher dye concentration on the highly uneven, porous TiO_2 surface than flat binding. It is likely that acid 3 binds predominantly edgewise (Fig. 4.21), given the single binding functionality. In contrast, it might be anticipated that a larger number of carboxylic functionalities might force the porphyrin to lie flat on the surface. The tetra-*meso*-acid porphyrins, acid 4 the *meta*-substituted monoporphyrin gave significantly higher *IPCE* results, with an IPCE value four-fold higher than the *para*-acid derivative (acid 1), Simple modelling of the tetra acids (Fig. 4.21) clearly demonstrates that while acid 4 could lie flat on the surface with all four acid groups available for binding, this would not be the case for acid 1.

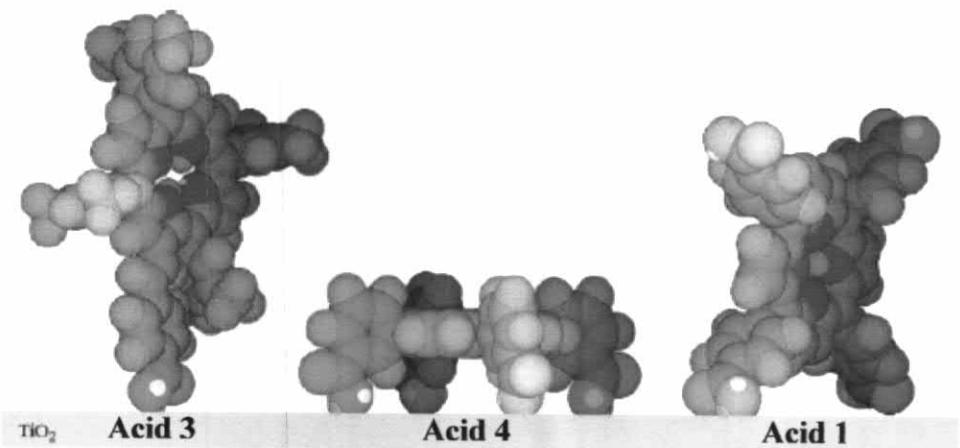

Figure 4.21 Possible binding models for carboxylic acid groups on TiO_2 surface

Indeed, Watson et al. (2004) have concluded that TCPP (acid 1) itself likely binds to TiO_2 in "a variety of different adsorption modes including multilayers" rather than a fully flat geometry (Diskin-Posner *et al.*, 1999). Therefore, the predominant factor for the improved efficiency of acid 3 over acid 1 could be the improved charge transfer through the fully conjugated system, along with higher surface area coverage

by this possibly edgewise-bound porphyrin. The nearly orthogonal electronically decoupled *meso*-benzoic acids may limit charge injection from acid 1. In contrast, if the *meta*-T_3CPP (acid 4) can adopt a fully flat binding mode, this might allow more efficient direct charge injection from the porphyrin to the semiconductor surface, accounting for the higher performance of this tetra acid. It was also noted that generally the low *IPCE* values of all the multiacid porphyrins were accompanied by the observation of faint dye colourations and shadowing on the TiO_2 surface after removal from the dye solution, indicating poor binding or low surface coverage. The weak binding of these acids is surprising considering the number of carboxylic acid groups present on these molecules. However, given the potentially flatter binding modality of the multiacid porphyrins, lower surface coverage is to be expected and the rough, nanocrystalline TiO_2 may not be the optimal surface for flat binding. In addition, Boschloo and Goossens (1996) have shown that the position of substitution (*meta*, *para*) of the binding functionality has a significant influence on the sensitisation efficiency of porphyrins. It is apparent that this is indeed the case here, with the porphyrins containing *meta* binding functionality showing superior cell performance to those with *para* binding functionality. This may again be a result of the surface binding modality.

4.4.3 Photoelectrochemical properties of the TiO_2 nanotube sensitized by zinc porphyrin

4.4.3.1 Relationship between the photocurrent efficiency and TiO_2 nanotube morphology. These prior studies were performed with the aim of optimizing the design and binding mode of the chromophores adsorbed on nanoparticulate TiO_2 films. With the same goal of optimizing DSSC efficiency, we propose to use our oxide nanotube arrays (prepared with different nanotube diameter and wall thickness, see sections 4.1 and 4.2) and newly designed porphyrin chromophores prepared by Prof. Elena Galoppini at Rutgers University. As porphyrin dyes have Q absorption bands responsible for their purple color (λ_{max} of 500-650 nm), the enhance the photocurrent efficiency in this spectral range by controlling the directionality of electron injection from the photoexcited dye to the semiconductor. This in turn promotes electron transport through the self-ordered arrays of TiO_2 nanotubes thus minimizing electron-hole recombination (Fig. 2.3). The chemical structures of these

porphyrins are presented in Fig. 4.22. Observe that two of them have four anchoring groups and one has only two.

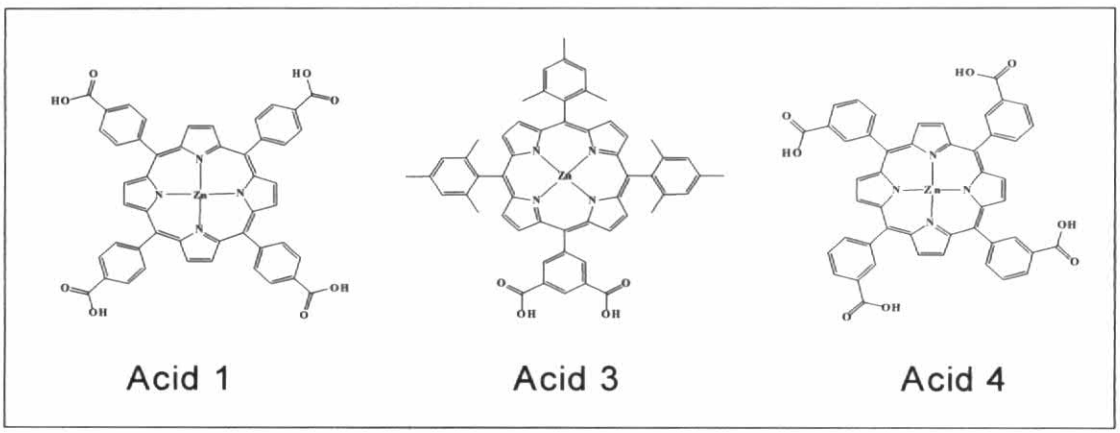

Figure 4.22 Structures of the porphyrins for sensitization of TiO_2 nanotube arrays.

For measuring the IPCE value, we have built a prototype DSSC (area ~0.7 cm^2). Typically, the cell consists of porphyrin sensitized TiO_2 nanotube arrays as working electrode, a TCO glass with 15 Å of e-beam evaporated transparent Pt as counterelectrode, and a sealing separator (60 μm) for providing the electrolyte chamber which is filled with I^-/I_3^- electrolyte + *tert*-butyl pyridine in acetonitrile. The cell is illuminated from the top through the counterelectrode and the light intensity is measured monochromatically to normalize the photocurrent response of the DSSC device (see Fig. 3.4). Incident photon-to-electron conversion efficiency (IPCE) was used as a figure-of-merit after a selected porphyrin chromophore is attached to the oxide (initially, TiO_2) nanotube array. Different numbers and positions of carboxylic acid anchoring groups in the dye was tested for their influence on the binding mode (planar, vertical) and, consequently, on the efficiency of electron injection. The binding time for the porphyrin was adjusted for each type of TiO_2 nanotube array to balance a high degree of porphyrin adsorption without excessive aggregation/ stacking.

Fig. 4.23 shows photocurrent action spectra of the zinc porphyrin sensitized nanotubular surfaces with different adsorption time for TiO_2 nanotube prepared by anodization at 20 V for 3 h in 0.36 M NH_4F/EG in same dye concentration (0.5 mM). It can be seen that short time binding 30 min at 410 nm the $IPCE_{max}$ of 23 % is

achieved the highest value, but when increase binding time the $IPCE_{max}$ were decreased. So a short binding time was chosen to prevent aggregation of the porphyrins at the metal oxide surface.

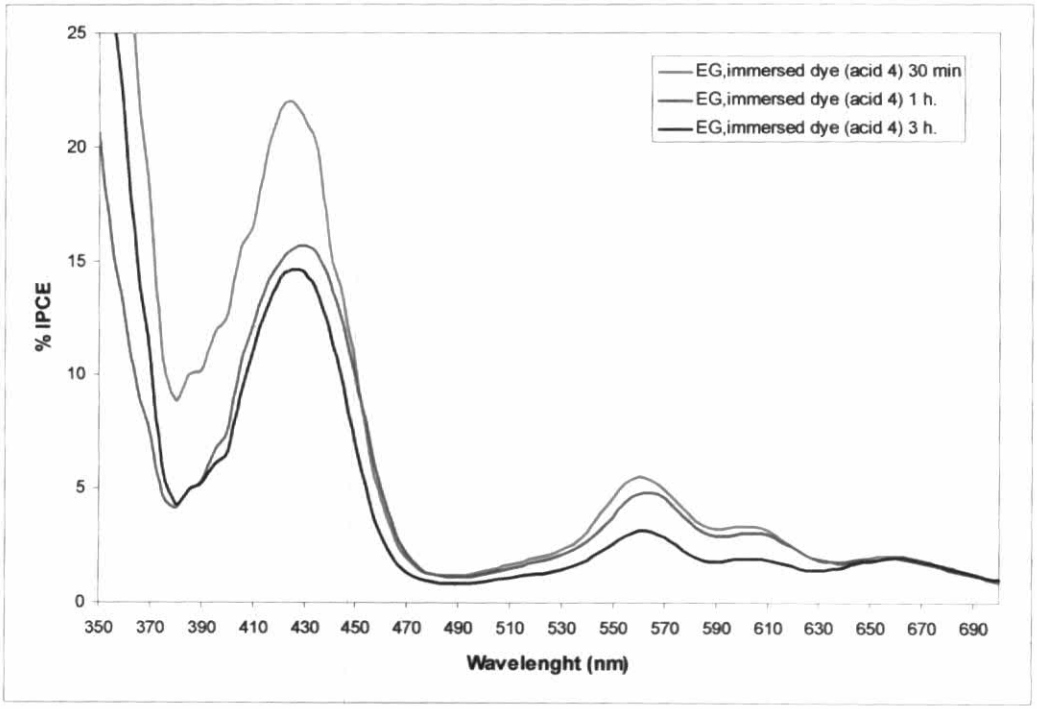

Figure 4.23 Photoaction spectra (IPCE VS wavelength) of nanoporous TiO_2 films prepared in different media modifiers as shown by anodization at 20 V for 3 h in 0.36 M NH_4F/EG. The stationary photocurrent density was measured monochromatically at 0.48 V for these TiO_2 films after sensitization for different time in 0.5 mM m-ZnTCPP dye (acid 4).

Preliminary IPCE vs. wavelength plots obtained for three newly synthesized porphyrins (with short names acid 1, acid 3, and acid 4) adsorbed on different TiO_2 nanotube arrays, are presented in Fig. 4.24. Each frame in Fig. 4.24 corresponds to a different TiO_2 nanotube array prepared (top to bottom) by anodization at 20 V (3 h) in 0.36 M NH_4F electrolyte with ethylene glycol (EG), glycerol, poly(ethylene glycol) (PEG 400), and without media modifier respectively. The corresponding SEM images are also inserted in the IPCE data. Some correlations between the TiO_2 nanotube morphology and the IPCE values for the three porphyrin sensitizers can be extracted from the data in Table 4.6 and Fig. 4.24.

Table 4.7 Photoelectrochemical Properties of three Porphyrin on TiO_2 nanotubes

Porphyrin	TiO_2/ media modifier (tube diameter)	IPCE(%) Soret 430 nm	Q(1,0) 560 nm[d]	Q(0,0) 600 nm[e]
Acid 1[a]	NH_4F *(porous)*	19.15	2.82 (0.15)	2.09 (0.11)
	EG *(55 nm)*	38.44	4.23 (0.11)	1.96 (0.05)
	Glycerol *(70 nm)*	24.90	2.96 (0.12)	1.92 (0.78)
	PEG 400 *(120 nm)*	34.13	4.88 (0.14)	3.18 (0.09)
Acid 3[b]	NH_4F	34.76	9.29 (0.27)	4.87 (0.14)
	EG	37.44	19.24 (0.51)	9.54 (0.25)
	Glycerol	35.24	14.21 (0.40)	7.46 (0.21)
	PEG 400	39.10	14.93 (0.38)	7.21 (0.18)
Acid 4[c]	NH_4F	43.16	20.41 (0.47)	11.27 (0.26)
	EG	51.75	24.64 (0.48)	13.12 (0.25)
	Glycerol	47.81	22.16 (0.46)	11.96 (0.25)
	PEG 400	47.88	26.23 (0.54)	13.52 (0.28)

[a] Acid 1 = Zn(II)-5,10,15,20-Tetra(4-carboxyphenyl)porphyrin (*p*-ZnTCPP)
[b] Acid 3 = Zn(II)-5-(3,5-bicarboxyphenyl)-10,15,20-trimesitylporphyrin
[c] Acid 4 = Zn(II)-5,10,15,20-Tetra(3-carboxyphenyl)porphyrin (*m*-ZnTCPP)
[d] In parentheses are the Q(1,0) vs Soret peak intensity ratios.
[e] In parentheses are the Q(0,0) vs Soret peak intensity ratios.

The IPCE for *m*-ZnTCPP (acid 4) at 430 nm of the entire TiO_2 electrode (The IPEC up to 48 % are reached), corresponding to the Soret absorption band, represented a 2-fold increase with respect to the pare-substituted analogue *p*-ZnTCPP (acid 1) at the corresponding wavelength. IPCE value at the lower energy Q band of *m*-ZnTCPP (acid 3 and acid 4) were in the range of 10-27%, which is a greater than 15-fold increase with respect to the IPCE values observed in the same region for *p*-ZnTCPP (Table 4.7). Interestingly, the IPCE value at the high energy band (Soret band) for the three acids on films prepared from EG (Fig. 4.24 a) is highest than the IPCE-wavelength profiles of the other TiO_2 nanotube architectures. The IPCE values at the Soret band for the three acids on TiO_2 nanotube arrays prepared from EG (tube diameter: ~55 nm), glycerol (tube diameter: ~70 nm), and PEG 400 (tube diameter: ~120 nm) are higher than TiO_2 nanoporous (Fig. 4.24 d).

For all porphyrins, the Soret band showed the highest IPCE value. This was expected as its extinction coefficient is 1 order of magnitude larger than for the Q bands. However, the larger increase in IPCE observed for the *meta*-substituted systems in the Q-band region, relative to the Soret absorption, suggests that the lower energy S_1 transition of the porphyrin chromophores has a greater quantum efficiency for change injection when oriented in a planar geometry with respect to the TiO_2 surface Q (1,0)/Soret peak intensity ratio (see Table 4.7). Comparing the ratio of the IPCE values at the Soret band with respect to the Q (1,0) band (peaking at 560 and 600 nm), it appears that acid 4 may be binding preferentially in a planar geometry to the TiO_2 nanotubes prepared from EG (Fig. 4.24a) vs. a vertical binding to the larger nanotubes prepared from PEG 400 (Fig. 4.24c). This is also corroborated by the lower Soret IPCE observed in Fig. 4.24a in comparison to that obtained on larger nanotubes (Fig. 4.24c). The higher IPCE values observed for acid 4 in the Q band region in comparison to those of acid 3 as well as its greater I_{sc} suggest a reduced charge recombination for this system, possibly because of the increased distance of the porphyrin ring from the TiO_2 surface and/or a better surface coverage blocking the electrons in the TiO_2 from reacting with the electrolyte. The lack of any aggregate absorption band in the photocurrent action spectrum of *p*-ZnTCPP suggests that aggregates do not contribute to any current generation. As the higher energy peak in the Soret band is due to formation of H-aggregates at the surface, its manifestation in the IPCE data indicates that H-aggregates are contributing efficiently (~51%) to charge injection into TiO_2 nanotubes prepared from EG. *A lower performance (~19%) was found for this acid when anchored on a TiO_2 nanoparticulate film.*

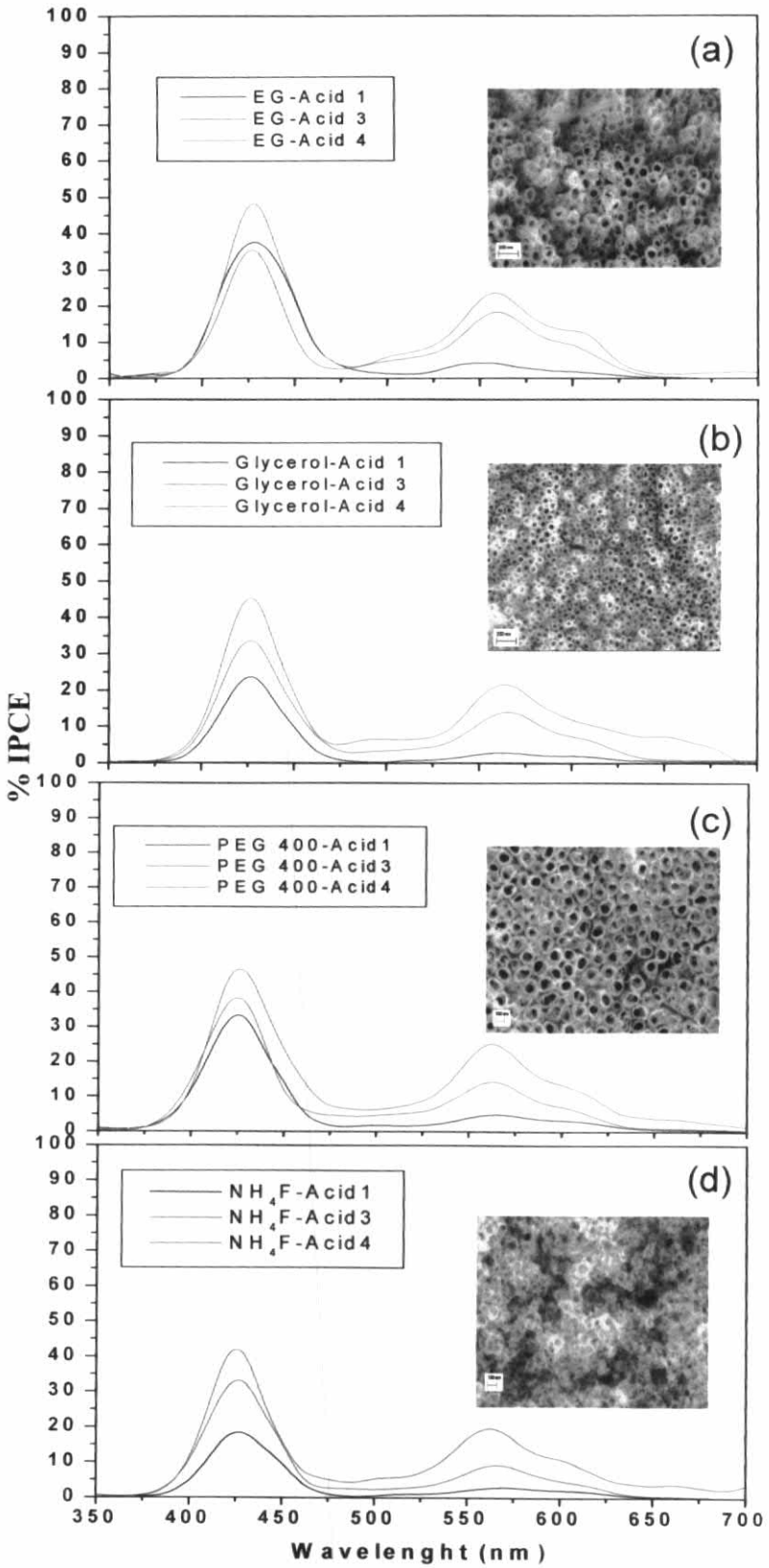

Figure 4.24 Photoaction spectra obtained using the prototype DSSC device at a 0.4 V bias between working and counter electrodes. The inserts show the corresponding TiO_2 morphology in each case.

The efficient directionality of electron transfer from the excited dye to the nanotubes is also supported by the negative effect of $TiCl_4$ treatment on our films. In fact, this known procedure consisting of impregnation with $TiCl_4$ followed by thermal anneal, has the purpose of enhancing the film surface area, thus improving the photoconversion performance in nanoparticulate TiO_2 films. On the contrary, this treatment is deleterious for our highly ordered nanotube arrays suggesting that a key parameter is the right positioning (and anchoring) of the dye on *smooth* TiO_2 nanotubes to afford a straight path for the injected electrons from the photoexcited dye (see Fig. 4.25).

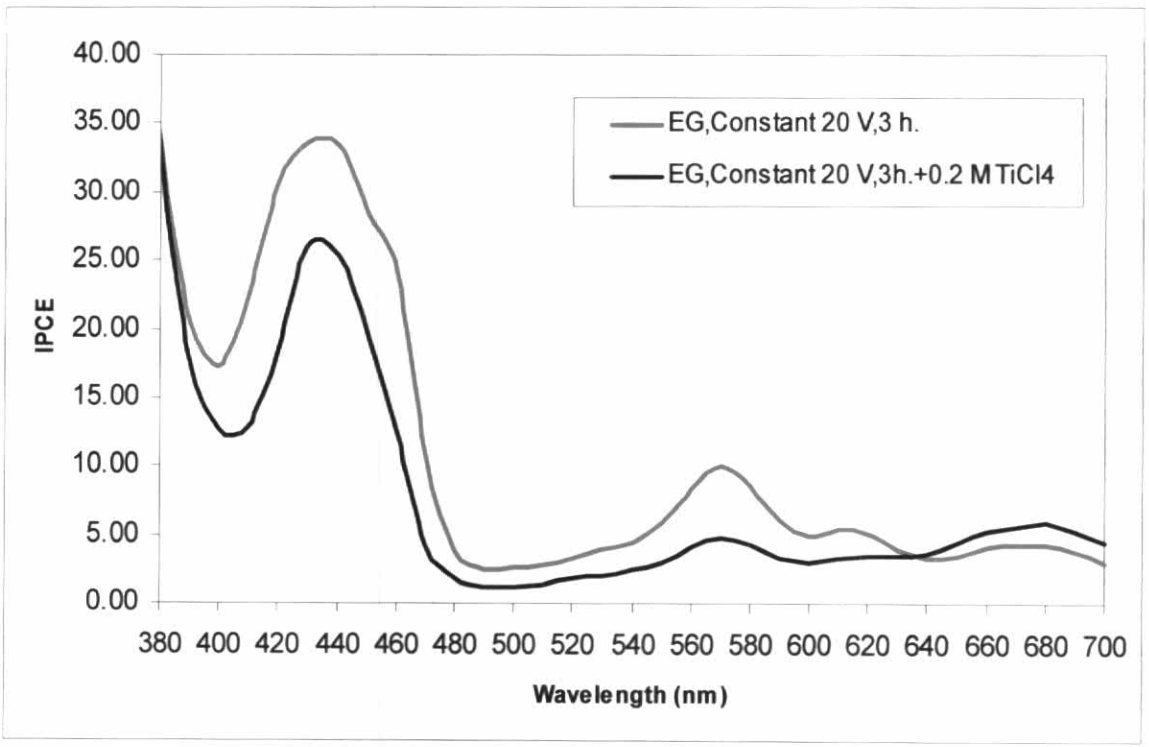

Figure 4.25 Photoaction spectra (IPCE VS wavelength) of nanoporous TiO_2 films prepared by anodization at 20 V for 3 h in 0.36 M NH_4F/EG. The stationary photocurrent density was measured monochromatically at 0.48 V for these TiO_2 films after sensitization for 30 min in 0.5 mM m-ZnTCPP dye (acid 4).

4.4.3.2 Relationship between the photocurrent efficiency and adsorption characteristic The main objective of the photochemical experiment and the adsorption spectra was to determine the effect of the binding geometrics of the sensitizer on the solar cell efficiencies. The photocurrent action spectra of all three zinc porphyrin bound to TiO_2 nanotube are shown in Table 4.8 and Fig. 4.26.

Porphyrin	TiO_2/ media modifier	UV-Vis absorption			
		Soret λ_{max}, (A)	Q(1,0) λ_{max}, (A)	Q(0,0) λ_{max}, (A)	Splitting λ_{max}, (A)
Acid 1[a]	NH_4F	427(0.43)	562(0.07)	603(0.04)	412(0.39)
	EG	425(0.91)	559(0.05)	603(0.01)	412(0.54)
	Glycerol	428(0.39)	560(0.03)	603(0.01)	412(0.23)
	PEG 400	429(0.64)	561(0.06)	608(0.02)	412(0.47)
Acid 3[b]	NH_4F	433(0.76)	558(0.08)	596(0.04)	
	EG	428(0.91)	557(0.21)	599(0.05)	
	Glycerol	428(0.64)	555(0.13)	596(0.04)	
	PEG 400	428(1.00)	557(0.15)	600(0.04)	
Acid 4[c]	NH_4F	432(0.75)	560(0.06)	601(0.02)	
	EG	428(1.18)	558(0.21)	599(0.06)	
	Glycerol	429(0.74)	559(0.09)	598(0.02)	
	PEG 400	428(1.04)	559(0.13)	599(0.02)	

Table 4.8 UV-Vis Absorption data of three Porphyrin on TiO_2 nanotubes

[a] Acid 1 = Zn(II)-5,10,15,20-Tetra(4-carboxyphenyl)porphyrin (*p*-ZnTCPP)
[b] Acid 3 = Zn(II)-5-(3,5-bicarboxyphenyl)-10,15,20-trimesitylporphyrin
[c] Acid 4 = Zn(II)-5,10,15,20-Tetra(3-carboxyphenyl)porphyrin (*m*-ZnTCPP)

The absorption of the TiO_2 electrode modified with acid 4 is narrow than that of TiO_2 electrode modified with acid 1 and acid 3 dye molecules, and can match the solar spectrum. Even more interesting is that acid 1 on the TiO_2 nanotubes prepared from NH_4F (nanoporous) (Fig. 4.26 d) shows a significant split (Soret band) in the absorption spectra, whereas on the TiO_2 nanotubes prepared from EG, glycerol, and PEG 400 (nanotube), no splitting is evident (Fig. 4.26 a-c). Interestingly, the absorption spectra at the high energy band (Soret band) for the acids 3 on films prepared from EG (Fig. 4.26 a) is split in contrast with the absorption spectra profiles of the other TiO_2 nanotube architectures.

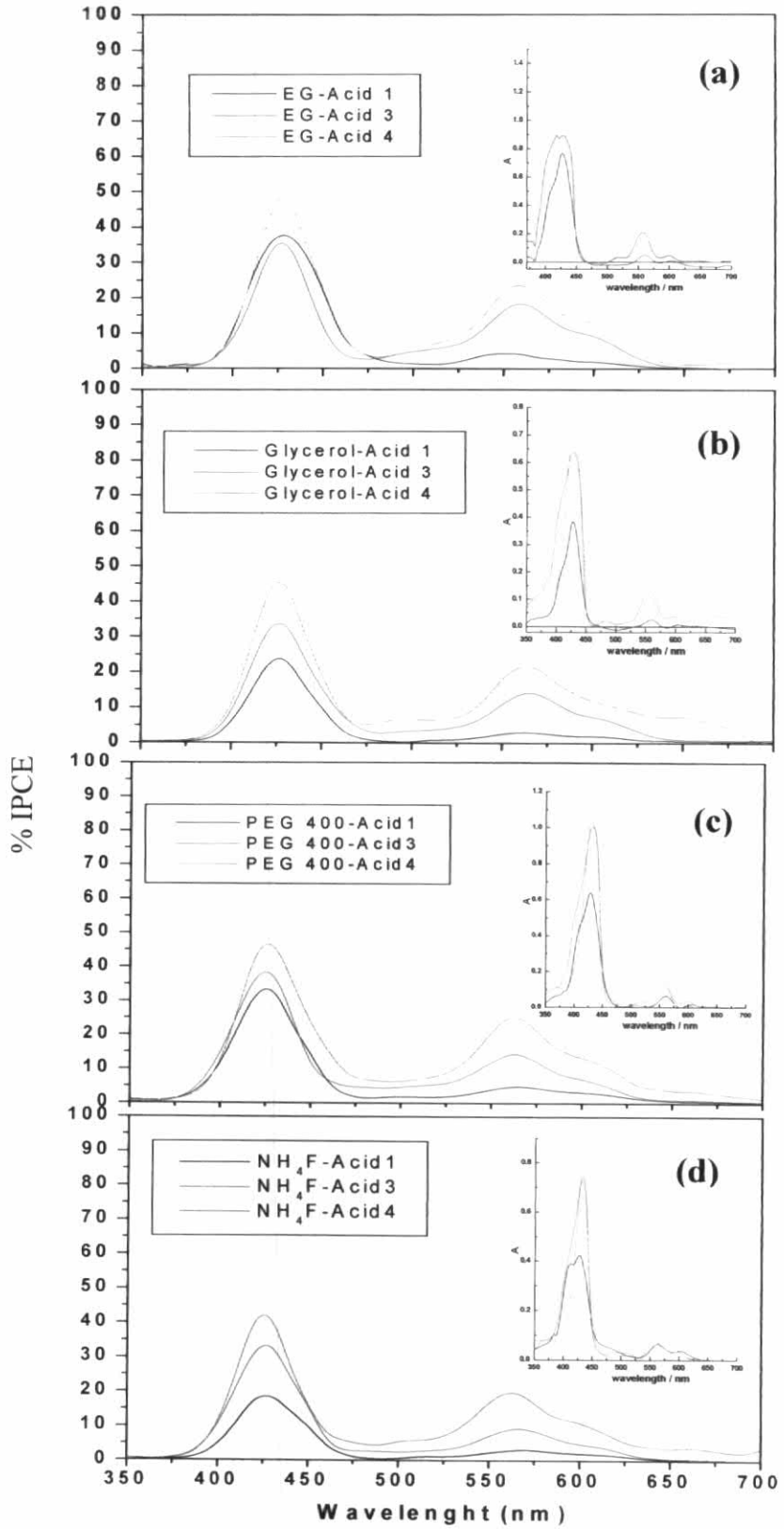

Figure 4.26 Photoaction spectra obtained using the prototype DSSC device at a 0.4 V bias between working and counter electrodes. The inserts show the absorption spectra in each case.

The photocurrent action spectrum of the TiO_2 electrode correlates well with its absorption spectrum, indicating the acid 3 and acid 4 have a significant contribution to the photocurrent of the electrode. The incident photon- to-current-conversion, an IPCE up to 52 % is reached. The high yield in the IPCE of the zinc porphyrin cell based on the TiO_2 nanotube electrode can be explained as follows: The dye is absorbed on the surface of the TiO_2 electrode, due to the large surface area factor of the nanotube electrode, only the first monolayer of adsorbed dye is sufficient to absorb the incident light nearly completely, the photogenerated carries resulted from absorption of incident photons by dye molecules can be easily transported into the conduction band of the TiO_2, improving the charge separation efficiency.

In summary, the self-organized TiO_2 nanotubes can be sensitized with a suitable charge transfer dye to significantly increase the quantitative conversion efficiency of visible light photons into electric current. Photoelectrochemical investigations were carried out with anodic TiO_2 nanotube grown in 0.36 M NH_4F/ethlylene glycol with a diameter of 60 nm and length of 800 nm. Clearly sub-band gap sensitization with Zn(II)-5,10,15,20-Tetra(3-carboxyphenyl)porphyrin (acid 4) was successful and led to considerable conversion efficiencies (IPCE up to 52%). The main factors that affect the IPCE in the visible range are the structure of the tube (anatase better than amorphous), the dye concentration and the tube length. Both an increase in dye concentration and tube length lead to an increase in IPCE. This can be ascribed to a higher packing density of the dye on TiO_2 surface with a higher concentration and a higher light absorption length. However, considering both factors, it turns out that for the longer tubes a significantly lower dye concentration is needed to achieve maximum IPCE values. A potential advantage of the nanotubes over conventional e.g. sol– gel produced TiO_2 electrodes is that their highly ordered morphology provides a high degree of control for device implementation. The application of this material geometry to dye cells requires backside illumination, a less than optimal approach for light-to-electrical energy conversion because the platinised counter electrode partially reflects light, while iodine in the electrolyte absorbs photons in the near UV region.

However dye sensitized film cannot use in photoreduction of chromium (VI) applications due to adsorb dye molecules on the semiconductor surface. Which upon light absorption will inject electrons into conduction band of TiO_2 nanotube from the excited state of the dye molecule into the semiconductor, the photooxidized dye can occur because the dye cannot regenerated by electron donation from the electrolyte, usually an organic solvent containing a electrolyte system, such as the iodide/triiodide couple. The regeneration of the sensitizer by iodide intercepts the recapture of the conduction band electron by the oxidized dye. Additionally, porphyrin dye dissolved in water, thus dye sensitized film not response with visible light.

4.5 Photocatalytic reaction of TiO_2 nanotube

4.5.1 Photocatalytic properties of TiO_2 nanostructures using different electrolyte composition prepared by anodization technique

4.5.1.1 Effect of electrolyte composition on morphology of TiO_2 nanostructures. Anodic growth of oxide layers on Ti substrates relies on the controlled balance between oxide formation and chemical/electrochemical dissolution phenomena. The ability to fabricate nanotube arrays of different shape (cylindrical, tapered), pore size, length, and wall thickness by varying anodization parameters including electrolyte concentration, media modifier, pH, voltage, and bath temperature. For what concerns the electrolyte composition, an important requirement is that it should not be aggressive towards the growing oxide, to avoid its dissolution during the process, or at least it should be ensured that the oxide growth rate is higher than the dissolution one (Cai *et al.* 2005). Thus a wide range of fluoride-based electrolytes have been deployed in previous studies, including HF, KF or NaF, and HNO_3-HF or H_2SO_4-HF mixtures. Other electrolyte compositions include $NH_4F/(NH_4)_2SO_4$ or NaF/Na_2SO_4 mixtures and various acids such as boric acid, citric acid, or acetic acid (Mor *et al*, 2006).

In this study, the TiO_2 samples were prepared by constant anodization at 20 V (Fig. 3.1 a) with those grown via 20 V/-4 V pulses (Fig. 3.1 b). In all cases, aqueous NH_4F electrolytes (0.36 M concentration) were used for 3 h growth times in different media modifier (entries 1-11, Table 4.9). The morphology were not different in both case (constant, pulse) when using EG, Glycerol:H_2O (90:10), PEG 400:H_2O (80:20), 1 M Na_2SO_4, 1 M $(NH_4)_2HPO_4$ and 1 M CH_3COONH_4. The effect of pulse anodization were extremely shown when using 1M D-mannitol, 1 M $(NH_4)_2SO_4$, 1 M H_3PO_4, 1 M CH_3COOH and without media modifier. It is observed that using different anodization conditions (constant or pulse) and different media modifiers provide different structures of nanostructures. Various formations of TiO_2 nanotube can be seen in the presence of organic media modifier such as glycerol, EG, and PEG 400. The TiO_2 nanotubes and non-organized form are obtained when using inorganic salt as media modifier. The non-organized form can be seen in the pulse anodization mode.

Table 4.9 Anodization conditions and morphology of TiO_2 nanostructures in this study

Medium modifiers	TiO_2-nanotube	TiO_2-nanoporous	TiO_2-nonorganized
A1: w/o medium modifier		*Pulse* [a)]	*Constant* [b)]
A2: EG:H_2O (90:10)	*Constant , Pulse*		
A3: Glycerol:H_2O (90:10)	*Constant , Pulse*		
A4: 1 M D-mannitol		*Constant*	*Pulse*
A5: PEG 400 :H_2O (90:20)	*Constant , Pulse*		
A6: 1 M Na_2SO_4		*Constant , Pulse*	
A7: 1 M $(NH_4)_2SO_4$	*Pulse*	*Constant*	
A8: 1 M H_3PO_4		*Constant*	*Pulse*
A9: 1 M $(NH_4)_2HPO_4$			*Constant , Pulse*
A10: 1 M CH_3COOH		*Constant*	*Pulse*
A11: 1 M CH_3COONH_4			*Constant , Pulse*

a) : TiO_2 film prepared by pulse anodization between 20 V/-4 V (30 s) for 3 h
b) : TiO_2 film prepared by constant anodization for 3 h

It is noted that the negative limit of the voltage pulse and the cathodic current flow regime of the pulse both exerted a crucial effect on the nanotube morphology. This occurrence can be explained by the fact that the formation of TiO_2 nanotube is mainly controlled by the following chemical and electrochemical reactions. In general, hydrogen formation is occurring at the TiO_2/electrolyte inteface because the semiconductor is under direct biased condition (i.e. under an applied potential more negative than its flat band potential). Besides, during the cathodic voltage portion of the cycle, chemical dissolution of the oxide in the fluoride electrolyte plays a key role in the anodic layer morphology. These account for the progression in layer morphology from a nanoporous structure to a discrete tubular appearance when the chemical etching is allowed to exert an effect in the pulse mode. However, growth and self-assembly of TiO_2 nanotube and the chemical/electrochemical dissolution must be carefully balanced; for example, facile a chemical etch which can destroy the nanotube array structure.

4.5.1.2 Effect of types of media modifier on photoelectrochemical performance. The photoelectrochemical responses of TiO_2 films prepared under constant (20 V) and pulse (20 V/-4 V) polarization are shown in Fig. 4.27. Bar graph was used to compare the incident monochromatic photon-to-current conversion efficiencies (IPCE) for nanostructures TiO_2 films. The maximum incident photon to electron conversion efficiency IPCE (λ_{max}) of TiO_2 is identified at 320 nm (de Tacconi *et al.*, 2006). The IPCE (λ) is defined by equation 3.1 section 3.4.4. Photoaction spectra for TiO_2 nanostructures film were obtained with 0.5 M Na_2SO_4 supporting electrolyte.

(a) Nanotube

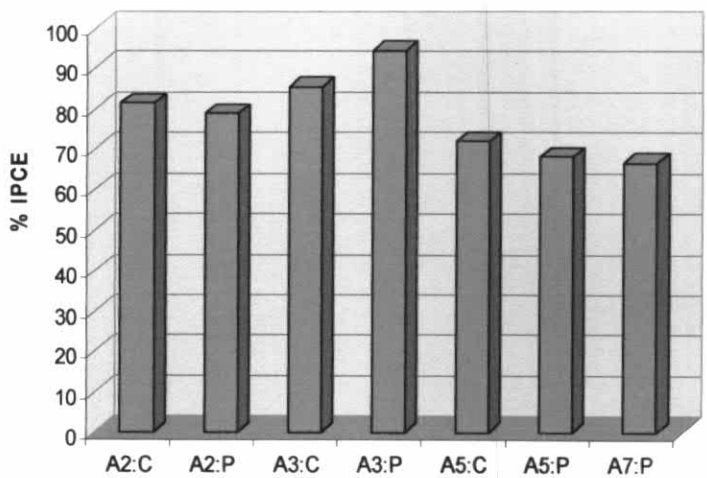

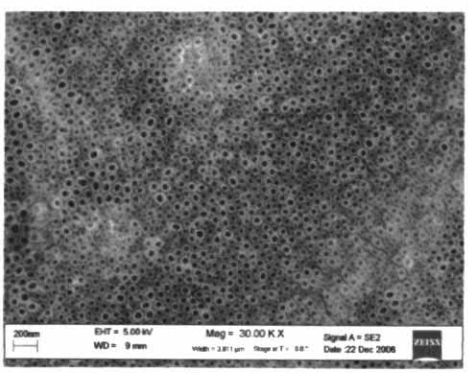

Nanotube TiO_2 (prepared by pulse anodization) in 0.36 M NH_4F/glycerol

(b) Nanoporous

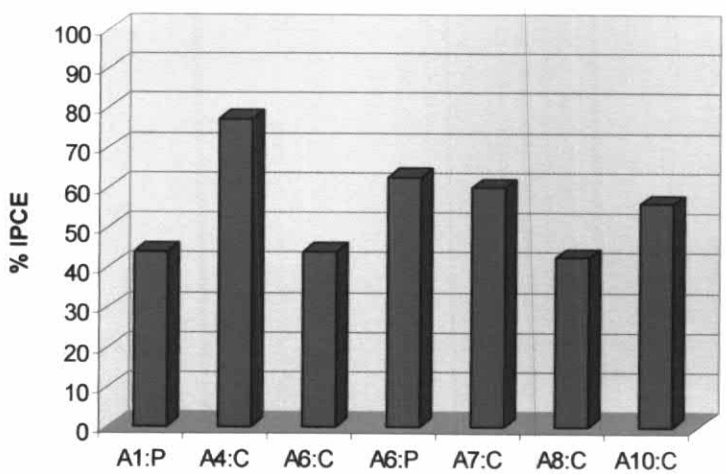

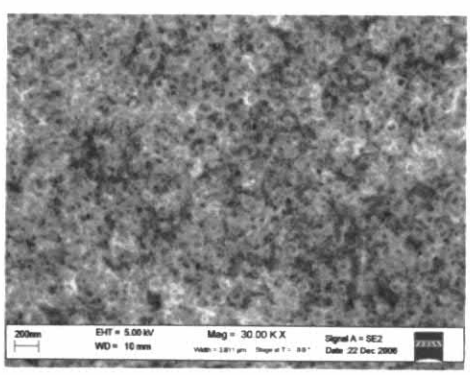

Nanoporous TiO_2 (prepared by pulse anodization) in 0.36 M NH_4F/1 M D-mannitol

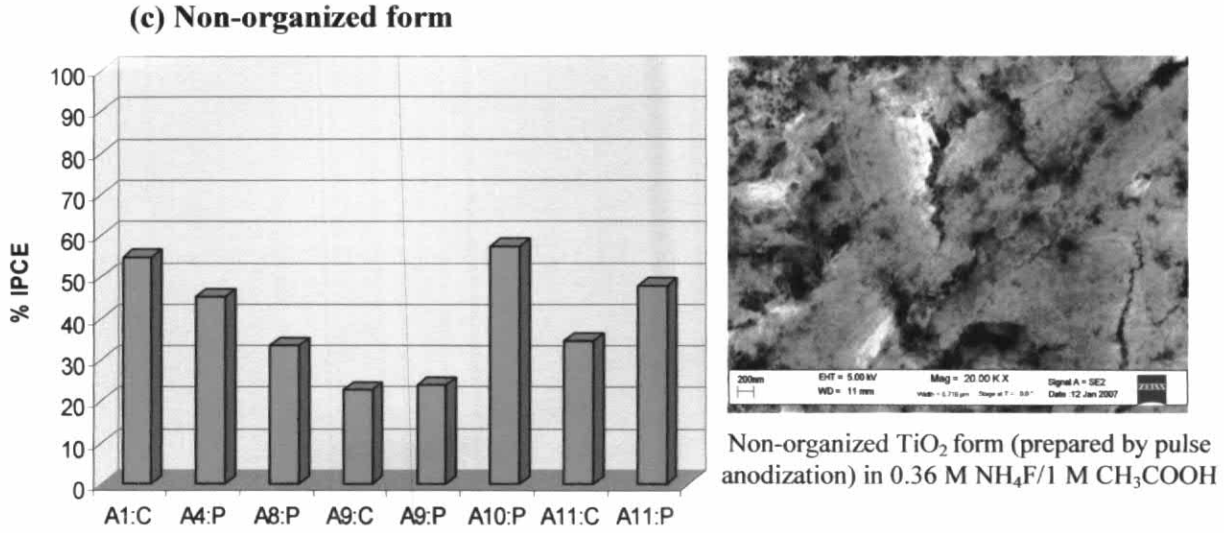

Figure 4.27 Bar diagram comprising of the incident photon-to-current conversion efficiencies (IPCE) at 320 nm for nanostructures TiO_2 films grown under different media modifier conditions. The inserts show the SEM picture in each case.

Fig. 4.27 shows the incident monochromatic photon-to-current conversion efficiencies (IPCE) for three different morphologies of TiO_2 nanostructure films. In comparison with the TiO_2 morphology, the TiO_2 nanotube array films (Fig. 4.27 a) show a significant increase the photoelectrochemical response than counterpart (nanoporous, non-organized in Fig 4.27 b-c, respectively), the IPCEs values can be divided into three ranges as 63-95%, 40-75 % and 20-55% corresponding nanotube, nanoporous and non-organized, respectively.

The result suggests that TiO_2 nanotube array film is able to harvest light more effectively than the nanoporous and non-organized structure under the same illumination. This strong enhancement of photoresponse could be ascribed to an increased light penetration depth and better scattering within a nanotube than a regular pore structure. In addition, the photogenerated charge carriers in the TiO_2 nanotube structure might be separated more efficient than TiO_2 nanoporous and non-organized films because of the short diffusion distance in the tube wall and the high contact area between the photocatalyst and electrolyte.

4.5.1.3 Effect of electrolyte composition on heterogeneous photocatalysis chromium removal by photocatalysis reduction

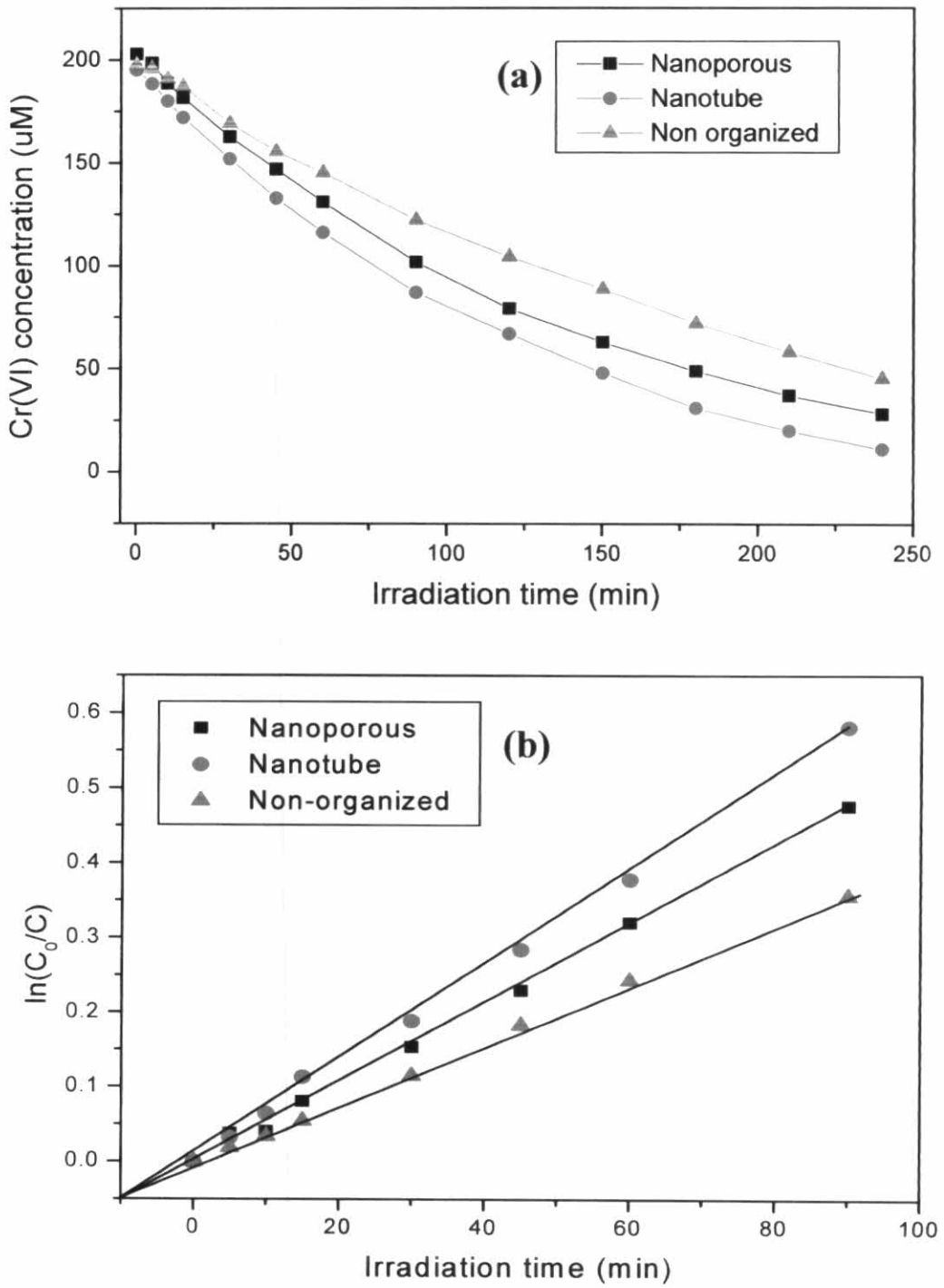

Figure 4.28 Kinetic plots of photoreduction of Cr(VI) in aqueous solution (200 μM) using TiO_2 nanostructure with different morphology

Fig. 4.28 a shows the plot of normalized concentration of Cr(VI) after dark adsorption 30 min versus illumination time. It is obvious that photoreduction of Cr(VI) obeys that pseudo first-order photoreduction reaction and its kinetics may be expressed as;

$$\ln(C_0/C) = kt \qquad \text{(Eq. 4.5)}$$

where k is the apparent rate constant, t is the irradiation time, and C_0, C are the initial and reaction concentrations of Cr (VI) aqueous solution, respectively. The apparent rate constant of the photoreduction of Cr (VI) represents a straight of line and the slope of linear regression with the different of TiO_2 nanostructure films shown in Fig. 4.28 b. When comparing the k_{obs} value of photoreduction activity of the TiO_2 nanostructure film (nanotube = 7.33×10^{-3}, nanoporous = 6.44×10^{-3} and non-organized = 4.03×10^{-3}), it is obvious that the well-ordered nanotube array film is more efficient than the random nanostructure film. This is ascribed to the more effective separation for the photogenerated electron-hole pairs and the higher internal surface area of the special nanotube array structure. Thus, the electron and the hole have high opportunities to participate in reduction reaction.

Following the above calculation, the kinetic values k_{obs}, $t_{1/2}$, and $r_{initial}$ of chromium (VI) photoreduction by TiO_2 photocatalyst prepared with different media modifiers are illustrated in Table 4.9. Obviously, the k_{obs} values are in the order nanotube > nanoporous > non-organized form; (9.1×10^{-3}-15.7×10^{-3}) > (7.27×10^{-3}–8.22×10^{-3}) > (5.44×10^{-3}-6.15×10^{-3}). It is noted that all kinetic values are direct proportion to the IPCE values. The kinetics behaviors of chromium (VI) photoreduction by the TiO_2 photocatalyst prepared with different media modifiers are listed Table 4.10a-c respectively.

Table 4.10 Kinetic parameters on photocatalytic reduction of Cr(VI) for selected TiO_2 nanonanostructure film

(a) Kinetic of photocatalysis Cr (VI) of TiO_2 nanotube

Code	Medium modifiers	k_{obs} (min^{-1})	$t_{1/2}$ (min)	$r_{initial}$ (μM/min)	Φ_{app} ($\times 10^{-4}$)
A2:P*	EG:H_2O (90:10)	10.70×10^{-3}	64.95	1.98	10.40
A3:C	Glycerol:H_2O (90:10)	8.81×10^{-3}	78.66	1.77	9.29
A3:P*	Glycerol:H_2O (90:10)	8.90×10^{-3}	73.88	1.70	8.90
A5:C	PEG 400:H_2O (90:20)	8.92×10^{-3}	77.69	1.74	9.12
A5:P*	PEG 400:H_2O (90:20)	16.30×10^{-3}	72.41	3.00	15.70

(b) Kinetic of photocatalysis Cr (VI) of TiO_2 nanoporous

Code	Medium modifiers	k_{obs} (min^{-1})	$t_{1/2}$ (min)	$r_{initial}$ (μM/min)	Φ_{app} ($\times 10^{-4}$)
A6:C	1 M Na_2SO_4	7.39×10^{-3}	93.77	1.57	8.22
A6:P	1 M Na_2SO_4	8.15×10^{-3}	85.03	1.54	8.08
A7:C	1 M $(NH_4)_2SO_4$	6.58×10^{-3}	105.32	1.39	7.27
A8:C	1 M H_3PO_4	7.60×10^{-3}	91.18	1.54	8.08
A10:C	1 M CH_3COOH	7.33×10^{-3}	94.54	1.54	8.10

(c) Kinetic of photocatalysis Cr (VI) of TiO_2 nonorganized form

Code	Medium modifiers	k_{obs} (min^{-1})	$t_{1/2}$ (min)	$r_{initial}$ (μM/min)	Φ_{app} ($\times 10^{-4}$)
A8:P	1 M H_3PO_4	5.13×10^{-3}	135.08	1.05	5.44
A9:C	1 M $(NH_4)_2HPO_4$	5.47×10^{-3}	126.69	1.08	5.66
A9:P	1 M $(NH_4)_2HPO_4$	5.11×10^{-3}	135.62	0.99	5.18
A10:P	1 M CH_3COOH	6.08×10^{-3}	113.98	1.17	6.15
A11:C	1 M CH_3COONH_4	5.23×10^{-3}	132.50	1.40	5.59
A11:P	1 M CH_3COONH_4	7.12×10^{-3}	97.33	1.06	7.35

* TiO_2 nanotube film prepared by pulse anodization (20/-4 V) using duration time 10 s, another films using duration time 30 s.

The result suggests that the incident monochromatic photon-to-current conversion efficiencies (IPCE) for the TiO_2 nanotube array films provide higher significant increase of photoelectrochemical response than counterpart (nanoporous, non-organized form), the IPCEs values obtained from TiO_2 nanotube can be produced more electron than those obtained from nanoporous and non-organized morphology under the same illumination respectively. This strong enhancement of photoresponse could be ascribed to an increasing of electron trapped surface more than a regular pore structure. In addition, the photogenerated charge carriers in the TiO_2 nanotube structure might be separated more efficiency than TiO_2 nanoporous and non-organized films because of the short diffusion distance in the tube wall and the high contact area between the photocatalyst and electrolyte. The responsive incident photon-to-current conversion efficiencies could reflect the overall photoelectron-conversion process. The high IPCE can be certainly attributed to high electron-injection yield, low electron-hole recombination and high photoelectron transfer efficiency for the nanotube array film, which could eventually benefit the corresponding photocatalytic reaction.

4.5.1.4 Quantum yield on photocatalytic reduction of Cr(VI) for TiO_2 nanonanostructure film. In photocatalysis, the addition of TiO_2 semiconductor by pulse anodization technique can alter the performance of photocatalysis process by changing the semiconductor surface properties. The enhancement in reactivity was observed from Fig. 4.29. which are bar graphs comparing quantum yield of Cr(VI) photoreduction reaction efficiency for films prepared with and without different modifiers by constant and pulse anodization. The efficiency of the photochemical reaction as quantum yield has been calculated for the Cr(VI) photoreduction reaction. The quantum yield is one of the most important parameter in evaluating the efficiency of a photochemistry, such as primary quantum yields (φ), product quantum yields (Φ), quantum yields of fluorescence, decomposition, etc. (Calvert and Pitt, 1966). In general, for direct photocatalysis processes in the environmental applications, it is not necessary to determine all the individual quantum yields corresponding to various pathways that the excited state can follow, but only the reaction quantum yield, which encompasses all reactions in a given set of conditions that lead to the decay of the parent pollutant, as a result of absorbed light in the system. The quantum yield for direct UV photolysis of pollutant, *P* is defined as (Equation 4.6) (Hatchard and Parker, 1956)

$$\Phi = \frac{\text{Number of molecules of } P \text{ disperse}}{\text{Number of photon of light absorbed}} \qquad \text{(Eq. 4.6)}$$

The results of chromium reduction quantum yield by the TiO_2 nanostructure electrode show in Fig. 4.29.

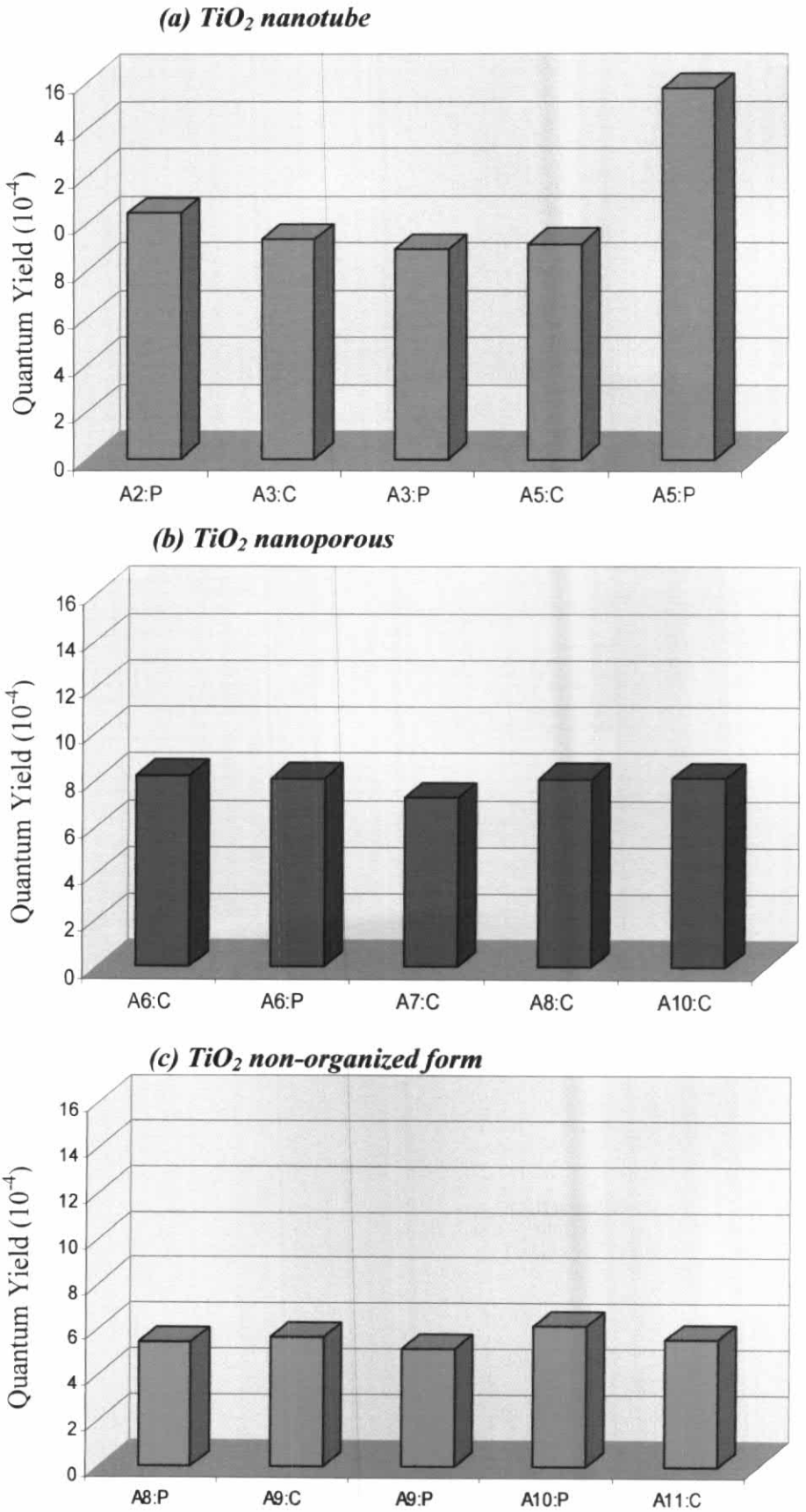

Figure 4.29 Bar diagram comprising of quantum yield for nanostructures TiO_2 films grown under different media modifier conditions.

Fig. 4.29 shows the quantum yield for three different morphologies of TiO_2 nanostructure film. In comparison with the TiO_2 morphology, the TiO_2 nanotube array films (Figs. 4.27 a) show a significant increase in photoelectrochemical response than counterpart (nanoporous, non-organized form in Figs 4.27 b-c respectively), the quantum yield values were devided into three ranges as 8.9×10^{-4}-15.7×10^{-4}, 7.27×10^{-4}–8.22×10^{-4} and 5.44×10^{-4}-6.15×10^{-4}corresponding to nanotube, nanoporous and non-organized structure, respectively. Information from this result indicates that different morphology of TiO_2 nanotubes, nanoporous and non-organized structure leads to the difference not only in photon-to-current conversion efficiencies (IPCE) but also in photocatalytic activities. The photoreduction reaction of chromium (VI) yield on a TiO_2 nanotube is higher than that on TiO_2 nanoporous and non-organized form respectively.

In summary a novel, well-aligned titanium nanotube array on Ti substrate was successfully prepared using the electrochemical method. It was observed that the morphologies of the as-prepared titanium nanostructure were greatly influenced by the composition of electrolyte and medium modifiers. It is noted that only organic medium modifier in electrolyte can provide nanotube array. The photocatalytic activity of titanium nanostructure was strongly depending on the morphology. The different photocatalysis activity may be attributed to the difference of active surface area and turnover between the nanotubes and the nanoporous and non-organized films. TiO_2 nanotubes have larger specific surface area than TiO_2 film and could adsorb more substrate matters and provide more effective separation of the photogenerated electron-hole pairs. Consequently the greater the activity of photocatalyst is, the greater the quantum yield. The photocatalytic activities increase in the order of non-organized form < nanoporous < nanotube.

4.5.2 Photocatalysis properties of metal doped TiO_2 nanotube prepared by pulse anodization

Ideally, a semiconductor photocatalyst for the purification of water should be chemically and biologically inert, photocatalytically active, easy to produce and use, and activated by sunlight. It is hardly surprising that no semiconductor fits this demanding list of requirement perfectly, although the semiconductor titanium dioxide (TiO_2) come close but dose not absorb visible light. Indeed, TiO_2 has a large band gap energy, $E_{bg} \approx 3.2\text{-}3.0$ eV, and, as a consequence, is only able to absorb ultraviolet (UV) light (typically < 380 nm), which represents a small fraction, *ca.* 6% of the solar spectrum. However, the very positive features of TiO_2 as a semiconductor photocatalyst far outweigh the limitations of its spectral profile and thus, it has become the semiconducting material for research in the field of semiconductor photocatalysis for water purification. Attempts at extending the visible light response of TiO_2 by metal doping date back to ~1977. Historically, doping of the titania has been the approach taken for band-gap of material. When employing dopant to change the optical response of a material, it is desirable to maintain the integrity of the host material crystal structure while changing its electronic structure. Most of the studies were focused on the nanosized TiO_2 with the purpose of improving the light absorption.

In this work, the photoactivity is investigated by performing the photocatalysis reduction experiments of chromium hexavalent using TiO_2 and metal doped TiO_2 nanotubes using anodization technique. The comparison of photoreduction rates for TiO_2 with and without dopants is presented.

4.5.2.1 Effect of medium modifiers on properties of metal doped TiO_2

The photoresponse is usually evaluated by the incident photon-to-current conversion efficiency (IPCE) sometimes referred to also as "external quantum efficiently" corresponds to the external circuit divided by the monochromatic photon flux that strikes the cell. This key parameter can be expressed by the product (de Tacconi *et al.*, 2006)

$$IPCE(\lambda) = 1240\ (I_{sc}/\ \lambda\Phi) \qquad \text{(Eq. 4.7)}$$

Where λ is the light wavelength, I_{sc} is the current at short circuit (mA/cm^2), and Φ is the incident radiative flux (W/cm^2). The IPCEs and photoreduction efficiencies in Cr(VI) removal are shown in Fig. 4.30. The kinetic parameters in Cr(VI) photoreduction are shown in Fig. 4.31 and Table 4.11-4.12.

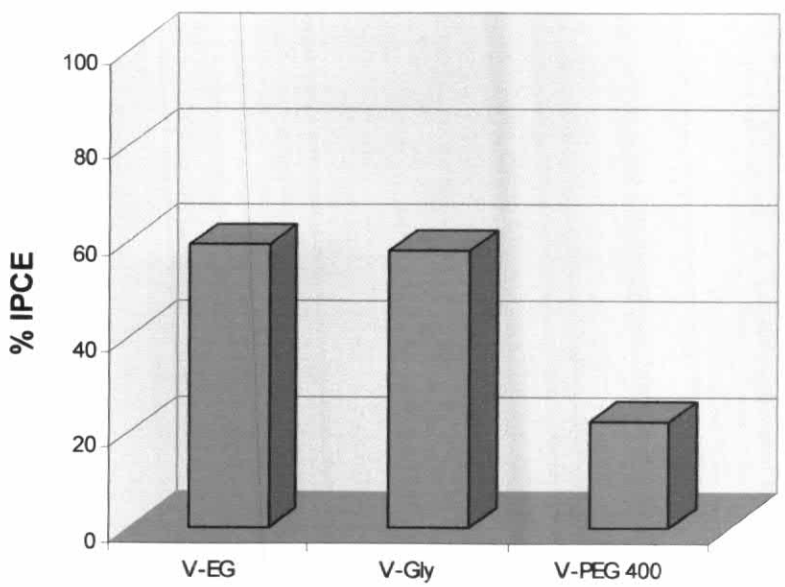

Figure 4.30. Bar graphs comparing % IPCE for films prepared by doping with VF_4 in different co-dopant.

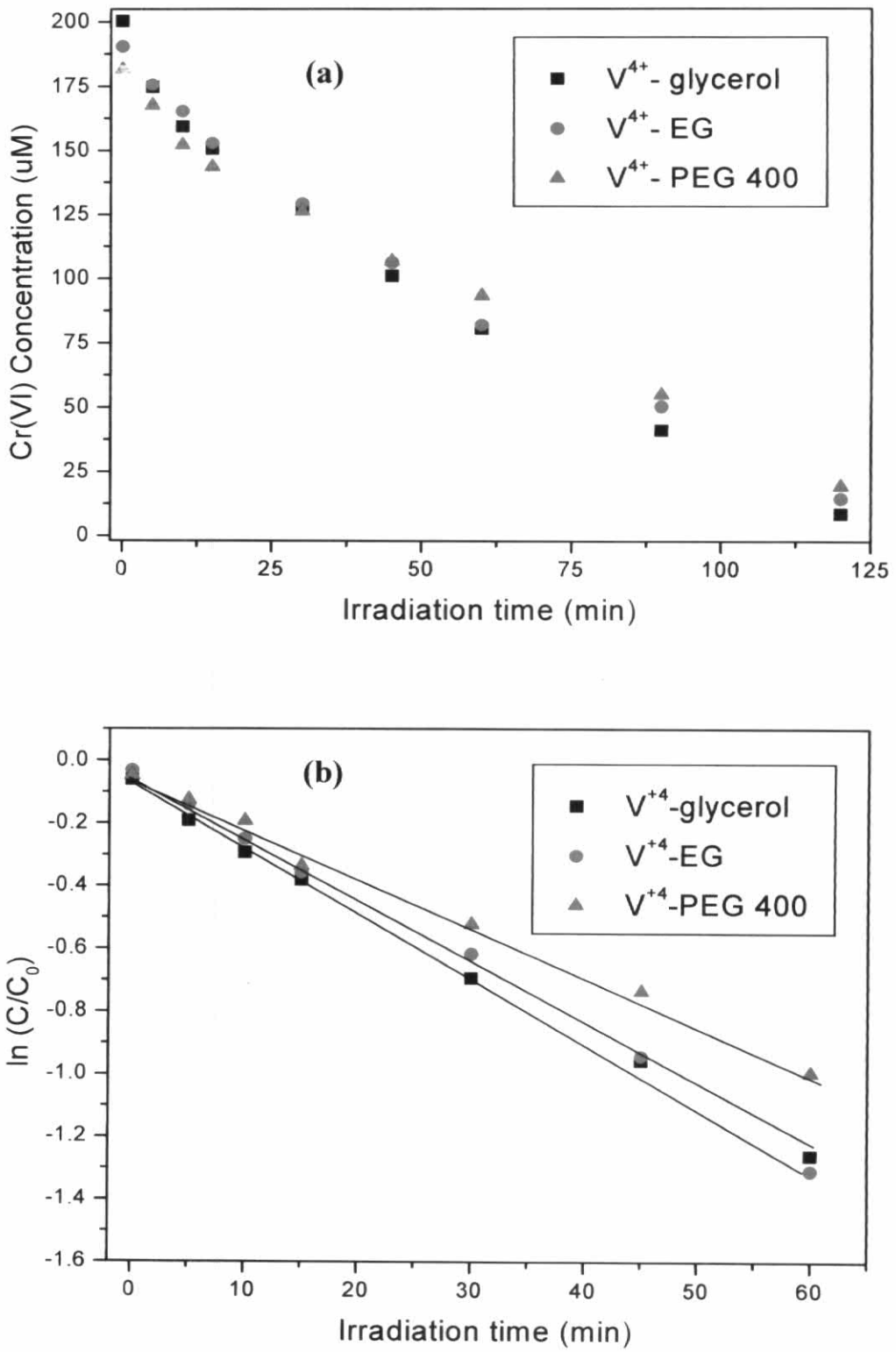

Figure 4.31 Kinetic plots of photocatalytic reduction of Cr(VI) in aqueous solution (200 μM) using various types of TiO_2 nanotube films prepared with different co-dopant using VF_4 as metal-dopant

Table 4.11 Kinetic parameters on photocatalytic reduction of Cr(VI) for metal doped TiO_2 nanotube films prepared with different co-dopant using VF_4 as metal-dopant

Metal Doped	k_{obs} (min^{-1})	$t_{1/2}$ (min)	$r_{initial}$ ($\mu M/min$)	Φ ($\times 10^{-3}$)
TiO_2- V^{4+}-glycerol	1.42×10^{-2}	48.60	2.86	1.47
TiO_2-V^{4+}-EG	1.35×10^{-2}	51.26	2.58	1.25
TiO_2- V^{4+}-PEG 400	1.07×10^{-2}	64.71	1.95	0.98

Table 4.12 Properties of metal-doped TiO_2 nanotube film prepared with different co-dopant using VF_4 as metal-dopant

Metal Doped	Inner diameter (nm)	EN	Band gap (eV)
TiO_2- V^{4+}-glycerol	65±1	1.63	3.10
TiO_2-V^{4+}-EG	69±1	1.63	3.10
TiO_2- V^{4+}-PEG 400	100±2	1.63	3.10

For the specific case of oxide nanotubes, additives such as PEG, glycerol, and ethylene glycol can be used to control the morphology and growth mechanism. Preferential adsorption and the high viscosity of these additives improve the quality of the resulting film by affecting the degree of oxide dissolution at high positive potentials.

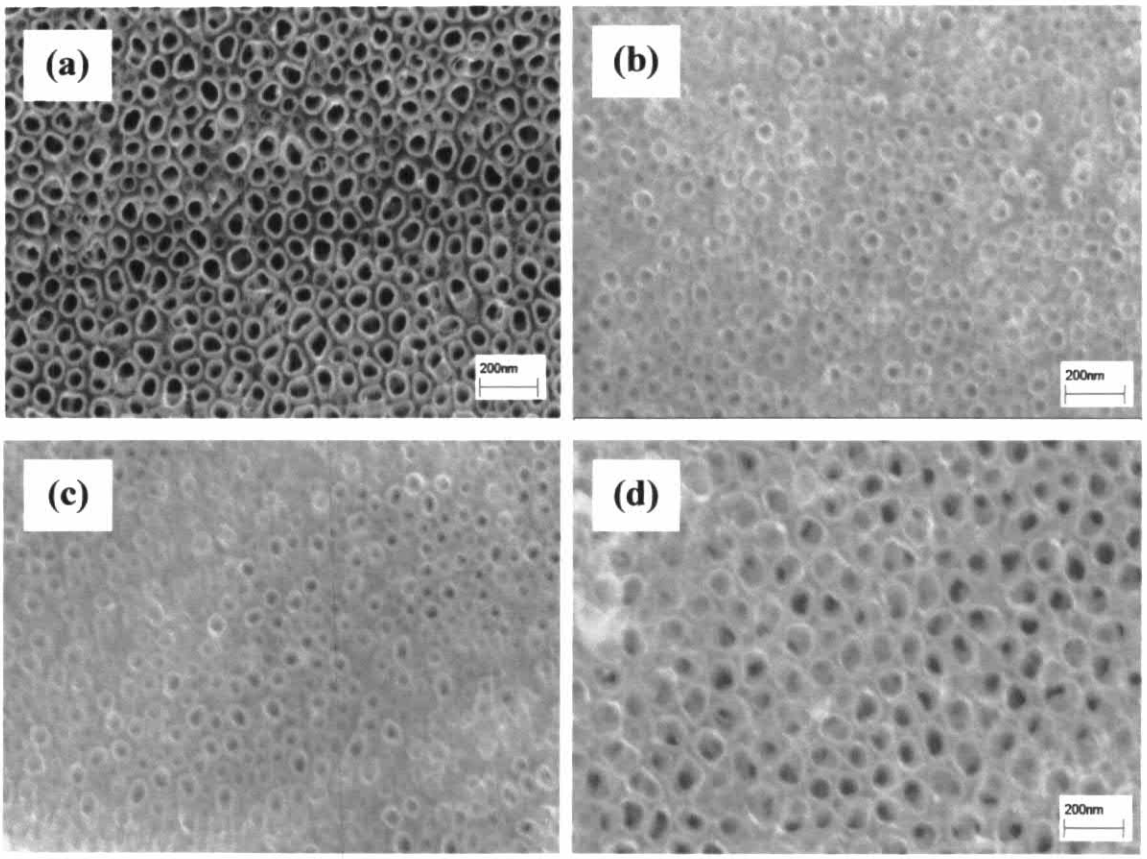

Figure 4.32 SEM images of TiO_2 nanotube arrays grown by pulse anodization (20 V, /-4 V) compared with corresponding (a) TiO_2 nanotube using glycerol as medium modifier without metal doping (b) V^{4+} metal doping film in 0.36 M NH_4F electrolyte using glycerol (c) ethylene glycol and (d) poly ethylene glycol 400 as co-dopant respectively.

Fig. 4.32 contains representative SEM data showing the influence of V^{4+} metal doped on the growth of TiO_2 nanoporous structure in 0.36 M NH_4F as electrolyte by pulse waveform between 20 V/-4 V. In all the cases, the TiO_2 nanotubes were grown for 3 h. Using EG as medium modifier, TiO_2 nanotube inner diameter around 82 nm, and wall thickness 15 nm (Fig. 4.32a) can be obtained. When VF_4 is added to the fluoride electrolyte as metal dopant (Fig. 4.32b), the resultant TiO_2 nanostructure was extremely change. The TiO_2 nanotube walls are clearly separated as individual tube and the TiO_2 nanotube diameter also shrinks from 82 ± 2 nm in to 69 ± 1 nm. Thus surface areas of the nanotube structure are increased for the reaction with Cr(VI).

It can be observed that highly ordered TiO_2 nanotube arrays were composed of nanotubes with average inner diameter of 65, 69, and 100 nm corresponding to glycerol, ethylene glycol and polyethylene glycol 400 as media modifier, respectively. Small nanotube diameters such as those generated from glycerol and ethylene glycol provide high quantum yield of Cr (VI) photoreduction reaction compared to other TiO_2 nanostructured as reported previously. Diameter of nanotubes are depend on the anodization waveform, and metal dopant. These dimensions provide the clear path for O_2 bubbles generated inside the tubes without blocking effect. Thus the medium modifiers clearly play a role in the nanotube wall thickness, diameter and length under different waveform potentials and durations and these variables, in turn, impact the photocatalytic activity. Recently, Macak and Schmuki (2006) reported formation of smooth and ridges-free nanotubes of much smaller diameter and very high aspect ratio using fluoride containing high viscous organic electrolytes such as glycerol and ethylene glycol. The diameter of the nanotubes varied from 40 nm to 60 nm and anodization for 18 h resulted in length of about 6 μm. An improved ordering and smooth surface of the nanotube array formed in high viscous organic solutions could provide more interesting applications to these nanotubes such as potical wave guides. Recently, Paulose *et al.* (2006) reported 134 μm long nanotular arrays by anodizing in various non-aqueous organicpolar electrolytes such as ethylene glycol, dimethyl sulfoxide, formamide etc. When the TiO_2 nanotubes formed in the organic solutions were annealed at 500-650 °C, the adsorbed carbon species during the anodization process modified the tubes as $TiO_{2-x}C_x$ after annealing by internal-diffusion if carbon into the lattice (Raja *et al.*, 2007). In terms of the comparative effect of the three medium modifiers (glycerol, ethylene glycol and PEG 400) or call "co-dopant" on the resulting photocatalysis performance of metal doped TiO_2 nanotube arrays. From the images reported in the work it is clear, that the self-organized structures produced in glycerol co-dopant are significantly different from all structures forms in aqueous electrolytes (Raja *et al.*, 2007). This process resulted in an improved photoactivity during photoelectrochemical generation of hydrogen, which was similar to the behavior of carbon modified TiO_2.

The smoothness of the nanotubes could play an important role for the improvement of various properties of these self-organized TiO_2 nanotubular structure. For example, the absence of ripple may affect the optical properties such as, for example, the light reflection behavior and thus may have a way to application such as photonic crystals or waveguides. It is note worthy that tube from under identical conditions in glycerol and ethylene glycol has a considerably different morphology in other word, specific chemical effects, such as the surface adsorption behavior, or possible formation of decomposition product, cannot be ruled out.

4.5.2.2 Kinetic study of chromium removal by photocatalysis reduction using metal doped TiO_2 with ethylene glycol as co-dopant

Photocatalytic reduction of Cr(VI) in aqueous solution using TiO_2 nanotube doped with various metals are shown Fig. 4.33a. As the reactions follow pseudo first-order pattern, the kinetic parameters can be obtained from the plot of $\ln(C/C_0)$ versus irradiation time as shown in Fig. 4.33b.

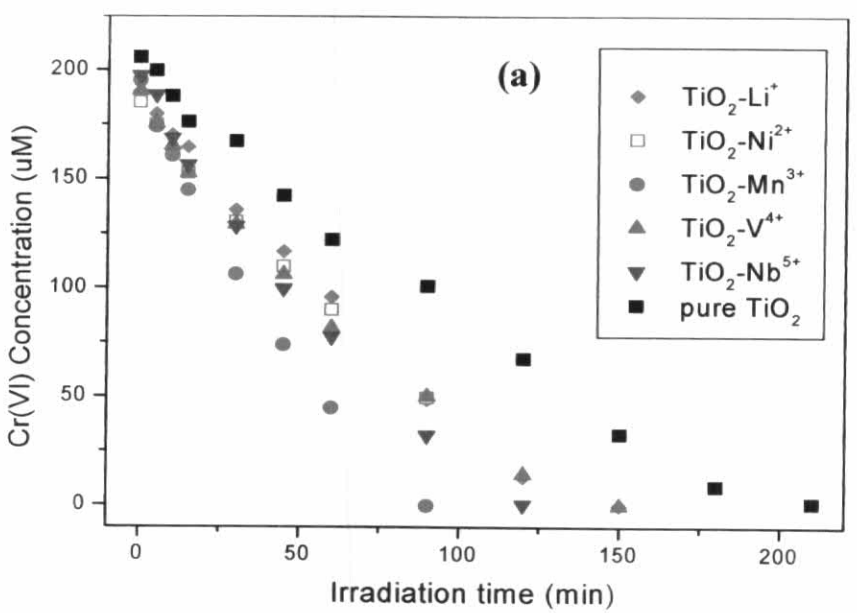

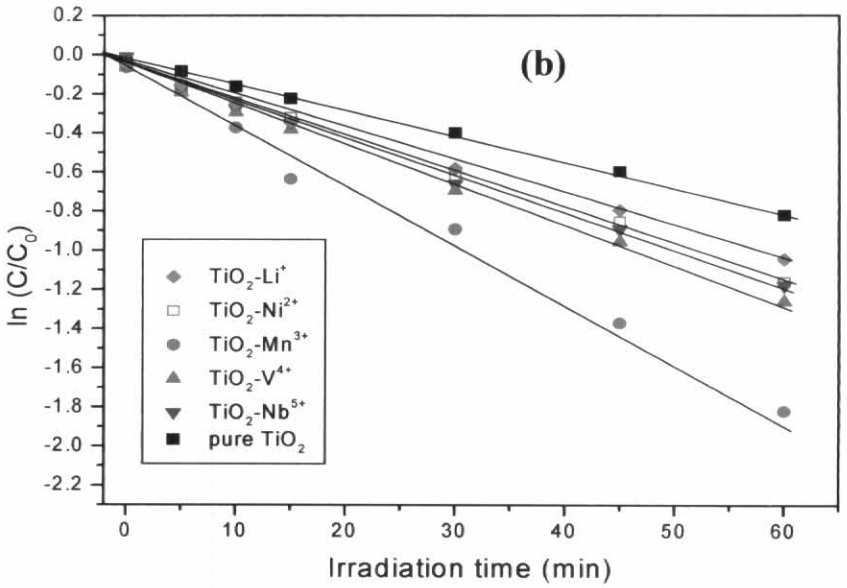

Figure 4.33 Kinetic plots of photocatalytic reduction of Cr(VI) in aqueous solution (200 μM) using various types of TiO_2 nanotube films prepared using ethylene glycol as co-dopant

The kinetic parameters of photocatalytic reduction of Cr(VI) can be calculated following the pseudo first-order photocatalytic reduction reaction which is expressed as;

$$\ln(C_0/C) = kt \qquad \text{(Eq. 4.8)}$$

Where k is the apparent rate constant, t is the irradiation time, and C_0, C are the initial and effluent concentrations of Cr (VI) in aqueous solution, respectively. The kinetic parameters included kinetic constant, k_{obs}, half-life, $t_{1/2}$, and apparent rate constants, $r_{initial}$, of the photocatalytic reduction of Cr (VI) were calculated as shown in Table 4.13.

Table 4.13 Kinetic parameters on photocatalytic reduction of Cr(VI) for metal doped TiO_2 nanotube films using ethylene glycol as co-dopant

Metal Doped	k_{obs} (min^{-1})	$t_{1/2}$ (min)	$r_{initial}$ ($\mu M/min$)
Pure TiO_2	1.07×10^{-2}	64.95	1.98
TiO_2-Li+-EG	1.13×10^{-2}	61.49	2.15
TiO_2-Ni^{2+}-EG	1.17×10^{-2}	59.03	2.18
TiO_2-Mn^{3+}-EG	2.37×10^{-2}	29.27	4.63
TiO_2-V^{4+}-EG	1.35×10^{-2}	51.26	2.58
TiO_2-Nb^{5+}-EG	1.55×10^{-2}	44.62	3.07

From this experiment set, it is obvious that the Mn-doped TiO_2 nanotube provide highest initial rate in photocatalytic reduction of Cr(VI) as 4.63 μM/min with the shortest half-life, 29.27 min. With the highest value of initial rate of the reaction, the quantum yield of this film is consequently greatest number as shown in Fig. 4.34. The quantum yields of other films are sequence as follow;

Mn-doped TiO_2 > Nb-doped TiO_2 > V- doped TiO_2 > Ni- doped TiO_2 ≈ Li- doped TiO_2 > pure TiO_2

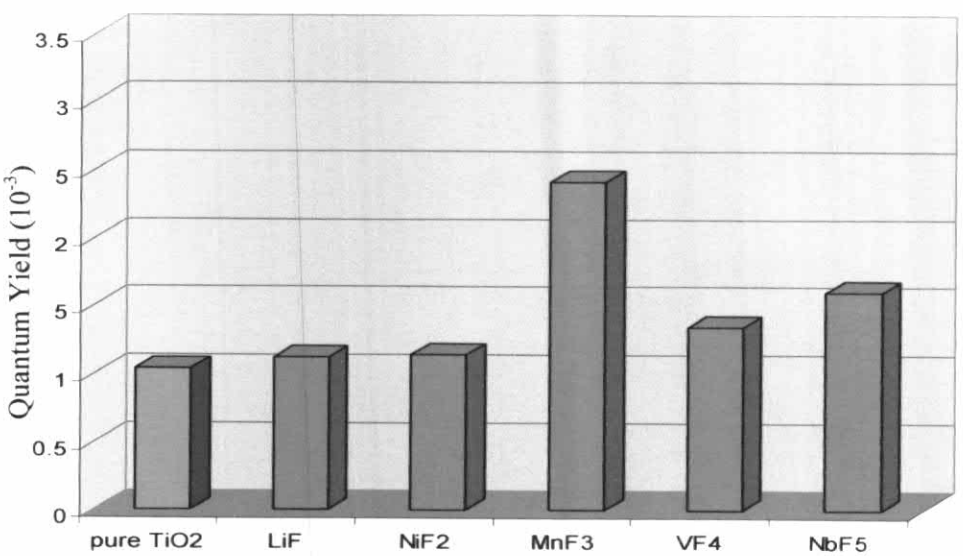

Figure 4.34 Quantum yield of each metal-doped TiO_2 nanotube film prepared by using ethylene glycol as co-dopant

To explain the photocatalytic reduction behavior of metal-doped TiO_2 nanotube, characteristics of each film have to be taken in account. The associated film properties include diameter of nanotube, electronegativity of doped metal, and the band gap of each metal-doped TiO_2. These properties are shown in Table 4.14

Table 4.14 Properties of metal-doped TiO_2 nanotube film prepared by using ethylene glycol as co-dopant

Metal Doped	Inner diameter (nm)	EN	Band gap (eV)
TiO_2-Li+-EG	71±2	0.98	2.90
TiO_2-Ni^{2+}-EG	61±1	1.90	3.10
TiO_2-Mn^{3+}-EG	66±2	1.55	2.85
TiO_2-V^{4+}-EG	69±1	1.63	3.10
TiO_2-Nb^{5+}-EG	76±2	1.60	2.90

Influence of each film characteristic on photocatalytic reduction of Cr(VI) can be described below.

It is well known that the film with small band gap requires less photon energy to promote the excitation of electron from valence band to the conduction band. Consequently, this small gap let the effectively use of semiconductor in visible light region. The smaller band gap, the higher amount of electron-hole pair can be produced.

The second property for photocatalysis efficiency consideration is electronegativity of the doped metal. Generally, the electronegativity of each atom is the ability of that atom to attract electrons to itself. The doped metal with high electronegativity value tends to draw and accumulate electrons on the nanotube surface for photocatalysis reaction. High electronegativity value leads to high amount of trapped electron and/or hole on the catalyst surface. Acting as electron and/or hole traps is the most important function of dopants. The trap of charge carriers can decrease the recombination rate of electron/hole pairs and consequently increase the lifetime of charge carriers. The process of charge trapping is as follows:

$$Ti^{4+} + e_{cb}^{-} \longrightarrow Ti^{3+} \quad \text{(Eq. 4.9)}$$

$$M^{n+} + e_{cb}^{-} \longrightarrow M^{(n-1)+} \quad \text{(Eq. 4.10)}$$

$$M^{n+} + h_{vb}^{+} \longrightarrow M^{(n+1)+} \quad \text{(Eq. 4.11)}$$

$$OH^{-} + h_{vb}^{+} \longrightarrow OH^{\bullet} \quad \text{(Eq. 4.12)}$$

$$e^{-}_{cb} + h^{+}_{vb} \longrightarrow \text{recombination} \quad \text{(Eq. 4.13)}$$

where M^{n+} is the metal ion dopant. The energy level of M^{n+} / $M^{(n-1)+}$ lies below the conduction band edge and the energy level of M^{n+} / $M^{(n+1)+}$ lies above the valence band edge. Metal cation can replace Ti^{4+} leaving extra electrons weakly bound to the dopant center and thus contributing to the conduction band. Electrons in the conduction band are trapped by doped metal without recombining, providing a valence band (VB) with more holes (see Fig. 4.35). Decreased recombination also produces more interfacial charge transfer potential to create more super oxide radicals.

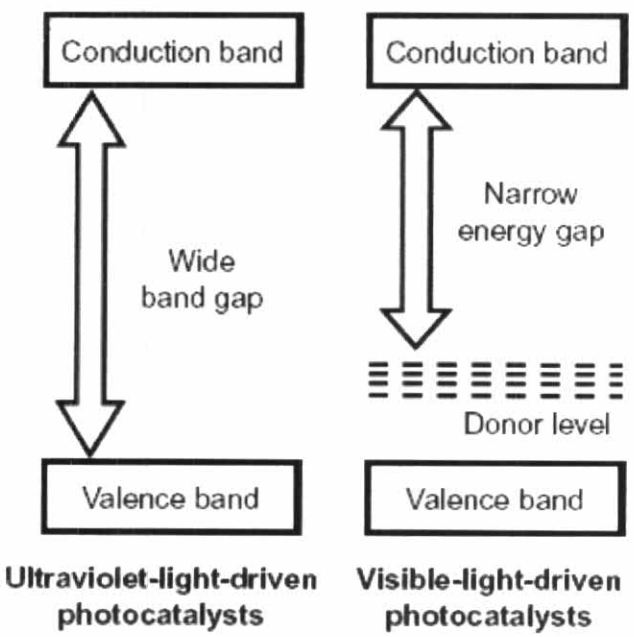

Figure 4.35 Design of visible-light-driven photocatalyst applying a doping strategy.

Thus, the energy level of transition metal ions affects the trapping efficiency. The trapping of electrons makes it easy for electron transfer onto the surface of TiO_2 and react with Cr(VI) in solution and reduced to Cr(III) in this work.

Besides the band gap of catalyst and electronegativity of doped metal, the diameter of TiO_2 nanotube also plays important role in determination of photocatalytic efficiency. The smaller diameter of the tube, the higher in surface area as the reaction site in photocatalysis reaction.

From overall catalyst characteristic consideration, obviously, the Mn-doped TiO_2 tends to provide highest efficiency in photocatalytic reduction of Cr(VI) owing to smallest band gap (2.85), high electronegativity (1.55) and small diameter of nanotube (66±2 nm). The plenty reactive surface site for photocatalytic reaction of Cr(VI) of Mn-doped TiO_2 could be anticipated. Nb-doped TiO_2 can also provide high efficiency of photocatalytic reduction of Cr(VI) as well. It is noted that both Mn-doped TiO_2 and Nb-doped TiO_2 has the high electronegativity values as 1.55 and 1.63, respectively. As the result, these two types of nanotube can generate high amounts of electron-hole pair and these carriers can be trapped on the surface site for photocatalytic reactions. Consequently, with the superb characteristics, the Mn-doped TiO_2 nanotube becomes the most effective film for photocatalytic reduction of Cr(VI).

With the highest electronegativity as 1.90, the Ni-doped TiO_2 catalyst tends to draw electron to the tube surface better than other metal-doped TiO_2. However, with the wide band gap (3.1 eV) of this semiconductor, the generated electrons are not as large as other metal doped TiO_2 catalysts. In addition, the diameter size of Ni-doped TiO_2 does not much different from other metal-doped TiO_2, thus the reactive site for this catalyst is not pronouncedly differ from other nanotube leading to less photocatalytic efficiency comparing to Mn-doped TiO_2 and other metal-doped catalyst.

4.5.2.3 Kinetic study of chromium removal by photocatalysis reduction using metal doped TiO_2 with polyethylene glycol as co-dopant

Photocatalytic reduction of Cr(VI) in aqueous solution using TiO_2 nanotube doped with various metals and synthesized using polyethylene glycol as co-dopant are shown Fig. 4.36a. As the reactions follow pseudo first-order pattern, the kinetic parameters can be obtained from the plot of $\ln(C/C_0)$ versus irradiation time as shown in Fig. 4.36b.

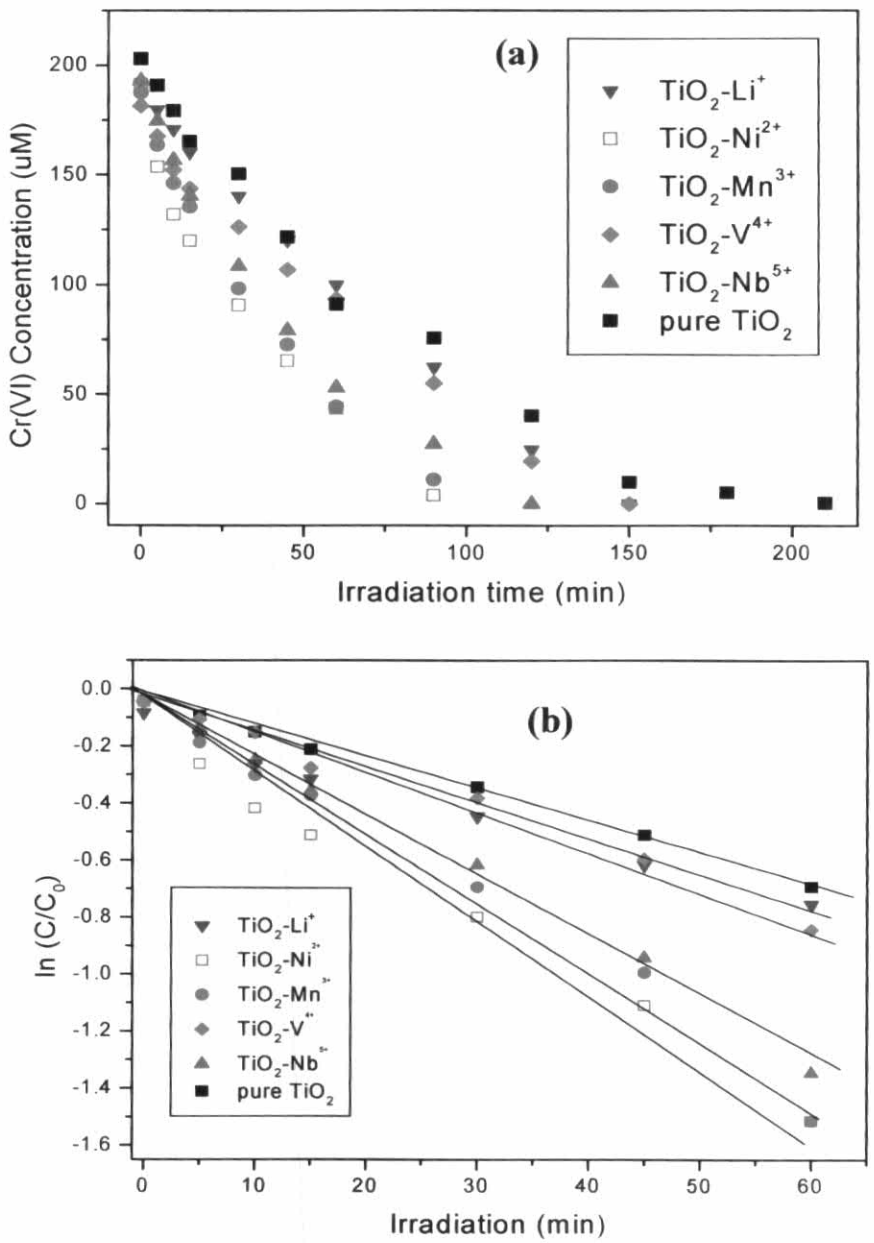

Figure 4.36 Kinetic plots of photocatalytic reduction of Cr(VI) in aqueous solution (200 μM) using various types of TiO_2 nanotube films prepared using polyethylene glycol as co-dopant

The kinetic parameters of photocatalytic reduction of Cr(VI) can be calculated following the pseudo first-order photocatalytic reduction reaction which is expressed as;

$$\ln(C_0/C) = kt \qquad \text{(Eq. 4.14)}$$

Where k is the apparent rate constant, t is the irradiation time, and C_0, C are the initial and effluent concentrations of Cr (VI) in aqueous solution, respectively. The kinetic parameters included kinetic constant, k_{obs}, half-life, $t_{1/2}$, and apparent rate constants, $r_{initial}$, of the photocatalytic reduction of Cr (VI) were calculated as shown in table 4.15.

Table 4.15 Kinetic parameters on photocatalytic reduction of Cr(VI) for metal doped TiO_2 nanotube films using polyethylene glycol as co-dopant

Metal Doped	k_{obs} (min^{-1})	$t_{1/2}$ (min)	$r_{initial}$ (μM/min)
Pure TiO_2	1.63×10^{-2}	42.41	3.00
TiO_2-Li+-PEG 400	1.06×10^{-2}	65.56	2.02
TiO_2-Ni^{2+}- PEG 400	1.17×10^{-2}	30.18	4.40
TiO_2-Mn^{3+}- PEG 400	2.29×10^{-2}	30.31	4.29
TiO_2-V^{4+}- PEG 400	1.07×10^{-2}	64.71	1.95
TiO_2-Nb^{5+}- PEG 400	2.09×10^{-2}	33.13	4.04

From this experiment set, it is obvious that the Ni-doped TiO_2 nanotube and Mn-doped TiO_2 nanotube provide high initial rates in photocatalytic reduction of Cr(VI) as 4.40 and 4.29 μM/min, respectively, with the short half-life, 30.18 and 30.31 min, respectively. It is noted that the Ni-doped TiO_2 nanotube exerted photocatalytic activity in equivalent with Mn-doped TiO_2 nanotube. All kinetic parameters from these two films do not considerably different. The quantum yields of all films are also determined as shown in Fig. 4.37 with can be sequenced as follow; Ni-doped TiO_2 ≈ Mn-doped TiO_2 > Nb- doped TiO_2 > pure TiO_2 > V- doped TiO_2 ≈ Li- doped TiO_2

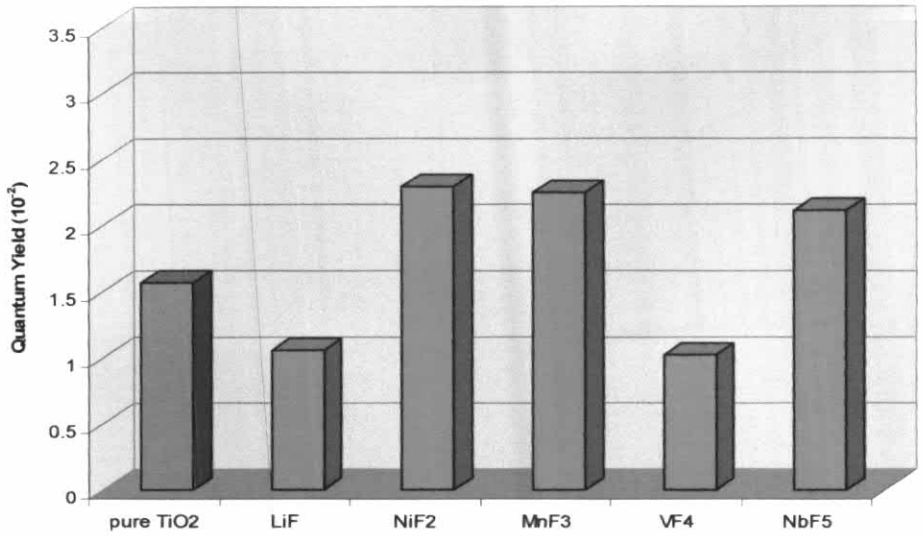

Figure 4.37 Quantum yield of each metal-doped TiO_2 nanotube film prepared by using polyethylene glycol as co-dopant

To explain the photocatalytic reduction behavior of metal-doped TiO_2 nanotube, characteristics of each film have to be taken in account. The associated film properties include diameter of nanotube, electronegativity of doped metal, and the band gap of each metal-doped TiO_2. These properties are shown in Table 4.16

Table 4.16 Properties of metal-doped TiO_2 nanotube film prepared by using polyethylene glycol as co-dopant

Metal Doped	Inner diameter (nm)	EN	Band gap (eV)
TiO_2-Li+-PEG 400	98±2	0.98	2.85
TiO_2-Ni^{2+}- PEG 400	79±2	1.90	3.10
TiO_2-Mn^{3+}- PEG 400	75±2	1.55	2.85
TiO_2-V^{4+}- PEG 400	100±2	1.63	3.10
TiO_2-Nb^{5+}- PEG 400	116±1	1.60	2.90

In consideration of band gap, Mn-doped TiO_2 and Li- doped TiO_2 provided the smallest band gap (2.85 eV). It is anticipated that these two films can utilize photon energy in producing highest amount of electron-hole pair leading to possibly high efficiency in photocatalytic reduction of Cr(VI). However, with relatively low electronegativity of Li, the Li- doped TiO_2 does not effectively attract electron on the catalyst surface comparing with other metal-doped TiO_2 nanotubes. Besides smallest band gap, the high electronegativity (1.55) and smallest diameter of nanotube (75±2 nm) of Mn-doped TiO_2 enhance high photocatalytic efficiency in Cr(VI) removal as represented by quantum yield of this catalyst.

For Ni-doped TiO_2, it is surprisingly that this film can provide highest quantum yield efficiency in Cr(VI) reduction as well as Mn-doped TiO_2. This phenomenon can be explained by the electronegativity of Ni and the size of nanotube. From Table 4.16, the electronegativity of Ni is 1.90 which is highest among the investigated metals. Even tough the Ni- doped TiO_2 can produce lowest amount of electron-hole pairs, but the generated carriers can be effectively attached on it surface. It is reported previously (Woo *et al.*, 2007) that Ni acts like sink of electron in reducing recombination of electron-hole pair. Thus, the photocatalytic reduction of Cr(VI) can be fully occurred with these trapped surface electrons. In combination with high electronegativity, the Ni-doped TiO_2 nanotube has relatively small diameter (79±2 nm) comparing to other metal-doped catalyst. The higher reactive surface sites and higher amount of trapped surface electrons lead to high photocatalytic efficiency in Cr(VI) removal.

For Nb- doped TiO_2, the bigger size of nanotube diameter (116±1 nm) leads to smaller photocatalytic efficiency in reduction of Cr(VI) than Ni-doped TiO_2. Either low electronegativity or bigger diameter of nanotube is the major property leading to incomparable photocatalytic efficiency of other metal-doped TiO_2 catalysts.